


ulm university universität
**uulm**

Institut für Theoretische Physik
Controlled Quantum Dynamics Group

# Numerical Methods for Complex Quantum Dynamics with Applications to Quantum Biology and Quantum Many-Body Dynamics

**Dissertation zur Erlangung des Doktorgrades**

**(Dr. rer. nat.)**

an der Fakultät für Naturwissenschaften der Universität Ulm
vorgelegt von

**Robert Rosenbach**

aus Kassel

Ulm, Mai 2015

## Dissertation

| | |
|---|---|
| **title** | *Numerical Methods for Complex Quantum Dynamics with Applications to Quantum Biology and Quantum Many-Body Dynamics* |
| **by** | Robert Rosenbach |
| **at the** | Institute for Theoretical Physics<br>University of Ulm<br>Albert-Einstein-Allee 11<br>89069 Ulm<br>Germany |
| **supervised by** | Prof. Dr. Martin B. Plenio |

---

| | |
|---|---|
| **Dekan der Fakultät** | Prof. Dr. Joachim Ankerhold |
| **Erstgutachter** | Prof. Dr. Martin B. Plenio |
| **Zweitgutachter** | Prof. Dr. Joachim Ankerhold |
| **Tag der Prüfung** | 16. Juli 2015 |

# Abstract

Multi-component quantum systems that interact strongly with their environments are difficult to simulate numerically. The coupling cannot be treated perturbatively and the standard approaches are often invalid or inefficient. In the present work we approach this challenge by introducing the numerically exact Time Evolving Density Matrix with Orthogonal Polynomial Algorithm (TEDOPA). The application of this algorithm allows for the efficient simulation of open quantum system dynamics, including spin-boson models and generalizations of it to multi-component systems. It is a two-stage method that transforms a spin-boson type environment into a one-dimensional configuration, subsequently treating this configuration numerically.

We first introduce the analytical and numerical tools that are necessary, resulting in the introduction of the TEDOPA algorithm. We highlight key points and implementational issues for the two distinct steps that TEDOPA comprises, followed by a general assessment of properties and applicability of the algorithm. Further we provide background information on the field of open quantum systems to evaluate the scope of, and possible applications for, TEDOPA as compared to similar techniques. Further we provide an introduction to the field of quantum biology, which provides a large body of open questions and challenges for tools like TEDOPA.

In the following main part of this work we start out by applying TEDOPA to biological settings, justifying why a full-grown TEDOPA simulation is necessary and what valuable insight we thereby extract. The systems of interest are pigment-protein complexes that play a key role in the photosynthetic process and that have been studied extensively in the last years. Experimental results indicate the occurrence of quantum effects – an unexpected and uncommon observation for which we present a microscopic mechanism that elicits similar results, offering an explanation of these effects.

This part is followed by subsequent improvements of TEDOPA, resulting in major speed-ups for certain parameter regimes. These improvements result from apt combinations with recent tools from open quantum systems and linear algebra. We highlight their applicability and identify novel regimes accessible by these extensions. We conclude this work by a succinct summary combined with an outlook to future applications.

# List of Publications

This thesis is partly based on, or has been taken from, material that has first been published elsewhere. This relates especially to Chapters 5 to 8, which are in large parts identical to [R1] - [R4]. At the beginning of the according chapters this relation is indicated as well. The corresponding references are

[R1] **A. W. Chin, J. Prior, R. Rosenbach, F. Caycedo-Soler, S. F. Huelga, and M. B. Plenio**
*The role of non-equilibrium vibrational structures in electronic coherence and recoherence in pigment–protein complexes*
Nature Physics 9, 113–118 (2013)
Copyright (2013) by Nature Publishing Group
arXiv: 1203.0776
Chapter 5, Reference [1]

[R2] **S. Oviedo-Casado, J. Prior, A. W. Chin, R. Rosenbach, S. F. Huelga, and M. B. Plenio**
*Phase-dependent exciton transport and energy harvesting from thermal environments*
Phys. Rev. A 93, 020102 (2016)
Copyright (2016) by the American Physical Society
arXiv: 1506.08151
Chapter 6, Reference [2]

[R3] **R. Rosenbach, J. Cerrillo, S. F. Huelga, J. Cao, and M. B. Plenio**
*Efficient simulation of non-Markovian system-environment interaction*
New J. Phys. 18, 023035 (2016)
doi:10.1088/1367-2630/18/2/023035
Copyright (2016) by IOP Publishing and Deutsche Physikalische Gesellschaft
(Published under a Creative Commons Attribution Licence: CC BY 3.0)
arXiv: 1510.03100
Chapter 7, Reference [3]

[R4] **D. Tamascelli, R. Rosenbach, and M. B. Plenio**
*Improved scaling of time-evolving block-decimation algorithm through reduced-rank randomized singular value decomposition*
Phys. Rev. E 91, 063306 (2015)
Copyright (2015) by the American Physical Society
arXiv: 1504.00992
Chapter 8, Reference [4]

# Contents

**Abstract** i

**List of Publications** iii

**1 Introduction** 1

**2 Open Quantum Systems** 5
- 2.1 General properties . . . 6
- 2.2 Markovian evolution . . . 7
  - 2.2.1 Born-Markov master equation . . . 8
  - 2.2.2 Lindblad equation . . . 9
- 2.3 The Redfield equation . . . 11
- 2.4 Non-Markovian evolution . . . 13
  - 2.4.1 Nakajima-Zwanzig equation . . . 13
  - 2.4.2 Extended approaches . . . 14
- 2.5 The spin-boson model . . . 15
- 2.6 Further methods . . . 16

**3 Numerical preliminaries** 19
- 3.1 Singular value decomposition . . . 19
- 3.2 Orthogonal polynomials . . . 21
- 3.3 Time evolving block decimation . . . 22
  - 3.3.1 Matrix product states . . . 23
  - 3.3.2 Gate applications . . . 25
  - 3.3.3 Implementation and scaling considerations . . . 27
  - 3.3.4 Measurements . . . 28
  - 3.3.5 Matrix product operators . . . 30
    - 3.3.5.1 Thermal states . . . 31
  - 3.3.6 Time evolution . . . 32
  - 3.3.7 Error analysis . . . 33
- 3.4 TEDOPA . . . 35
  - 3.4.1 The chain mapping . . . 35
  - 3.4.2 Numerical treatment . . . 38

**4 Quantum Biology** **41**
4.1 Bird navigation . . . 42
4.2 Sense of smell . . . 42
4.3 Photosynthetic complexes . . . 43
4.3.1 Photosynthesis . . . 44
4.3.2 Evidence of quantum effects in transport processes . . . 46
4.3.3 Experimental methods . . . 47
4.3.4 Theoretical methods . . . 51
4.3.5 Numerical methods . . . 55

**5 Electronic coherence and recoherence in PPCs** **57**
5.1 Motivation . . . 57
5.2 The microscopic model . . . 58
5.3 The physical mechanism of vibration-induced electronic coherence . . . 60
5.4 Semiclassical equations of motion . . . 61
5.4.1 Non-Markovian pure dephasing rates . . . 63
5.5 Fundamental mechanisms supporting long lived coherence . . . 65
5.6 Numerically-exact simulations . . . 66
5.6.1 Inter-exciton and ground-exciton coherences . . . 68
5.6.2 Population oscillations and environmental variables . . . 70
5.7 Single system vs. ensemble . . . 72
5.8 Anomalous anisotropy decay in organic polymers . . . 73

**6 Phase-dependent exciton transport** **75**
6.1 Motivation . . . 75
6.2 Dimer description . . . 77
6.3 Theoretical analysis . . . 78
6.4 Master equations . . . 82
6.4.1 Derivation . . . 82
6.4.2 Discrete modes . . . 84
6.5 Conclusions . . . 88

**7 The Transfer Tensor Method and TEDOPA** **89**
7.1 Motivation . . . 89
7.2 Non-Markovian dynamical maps . . . 90
7.3 Synergies . . . 92
7.4 Parameters and accuracy . . . 92
7.5 Benchmark . . . 93
7.6 Applications . . . 95
7.6.1 Non-Ohmic spectra . . . 95
7.6.2 Low temperatures . . . 96
7.6.3 Absorption spectrum . . . 97
7.7 Simulation time . . . 98
7.8 Conclusions . . . 100

**8 Reduced-Rank Randomized Singular Value Decomposition** **103**
8.1 Motivation . . . 103
8.2 An advanced application of the TEBD algorithm . . . 104

8.3 Reduced-rank randomized SVD . . . 105
8.4 RRSVD case-study and profiling of real TEBD simulations . . . 113
8.4.1 Stability analysis . . . 113
8.4.2 Performance on larger matrices and TEBD profiling . . . 114
8.5 Conclusions and Outlook . . . 118

**9 Summary and outlook** **121**

**Acknowledgements** **125**

**Curriculum Vitae** **127**

**Erklärung wissenschaftlicher Redlichkeit** **129**

**References** **130**

# CHAPTER 1

# Introduction

Multi-component quantum systems that interact strongly with their environments are difficult to simulate numerically. The coupling cannot be treated perturbatively and the standard approaches are often invalid or inefficient. In the present work we approach this challenge by introducing the numerically exact Time Evolving Density Matrix with Orthogonal Polynomial Algorithm (TEDOPA), first presented in [5, 6]. The application of this algorithm allows for the efficient simulation of open quantum system dynamics, including spin-boson models and generalizations of it to multi-component systems. It is a two-stage method that transforms a spin-boson type environment into a one-dimensional configuration, subsequently treating this configuration numerically.

We start out in Chapter 2 by providing background information of some related techniques for open quantum systems. Those are mainly standard approaches that are useful to illustrate for which regimes perturbative or analytical approaches are insufficient, thus indicating when it is desirable to resort to, or newly develop, numerically exact methods.

To fully grasp the analytical and numerical concepts that constitute TEDOPA, in Chapter 3 we introduce its basic underlying tools. This involves quite simple concepts like singular value decomposition and orthogonal polynomials, but quickly extends towards the numerical treatment of quantum many-body systems.

We then proceed in Chapter 4 towards the first field of application for TEDOPA – which is quantum biology. Protein complexes that play a major role during the photosynthetic process were in the last years discovered to feature signs of quantum effects. For the subsequent investigation of these complexes we introduce the biological settings, elaborating on the experimental and theoretical methods for their study.

This constitutes the preliminaries that allow to assess the scope of the present work. The following Chapters 5 to 8 introduce the research performed and published (or to be published) in [R1] - [R4] (see list of publications). The first two of these chapters focus on applications in biological settings, specifically in pigment-protein complexes that play

a major role in the photosynthetic processes, white the latter two introduce numerical improvements and combination that enhance TEDOPA's capabilities.

Chapter 5 revolves around results obtained from a special pigment-protein complex by ultrafast nonlinear spectroscopy that yielded sustained beating between optically excited states that last several hundreds of fs at room temperature, and up to nearly 2 ps at cryogenic temperatures [7, 8, 9, 10, 11]. These results have been interpreted as evidence for electronic coherences between excitons, with lifetimes surprisingly over an order of magnitude larger than coherences between electronic ground and excited states. These times are long enough for excitation energy transfer and excitonic coherence to coexist, constituting a setting that allows for sophisticated interplay of quantum and dissipative processes that theoretically optimize transport efficiency. We investigate this phenomenon by means of TEDOPA and provide a firm microscopic basis to successfully reproduce the experimentally observed coherence times in this complex. This is only possible due to TEDOPA's particular capability of treating non-trivial spectral structures of the protein environment. This mechanism details how environmental fluctuations can generate non-equilibrium processes that lead to the spontaneous creation and sustenance of electronic coherence, even at physiological temperatures.

We then continue in Chapter 6 to study pigment-protein complexes, specifically ultrafast, non-Markovian dynamics and their impact on non-equilibrium quantum thermodynamics. By means of TEDOPA, applied to a microscopic model for such complexes, we present and analyze an ultrafast environmental process that causes energy relaxation in the reduced system to depend explicitly on the phase of an initial preparation of eigenstates. Remarkably, for particular phases and system parameters, the net energy flow is uphill, transiently violating the principle of detailed balance, and implying that energy is spontaneously taken up from the environment.

Like any numerically exact method for open quantum systems, TEDOPA simulations are expensive. It is therefore worthwhile to make an effort to come up with improvements that allow to save on the associated computational demands. Thus we devote the next two chapters to the exploration of extensions and additional open quantum system approaches to exploit synergies, starting with the introduction of the transfer-tensor method (TTM) [12] in Chapter 7. For TEDOPA, as for any exact simulation method, it is generally the case that the size of the propagator or of the stochastic sample scales unfavorably with the time length of the simulation or the corresponding perturbative expansion order. For certain regimes though this scaling can be mitigated in some form if an effective propagator of a reduced size can be extracted with the intention of facilitating long-time simulations. TTM is a tool that quantifies the environment's back-action on the system as in the Nakajima-Zwanzig formalism, achieved by black-box learning from sample trajectories for some short initial period and subsequent generation of a compact multiplicative propagator for the system degrees of freedom alone. After introducing TTM, we specify the regime in which its combination with TEDOPA is expected to be most productive and continue by providing a benchmark between this proposed combination and the exact result and confirm perfect agreement while highlighting viability and combination synergies. Subsequently, relevant applications of this combination are proposed which include Ohmic and non-Ohmic spectral densities, low

temperature simulations and absorption spectra computations.

In Chapter 8 we again aim at improving the scaling of TEDOPA in order to save on computational demands – this time by focusing on the numerical part. We optimize its most costly part, the two-site update step employed in the numerical treatment, by resorting to a probabilistic, randomized algorithm to perform the singular value decomposition. After presenting the algorithm and reporting on its stability and accuracy, we combine it with a highly efficient low-level implementation that helps to considerably reduce the necessary numerical resources and improve the scaling of TEBD. We demonstrate that the critical step in the numerical evolution scheme can be addressed by the successful application of the randomized singular value decomposition, resulting in an improvement by more than one order of magnitude as compared to standard approaches – without additional accuracy losses. Finally we highlight for which parameter regimes this improvement results in the largest savings on computational time.

This thesis is concluded by Chapter 9 which recapitulates and summarizes again the key results and findings, putting them into perspective by addressing open questions and further research opportunities.

# CHAPTER 2

## Open Quantum Systems

The standard, well-known quantum evolution happens according to the Schrödinger equation

$$-i\hbar\frac{d}{dt}|\psi\rangle = H|\psi\rangle \tag{2.1}$$

for pure states or the von Neumann equation

$$\frac{d}{dt}\rho = -\frac{i}{\hbar}\left[H, \rho\right] \tag{2.2}$$

for mixed states. However these equations describe the unitary evolution of *closed* quantum systems and, since the Hamiltonian conserves energy, do not account for effects like decoherence or dissipation. This chapter introduces some basic concepts and methods used to treat so-called *open* quantum systems. These are systems which can interact with some kind of *environment* such that system and environment are treated by one joint Hamiltonian. The total evolution then is still unitary, however when regarding only the system of interest, this easily can result in a non-unitary evolution and thus introduce effects that cannot be observed in the closed-system counterpart. Since the main body of the present work centers on the development and applications of an efficient computational method for the simulation of open quantum system dynamics, first we set the stage by introducing basic concepts as well as some well-known and widely-used tools and methods. A much more detailed account of the presented concepts can be found in [13, 14, 15, 16].

Upon introducing an environment additionally to the system, the total Hamiltonian becomes

$$H = H_{\text{sys}} + H_{\text{env}} + H_{\text{int}} \tag{2.3}$$

with an additional term $H_{\text{env}}$ describing the evolution of the environment and $H_{\text{int}}$ which accounts for the interaction between system and environment. The term $H_{\text{sys}}$ corresponds to the full Hamiltonian $H$ from Eqs. (2.1) and (2.2).

When substituting this larger Hamiltonian in the evolution equations and extending the state $\rho$ to a combination of system and environment parts $\rho = \rho_{\text{sys}} \otimes \rho_{\text{env}}$ (plus possible correlations present between these two, depending on the initial state chosen), we still have a unitary evolution for the whole system plus environment configuration. Depending on the applied method, from this complete description some reduced description for only the system-part is derived - which then easily can exhibit non-unitary properties. A very general approach, independent of the actual parameters of the bath, comes from the quantum information area where such an open system evolution is described by a *dynamical map*

$$\rho(\tau) = \mathcal{E}_{0\to\tau}(\rho(0)) \tag{2.4}$$

where the dynamical map $\mathcal{E}_{0\to t}(\rho)$ is a quantum operation which propagates the state $\rho$ from time $t = 0$ to time $t = \tau$. Employing our knowledge of the unitary evolution of the complete system plus environment configuration, the dynamical map can be written as

$$\mathcal{E} = \text{tr}_{\text{env}}\left(U(\rho_{\text{sys}} \otimes \rho_{\text{env}})U^\dagger\right). \tag{2.5}$$

This propagates the joint system-environment state by the unitary transformation $U$ and subsequently traces out the environment to yield a system-only description. For arising questions like the requirement of an initial product state or the dimensionality of $U$ we refer to a more complete account of the dynamical maps [17].

## 2.1 General properties

Environments (also termed baths or reservoirs) can broadly be categorized into two categories: Markovian or non-Markovian. What does it mean? A Markovian bath is always in equilibrium with itself. Every kind of perturbation due to interaction with the system is damped out immediately. In physical terms this requires the environment to be really fast in damping out these perturbations. Therefore the bath needs to possess high-frequency components $\omega_{\text{env}}$ that are much larger than the system's typical frequencies $\omega_{\text{sys}}$, this it holds $\omega_{\text{env}} \gg \omega_{\text{sys}}$. If this requirement is fulfilled, than perturbations are damped out on timescales $\tau_{\text{env}}$ that are much smaller than the timescales $\tau_{\text{sys}}$ on which relevant dynamics in the system occur. This also can be seen as the bath being "memoryless". The system interacts with the same bath (in equilibrium) at each time step, thus the bath's density matrix can be approximated as constant $\rho_{\text{env}}(t) \equiv \rho_{\text{env}}(0)$. This phenomenological explanation is only supposed to set the stage, a more clear explanation of these approximations and why they are useful and sensible is given while deriving the Born-Markov master equation in Section 2.2.1.

Besides the distinction between different environments there is another common type of categorization for open quantum systems: the type of interaction between system and environment. This interaction can have different effects. Classically, an environment introduces friction (dissipation) and thus arranges an irreversible transfer of the system's energy to the bath. In the quantum world, there is also another possible effect that an environment can cause. Since the system can exhibit coherence properties, these can also be disturbed by an environment. The different type of interactions leading to these effects are highlighted below.

If the interaction is of the form

$$[H_{\text{sys}}, H_{\text{int}}] = 0 \tag{2.6}$$

then we have *decoherence without dissipation*, referring to the fact that the density matrix' off-diagonal elements decay. This is due to the evolution of an operator, given by

$$\frac{d}{dt}O(t) = -\frac{i}{\hbar}[H, O] \tag{2.7}$$

where $H$ is the total system plus environment Hamiltonian $H = H_{\text{sys}} + H_{\text{env}} + H_{\text{int}}$. When regarding the system's Hamiltonian $O = H_{\text{sys}}$ it of course interacts with itself and the environmental part. Thus when Eq. (2.6) is fulfilled as well the system's energy is a constant during time evolution and thus we have no dissipation. In quantum information language this setting is also known as quantum non demolition (QND). In the contrary case, when we have

$$[H_{\text{sys}}, H_{\text{int}}] \neq 0, \tag{2.8}$$

the result is *dissipation and coherence*, i.e. additionally to decoherence of the off-diagonal elements also the diagonal elements of the system's density matrix are subject to change.

## 2.2 Markovian evolution

In the following we will derive some equations that decribe systems subject to a Markovian environment. Therefore it is often useful to work in the interaction picture. The Hamiltonian is split up in two parts, $H = H_0 + H_I$ where $H_0 = H_{\text{sys}} + H_{\text{env}}$. By performing a unitary transformation, we separate the system- and environment-timescale given by $H_0$ from the interaction-timescale defined by $H_{\text{int}}$

$$\tilde{\rho}(t) = e^{\frac{i}{\hbar}H_0 t}\rho(t)\, e^{-\frac{i}{\hbar}H_0 t} \tag{2.9}$$

and denote the new interaction-picture operators by a tilde. Thus $\tilde{\rho}(0) = \rho(0)$. Inserting this into the von Neumann equation (2.2) yields the von Neumann equation in the interaction picture

$$\frac{d}{dt}\tilde{\rho}(t) = -\frac{i}{\hbar}\left[\tilde{H}_{\text{int}}, \tilde{\rho}(t)\right] \tag{2.10}$$

where

$$\tilde{H}_{\text{int}} = e^{\frac{i}{\hbar}H_0 t}H_{\text{int}}e^{-\frac{i}{\hbar}H_0 t}. \tag{2.11}$$

Formal integration of Eq. (2.10) gives

$$\frac{d}{dt}\tilde{\rho}(t) = \rho(0) - \frac{i}{\hbar}\int_0^t d\tau \left[\tilde{H}_{\text{int}}(\tau), \tilde{\rho}(\tau)\right] \tag{2.12}$$

and insertion of this result into Eq. (2.10) yields the integro-differential equation

$$\frac{d}{dt}\tilde{\rho}(t) = -\frac{i}{\hbar}\left[\tilde{H}_{\text{int}}(t), \rho(0)\right] - \frac{1}{\hbar^2}\int_0^t d\tau \ \left[\tilde{H}_{\text{int}}(t), \left[\tilde{H}_{\text{int}}(\tau), \tilde{\rho}(\tau)\right]\right]. \tag{2.13}$$

It should be noted that this equation is exact. The von Neumann equation has simply been recast into a form which enables us to easily apply approximations [13].

### 2.2.1 Born-Markov master equation

This will be the first open quantum system equation we derive [15]. It is also one of the simplest possible equations for open systems, subject to several restrictions, however still very useful in an astonishing number of scenarios. Since we are interested in the dynamics of the system only, we take the trace over the environment, resulting in

$$\begin{aligned}\frac{d}{dt}\tilde{\rho}_{\mathrm{sys}}(t) = &-\frac{i}{\hbar}\mathrm{tr}_{\mathrm{env}}\left(\left[\tilde{H}_{\mathrm{int}}(t), \rho(0)\right]\right) \\ &-\frac{1}{\hbar^2}\int_0^t d\tau\ \mathrm{tr}_{\mathrm{env}}\left(\left[\tilde{H}_{\mathrm{int}}(t), \left[\tilde{H}_{\mathrm{int}}(\tau), \tilde{\rho}(\tau)\right]\right]\right).\end{aligned} \tag{2.14}$$

Thereafter the following assumptions are made:

- System and environment are in a product state $\rho(0) = \rho_{\mathrm{sys}}(0) \otimes \rho_{\mathrm{env}}(0)$ at time $t = 0$, no correlations exist between these two parts. At time $t = 0$ the interaction is turned on.
- The first term on the right-hand side of Eq. (2.14) vanishes,

  $$\mathrm{tr}_{\mathrm{env}}\left(\left[\tilde{H}_{\mathrm{int}}(t), \rho(0)\right]\right) = 0. \tag{2.15}$$

  This is not really an assumption, since if it is not valid already it can always be ensured by moving the term $\mathrm{tr}_{\mathrm{env}}([H_{\mathrm{int}}, \rho_{\mathrm{env}}(0)])$ from the interaction Hamiltonian to the system Hamiltonian.
- The **Born approximation** holds, i.e. the complete state factorizes at all times

  $$\rho(t) \approx \rho_{\mathrm{sys}}(t) \otimes \rho_{\mathrm{env}} \tag{2.16}$$

  with the time-independent environment density matrix $\rho_{\mathrm{env}} \equiv \rho_{\mathrm{env}}(0)$. Physically this approximation corresponds to the assumption of a weak system-environment interaction as well as a sufficiently large environment. That way the environment remains largely undisturbed by the system and can be considered time-independent.

With these approximations we obtain the master equation in the form

$$\frac{d}{dt}\tilde{\rho}_{\mathrm{sys}}(t) = -\frac{1}{\hbar^2}\int_0^t d\tau\ \mathrm{tr}_{\mathrm{env}}\left(\left[\tilde{H}_{\mathrm{int}}(t), \left[\tilde{H}_{\mathrm{int}}(\tau), \tilde{\rho}_{\mathrm{sys}}(\tau) \otimes \rho_{\mathrm{env}}\right]\right]\right). \tag{2.17}$$

However, we still have a hard time solving this equation since it is time non-local. Specifically, the evolution of $\tilde{\rho}_{\mathrm{sys}}(t)$ depends on its past history $\tilde{\rho}_{\mathrm{sys}}(\tau)$. To circumvent this, the **Markov approximation** introduces the replacement $\tilde{\rho}_{\mathrm{sys}}(\tau) \to \tilde{\rho}_{\mathrm{sys}}(t)$ under the integral. Physically, this approximation requires that the timescale of the environment's memory (the correlation time, the time over which information is preserved in the environment) is much shorter than the relevant system relaxation timescale $\tau_{\mathrm{rel}}$.
To further eliminate the dependence on the initial time $t = 0$ in the integration's lower limit, the second Markov approximation substitues $\tau = t - s$ which to extend the time integration to infinity (with the same justification as before). This finally results in the *Born-Markov master equation*:

$$\frac{d}{dt}\tilde{\rho}_{\mathrm{sys}}(t) = -\frac{1}{\hbar^2}\int_0^\infty ds\ \mathrm{tr}_{\mathrm{env}}\left(\left[\tilde{H}_{\mathrm{int}}(t), \left[\tilde{H}_{\mathrm{int}}(t-s), \tilde{\rho}_{\mathrm{sys}}(t) \otimes \rho_{\mathrm{env}}\right]\right]\right) \tag{2.18}$$

or, with the commutator written out and a change of the integration variable

$$\frac{d}{dt}\tilde{\rho}_{\mathrm{sys}}(t) = -\frac{1}{\hbar^2}\int_0^\infty d\tau\ \mathrm{tr}_{\mathrm{env}}\Big[\tilde{H}_{\mathrm{int}}(t-\tau)\,\tilde{\rho}_{\mathrm{sys}}(t)\,\rho_{\mathrm{env}}\tilde{H}_{\mathrm{int}}(t) - \tilde{H}_{\mathrm{int}}(t)\,\tilde{H}_{\mathrm{int}}(t-\tau)\,\tilde{\rho}_{\mathrm{sys}}(t)\,\rho_{\mathrm{env}}\Big] + \mathrm{h.c.}\,. \tag{2.19}$$

This equation describes an open quantum system in the interaction picture, weakly coupled to a large environment that remains constant during the evolution. It has correlation times a lot smaller than those of the system, so that any fluctuations the system's presence induces in it are damped out immediately.

### 2.2.2 Lindblad equation

Starting from the Born-Markov master equation, we can proceed towards other descriptions, the first of which will be the master equation in Lindblad form [18]. Therefore it is convenient to preserve the generality of the interaction, but giving it a more specific form, suited for analytical treatment, by writing it as

$$H_{\mathrm{int}} = \sum_\alpha A_\alpha \otimes B_\alpha \tag{2.20}$$

where $A_\alpha = A_\alpha^\dagger$ and $B_\alpha = B_\alpha^\dagger$ are operators acting on the system and the environment, respectively. For further approximations it is convenient to expand the interaction Hamiltonian in the eigenbasis of the system Hamiltonian. Given a discrete spectrum of $H_{\mathrm{sys}}$ with eigenvalues $\varepsilon$, this is achieved by

$$A_\alpha(\omega) \equiv \sum_{\varepsilon'-\varepsilon=\omega} X(\varepsilon)\,A_\alpha X(\varepsilon')\,. \tag{2.21}$$

Indeed, this allows to recover the original operators $A_\alpha$, by employing the completeness relation, as

$$A_\alpha = \sum_\omega A_\alpha(\omega) = \sum_\omega A_\alpha^\dagger(\omega)\,. \tag{2.22}$$

Employing the new quantity $A_\alpha(\omega)$, the interaction Hamiltonian $H_{\mathrm{int}}$ receives the form

$$H_{\mathrm{int}} = \sum_{\alpha,\omega} A_\alpha(\omega)\otimes B_\alpha = \sum_{\alpha,\omega} A_\alpha(\omega)^\dagger \otimes B_\alpha^\dagger \tag{2.23}$$

which is the decomposition into eigenoperators of the system Hamiltonian that we desired.
The resulting commutation relation $[H_{\mathrm{sys}}, A_\alpha(\omega)] = -\omega A_\alpha(\omega)$ allows us to write the time evolution of the operator $A_\alpha(\omega)$ as

$$e^{\frac{i}{\hbar}H_{\mathrm{sys}}t}A_\alpha(\omega)\,e^{-\frac{i}{\hbar}H_{\mathrm{sys}}t} = e^{-i\omega t}A_\alpha(\omega)\,. \tag{2.24}$$

From here on we will omit the tilde to indicate the interaction picture. We are now able to express the interaction Hamiltonian (in the interaction picture) in the particularly simple form

$$H_{\mathrm{int}} = \sum_{\alpha,\omega} e^{-i\omega t}A_\alpha(\omega)\otimes B_\alpha(t) = \sum_{\alpha,\omega} e^{i\omega t}A_\alpha^\dagger(\omega)\otimes B_\alpha^\dagger(t) \tag{2.25}$$

where we introduced the interaction picture bath operators $B_\alpha(t)$ defined by

$$B_\alpha(t) = e^{\frac{i}{\hbar}H_{\text{env}}t} B_\alpha e^{-\frac{i}{\hbar}H_{\text{env}}t}. \tag{2.26}$$

Note that our assumption Eq. (2.15) from the previous section becomes

$$\langle B_\alpha(t)\rangle \equiv \text{tr}_{\text{env}}\left(B_\alpha(t)\,\rho_{\text{env}}\right), \tag{2.27}$$

stating that the environment average of $B_\alpha(t)$ vanishes.

Using this new form of the interaction Hamiltonian on the right-hand side of the Born-Markov master equation (2.19) yields

$$\begin{aligned}\frac{d}{dt}\rho(t) = &\sum_{\omega,\omega'}\sum_{\alpha,\beta} e^{i(\omega'-\omega)t}\,\Gamma_{\alpha,\beta}(\omega) \\ &\times\left[A_\beta(\omega)\,\rho(t)\,A_\alpha^\dagger(\omega') - A_\alpha^\dagger(\omega')\,A_\beta(\omega)\,\rho(t)\right] + \text{h.c.}\,.\end{aligned} \tag{2.28}$$

Here we adopted the convention $\hbar = 1$ which we will keep for the rest of this derivation to provide consistency with literature. Further from now on we denote $\rho = \rho_{\text{sys}}$, since any ambiguity is now excluded because the environment's part of the density matrix has been moved into $\Gamma_{\alpha,\beta}$, the one-sided Fourier transform

$$\Gamma_{\alpha,\beta}(\omega) = \int_0^\infty d\tau e^{i\omega\tau}\text{tr}_{\text{env}}\left(B_\alpha^\dagger(t)\,B_\beta(t-\tau)\,\rho_{\text{env}}\right), \tag{2.29}$$

of the *environment correlation functions*

$$\langle B_\alpha^\dagger(t)\,B_\beta(t-\tau)\rangle \equiv \text{tr}_{\text{env}}\left(B_\alpha^\dagger(t)\,B_\beta(t-\tau)\,\rho_{\text{env}}\right). \tag{2.30}$$

If the environment is in a stationary state, thus $[H_{\text{env}}, \rho_{\text{env}}] = 0$, these correlation functions are homogeneous in time and

$$\langle B_\alpha^\dagger(t)\,B_\beta(t-\tau)\rangle = \langle B_\alpha^\dagger(\tau)\,B_\beta(0)\rangle, \tag{2.31}$$

which then leads to time-independence of the $\Gamma_{\alpha,\beta}(\omega)$.

The Markov approximation relies on the fact that the environment correlation functions decay fast enough, on a timescale $\tau_{\text{env}}$ which is small compared to the system's relaxation time scale $\tau_{\text{rel}}$. It should be noted that this decay can only be strictly valid for an infinitely large environment involving a continuum of frequencies.
To further reduce terms, we now perform a secular approximation (in quantum optics known as rotating-wave approximation), which leads to the Master equation in Lindblad form.
Denoting the system's oscillation time scale by $\tau_{\text{sys}}$, defined by typical values of $|\omega' - \omega|^{-1}, \omega' \neq \omega$, it is possible to further simplify Eq. (2.28) and omit terms for which $\omega' \neq \omega$. This corresponds to neglecting the rapidly oscillating non-secular terms that vary quickly on the time scale $\tau_{\text{rel}}$ over which the system changes appreciably. In quantum optics this approximation is known as *rotating wave approximation*. With this approximation we obtain

$$\frac{d}{dt}\rho(t) = \sum_{\omega}\sum_{\alpha,\beta}\Gamma_{\alpha,\beta}(\omega)\left[A_\beta(\omega)\,\rho(t)\,A_\alpha^\dagger(\omega) - A_\alpha^\dagger(\omega)\,A_\beta(\omega)\,\rho(t)\right] + \text{h.c.}\,. \tag{2.32}$$

Upon further splitting $\Gamma_{\alpha,\beta}(\omega)$ into real an imaginary part as

$$\Gamma_{\alpha,\beta}(\omega) = \frac{1}{2}\gamma_{\alpha,\beta}(\omega) + iS_{\alpha,\beta}(\omega), \tag{2.33}$$

which allows to write the real part as

$$\gamma_{\alpha,\beta}(\omega) = \Gamma_{\alpha,\beta}(\omega) + \Gamma^*_{\alpha,\beta}(\omega) = \int_{-\infty}^{\infty} d\tau e^{i\omega\tau}\langle B^\dagger_\alpha(\tau) B_\beta(0)\rangle, \tag{2.34}$$

we receive the interaction picture *master equation in Lindblad form*

$$\begin{aligned}\frac{d}{dt}\rho(t) =& -i[H_{\mathrm{LS}}, \rho(t)] \\ &+ \sum_\omega \sum_{\alpha,\beta} \gamma_{\alpha,\beta}(\omega)\left(A_\beta(\omega)\rho(t)A^\dagger_\alpha(\omega) - \frac{1}{2}\{A^\dagger_\alpha(\omega)A_\beta(\omega), \rho(t)\}\right)\end{aligned} \tag{2.35}$$

with $H_{\mathrm{LS}}$ as the *Lamb shift* Hamiltonian

$$H_{\mathrm{LS}} = \sum_\omega \sum_{\alpha,\beta} \hbar S_{\alpha,\beta}(\omega) A^\dagger_\alpha(\omega) A_\beta(\omega) \tag{2.36}$$

commuting with $H_{\mathrm{sys}}$ and thus renormalizing the energy levels.

The master equation (2.35) is of the so-called first standard form. In addition to the microscopic derivation of the Lindblad equation above, it can also be derived from first principles, employing a quantum dynamical semigroup. This results in two possible forms, the first (and equivalent to the previously derived one) being the standard form

$$\frac{d}{dt}\rho(t) = -i[H, \rho(t)] + \sum_{i,j=1}^{N^2-1} a_{ij}\left(F_i\rho F^\dagger_j - \frac{1}{2}\{F^\dagger_j F_i, \rho(t)\}\right) \tag{2.37}$$

with $N = \dim(\mathcal{H}_{\mathrm{sys}})$ and $F_i$ for $i = 1, 2, \ldots, N^2$ a complete basis of orthonormal operators. The second form results from the diagonalization of the (positive) coefficient matrix $a = (a_{ij})$ and yields the diagonal form

$$\frac{d}{dt}\rho(t) = -i[H, \rho(t)] + \sum_{k=1}^{N^2-1} \gamma_k\left(A_k\rho(t)A^\dagger_k - \frac{1}{2}\{A^\dagger_k A_k, \rho(t)\}\right). \tag{2.38}$$

The right-hand side gives the most general form of an open quantum dynamical semigroup generator. The first term describes the unitary evolution of the dynamics the Hamiltonian $H$ generates. The operators $A_k$ are the Lindblad operators and can be expressed by the previous operators $F_i$ via linear combinations. The $\gamma_k$ are positive and, for dimensionless operators $A_k$, have the dimension of inverse time [15].

## 2.3 The Redfield equation

In the derivation of the Lindblad equation we proceeded from the Born-Markov equation by inserting Eq. (2.25) for the interaction Hamiltonian and performed a secular approximation. Now we will again start from the Born-Markov equation, but follow the

approach of [19], forego the secular approximation and employ an arbitrary basis $\{|a_n\rangle\}$. Starting from Eq. (2.19), we introduce the explicit form

$$H_{\text{int}} = \sum_{\alpha} A_\alpha(t) \otimes B_\alpha(t) \tag{2.39}$$

for the interaction Hamiltonian. This is in the interaction picture, thus the time-dependence of $A_\alpha$ and $B_\alpha$. We insert this in the Born-Markov equation, but this time omit the second Markov approximation. Renaming the integration variable to $t'$ and introducing the environment correlation functions as before yields for the system's density matrix $\rho = \rho_{\text{sys}}$

$$\begin{aligned}\frac{d}{dt}\rho(t) = \sum_{\alpha,\beta}\int_0^\infty dt' \Big[A_\alpha(t) A_\beta(t')\rho(t) - A_\beta(t')\rho(t)A_\alpha(t)\Big]\langle B_\alpha(t) B_\beta(t')\rangle \\ \times\Big[\rho(t)A_\beta(t')A_\alpha(t) - A_\alpha(t)\rho(t)A_\beta(t')\Big]\langle B_\beta(t')B_\alpha(t)\rangle.\end{aligned} \tag{2.40}$$

We now introduce the transformation $V = \sum_n |\omega_n\rangle\langle a_n|$ twice as $VV^\dagger$, with the eigenbasis $\{|\omega_n\rangle\}$ of the system Hamiltonian $H_{\text{sys}}$. For the first term in the equation above, after transforming back to the Schrödinger picture, this leads to

$$A_\alpha V V^\dagger e^{-iH_{\text{sys}}(t-\tau)} A_\beta e^{iH_{\text{sys}}(t-\tau)} V V^\dagger \rho(t) \tag{2.41}$$

for which we define its middle part as $Q = V^\dagger e^{-iH_{\text{sys}}(t-\tau)} A_\beta e^{iH_{\text{sys}}(t-\tau)} V$. Upon inserting the identity as $\sum_n |\omega_n\rangle\langle\omega_n|$ twice, $Q$ becomes

$$Q = \sum_{l,m,n,p} |a_l\rangle\langle\omega_l|e^{-iH_{\text{sys}}\tau}|\omega_m\rangle\langle\omega_m|A_\beta|\omega_n\rangle\langle\omega_n|e^{iH_{\text{sys}}\tau}|\omega_p\rangle\langle a_p| \tag{2.42}$$

where the first and third bra-ket-combination yield $\exp(-i\omega_l\tau)\,\delta_{l,m}$ and $\exp(-i\omega_n\tau)\,\delta_{n,p}$, respectively, finally yielding

$$Q = \sum_{m,n} |a_n\rangle\langle\omega_m|A_\beta|\omega_n\rangle\langle a_m| e^{i(\omega_n-\omega_m)\tau} \tag{2.43}$$

with elements

$$\langle a_m|Q|a_n\rangle = \langle\omega_m|A_\beta|\omega_n\rangle e^{i(\omega_n-\omega_m)\tau} = \langle a_m|V^\dagger A_\beta V|a_n\rangle e^{i(\omega_n-\omega_m)\tau}. \tag{2.44}$$

Upon performing these operations on all of the four terms, the final result, the *Bloch-Redfield equation*, reads in its most general form

$$\begin{aligned}\frac{d}{dt}\rho(t) = -\frac{i}{\hbar}[H,\rho(t)] + \frac{1}{\hbar^2}\sum_{\alpha,\beta}\Big[ - A_\alpha V q_{\alpha\beta} V^\dagger\rho(t) + V q_{\alpha\beta}V^\dagger\rho(t)A_\alpha \\ - \rho(t)V\hat{q}_{\alpha\beta}V^\dagger A_\alpha + A_\alpha\rho(t)V\hat{q}_{\alpha\beta}V^\dagger\Big]\end{aligned} \tag{2.45}$$

where $H = H_{\text{sys}}$ and the elements of $q_{\alpha\beta}$ and $\hat{q}_{\alpha\beta}$ are given by

$$\langle a_n|q_{\alpha\beta}|a_m\rangle = \langle a_n|V^\dagger A_\beta V|a_m\rangle D_{\alpha\beta}(\omega_m-\omega_n) \tag{2.46}$$

$$\langle a_n|\hat{q}_{\alpha\beta}|a_m\rangle = \langle a_n|V^\dagger A_\beta V|a_m\rangle D^*_{\alpha\beta}(\omega_n-\omega_m) \tag{2.47}$$

with

$$D_{\alpha\beta} = \int_0^\infty d\tau e^{i\omega\tau} \langle B_\alpha(\tau) B_\beta(0) \rangle. \tag{2.48}$$

Since imaginary terms in $D_{jk}(\omega)$ lead to additional coherent dynamics, only the real part causes decoherence. This real part can be Fourier transformed

$$\mathrm{Re}(D_{\alpha\beta}) = \frac{1}{2} C_{\alpha\beta} \tag{2.49}$$

$$C_{\alpha\beta}(\omega) = \int_{-\infty}^\infty d\tau e^{i\omega\tau} \langle B_\alpha(\tau) B_\beta(0) \rangle \tag{2.50}$$

where $\langle B_\alpha(-\tau) B_\beta(0) \rangle = \langle B_\alpha(\tau) B_\beta(0) \rangle^*$ has been assumed.
The Bloch-Redfield equation [20] is found in a wide variety of forms and shapes. For more detailed information and derivations see also [13, 15, 16].

## 2.4 Non-Markovian evolution

The system's reduced dynamics, emerging upon purging the environment, is in general non-Markovian. Thus the previous approaches are inherently restricted to a sub-class of physical settings, often excluding the most interesting ones. Thus a more general approach is desirable. The key feature of non-Markovianity is that an open system no longer irretrievably loses information to the environment, but such information can also flow back from the environment to the system. This suggests the environment possesses some kind of "memory". A general outline of concepts around environmental memory effects and non-Markovianity can be found in References [21, 22]. While a general theory and quantification of non-Markovianity has not been established yet, important steps in this direction have been made [23, 24, 25].

One approach towards capturing the non-Markovianity is the projection operator technique, addressing the non-Markovian dynamics in a systematic way. This is done by interpreting the trace over the environment, which yields the system's reduced dynamics, as a formal projection and using a projection operator to do so. The most well-known representative of the projection operator techniques is the Nakajima-Zwanzig equation derived below [26, 27, 28].

### 2.4.1 Nakajima-Zwanzig equation

The derivation of the Nakajima-Zwanzig equation starts, following the approach from Reference [29], from the Liouville equation

$$\frac{d}{dt}\rho = -\frac{i}{\hbar}[H, \rho] = \mathcal{L}\rho \tag{2.51}$$

where $\rho$ describes the complete system plus environment. To obtain a description of the reduced system $\rho_{\mathrm{sys}}$ we employ the projection operator $\mathcal{P}$ which projects only on the system's subspace and thus yields a description of only this system part. Since it is an projection operator the relation $\mathcal{P}^2 = \mathcal{P}$ holds; the (orthogonal) projection on the

environment thus can be defined by $\mathcal{Q} \equiv \mathbb{1} - \mathcal{P}$. Substituting $\rho = (\mathcal{P} + \mathcal{Q})\,\rho$ into Eq. (2.51) we obtain

$$\frac{d}{dt}\mathcal{P}\rho = \mathcal{P}\mathcal{L}\mathcal{P}\rho + \mathcal{P}\mathcal{L}\mathcal{Q}\rho \tag{2.52}$$

$$\frac{d}{dt}\mathcal{Q}\rho = \mathcal{Q}\mathcal{L}\mathcal{P}\rho + \mathcal{Q}\mathcal{L}\mathcal{Q}\rho \tag{2.53}$$

The second equation (2.53) can be solved formally yielding

$$\mathcal{Q}\rho = e^{\mathcal{Q}\mathcal{L}t}\mathcal{Q}\rho\,(t=0) + \int_0^t dt' e^{\mathcal{Q}\mathcal{L}t'}\mathcal{Q}\mathcal{L}\mathcal{P}\rho\,(t-t') \tag{2.54}$$

which in turn is substituted in Eq. (2.52) resulting in

$$\frac{d}{dt}\mathcal{P}\rho = \mathcal{P}\mathcal{L}\mathcal{P}\rho + \mathcal{P}\mathcal{L}e^{\mathcal{Q}\mathcal{L}t}\mathcal{Q}\rho(t=0) + \mathcal{P}\mathcal{L}\int_0^t dt' e^{\mathcal{Q}\mathcal{L}t'}\mathcal{Q}\mathcal{L}\mathcal{P}\rho(t-t'). \tag{2.55}$$

Here the second, inhomogeneous, term can be set to zero if we assume the initial state to be a product state.
Employing $\mathcal{P}^2 = \mathcal{P}$ and defining the *memory kernel* $\mathcal{K}(t)$ as

$$\mathcal{K}\,(t) = \mathcal{P}\mathcal{L}e^{\mathcal{Q}\mathcal{L}t}\mathcal{Q}\mathcal{L}\mathcal{P} \tag{2.56}$$

the final form of the Nakajima-Zwanzig equation for the relevant (system) part $\rho_{\text{sys}}$ is obtained as

$$\frac{d}{dt}\rho_{\text{sys}} = \mathcal{P}\mathcal{L}\rho_{\text{sys}} + \int_0^t dt' \mathcal{K}\,(t')\,\rho_{\text{sys}}\,(t-t') \tag{2.57}$$

This integro-differential equation involves an integral over the history of the reduced system though. While this equation is exact for the reduced system's relevant degrees of freedom and holds for all initial conditions $\rho_{\text{sys}}\,(0)$ and almost any type of system and interaction, it unfortunately is about as difficult to solve as the original Liouville equation for the total system. This usually leads to perturbative expansions to render numerical or analytical computations possible [15].

### 2.4.2 Extended approaches

Another famous variation of the projection operator technique is the time-convolutionless technique. It also yields an exact equation of motion that describes the evolution of the relevant part $\mathcal{P}\rho$. However, as opposed to the Nakajima-Zwanzig equation, it yields a time-local first-order differential equation. It expands the equation of motion with respect to the system-environment interaction strength and thus reaches regimes beyond the Born approximation. For further information we refer to Reference [15].

The Nakajima-Zwanzig equation itself also is a great starting point for further investigation. For example, under certain conditions, the transfer-tensor method presented in Chapter 7 is able to extract the memory kernel upon input of initial trajectories of the relevant part of the system and by that is able to propagate the system further in time. Later in that chapter we will present the amazing possibilities that this method leads to upon combining it with powerful numerical open quantum system-techniques, as i.e. those from Section 2.6.

## 2.5 The spin-boson model

Until now we introduced quite general tools to treat open quantum systems. Some assumptions about physical properties of the environment have been made, but no concrete modeling of its constituents or the form of interaction with it. While this is desirable to derive general-purpose tools, we now leave this restriction behind and move towards a more specific bath model.

The physically most intuitive assumption is to model the bath as an ensemble of harmonic oscillators. Usually this bath is coupled to a central two-level system (spin), giving rise to the *spin-boson model* (SBM). Since oscillators have sufficiently nice properties and tend to approximate physical scenarios sufficiently well, this assumption is able to describe an astonishingly large number of actual scenarios, but still is not too complex to be solved [30, 15]. By neglecting higher excitations it is especially suited to approximate many physically interesting systems in the low-temperature regime, as discussed thoroughly for the tunneling between two potential wells in Reference [31].

In a discrete setting, the total Hamiltonian $H = H_{\text{sys}} + H_{\text{env}} + H_{\text{int}}$ traditionally is constituted by the single contributions

$$H_{\text{sys}} = \frac{\omega_0}{2}\sigma_z \tag{2.58}$$

$$H_{\text{env}} = \sum_k \left( \frac{p_k^2}{2m_k} + \frac{1}{2} m_n \omega_k^2 x_n^2 \right) \tag{2.59}$$

$$H_{\text{int}} = -\frac{1}{2}\sigma_z \otimes \sum_k g_k x_k \tag{2.60}$$

where each of the environment's oscillators $k$ couples linearly via the operator $x_k$ with strength $g_k$ to the system operator $\sigma_z$. However, for our purposes it is much more suitable to give a continuous description [6] of the environment and interaction term, where the modes are labeled by some real number $x$, leading to the form

$$H = H_{\text{sys}} + \int_0^{x_{\max}} dx\ g(x)\, a_x^\dagger a_x + \int_0^{x_{\max}} dx\ h(x)\, A_{\text{sys}} \left( a_x + a_x^\dagger \right). \tag{2.61}$$

In a physical context, some continuous real variable – like the mode's momentum – can be expressed by $x$ with $x_{\max}$ as its maximum value present in the environment (which also could be infinity). The $a_x^\dagger$ and $a_x$ denote the bosonic creation and annihilation operators corresponding to the environmental mode $x$. The function $g(x)$ can be identified as the environmental dispersion relation, relating the oscillator's frequencies to the variable $x$. In the following we assume that $x$ and $g(x)$ both are bounded. The interaction term $H_{\text{int}}$ assigns each mode a coupling strength $h(x)$ between its displacement $(a_x^\dagger + a_x)$ and a general system operator $A$.
Together with the temperature, the functions $g(x)$ and $h(x)$ characterize the harmonic environment uniquely and define the *spectral density* $J(\omega)$ as

$$J(\omega) = \pi h^2 \left[ g^{-1}(\omega) \right] \frac{dg^{-1}(\omega)}{d\omega}. \tag{2.62}$$

The inverse of $g$ is given by $g^{-1}[g(x)] = x$. Thus in a physical interpretation, the spectral density is a combination of the density of environmental modes and the coupling strength of these modes to the system.

Since the environment is described in frequency space here, we can attribute every frequency slice $\delta\omega$ a density of states in the interval $\omega + \delta\omega$ for $\delta\omega \to 0$. This physical interpretation of the number of states present in the environment for a one such slice is given by

$$\frac{dg^{-1}(\omega)}{d\omega}\delta\omega. \tag{2.63}$$

Among the typical, often occurring spectral density is a Lorentzian peak with Drude cutoff [15]

$$J(\omega) = \lambda\gamma\frac{\omega}{\omega^2 + \gamma^2}, \tag{2.64}$$

where $\lambda$ is the system-environment coupling strength and $\gamma$ indicates some soft cutoff. A second, often found functional shape is

$$J(\omega) = 2\pi\alpha\omega_c^{1-s}\omega^s\theta(\omega - \omega_c). \tag{2.65}$$

with hard cutoff $\omega_c$, $\alpha$ the system-environment's dimensionless coupling strength and $\theta(\omega - \omega_c)$ the Heaviside step function. The cases of $s < 1$ are denoted as "sub-Ohmic" and those of $s > 1$ as "super-Ohmic" [32, 33].
The SBM itself is exceedingly difficult to integrate numerically in time due to the fact that large amount of entanglement build up in the system. We will not focus on any numerical or analytical solutions here, but instead refer to Section 3.4.1 where we introduce a way to make progress anyways, by introducing a transformation of this model which yields a configuration which is amenable to the application of methods from condensed matter physics and quantum information theory.

## 2.6 Further methods

Besides the presented open quantum system-methods, a range of versatile, numerically exact methods has been developed that often require considerable computational resources but in turn are able to deliver a far better description of a system interacting with an environment. Especially in the really hard regime, when intra-system coupling strengths are comparable to system-environment coupling strengths, these methods are indispensable. A prominent example of such systems where these numerical methods become incredibly useful are pigment-protein complexes in quantum biology. A large part of research around those complexes focuses on employing numerically exact treatments to reproduce experimental observations, as will be highlighted in more detail in Chapter 4. Some of the more prominent methods are introduced below.

Path Integral Monte Carlo (PIMC) combines Monte Carlo methods and a path integral description to provide a numerically exact method able to treat the spin-boson model at finite temperatures [34]. Towards low temperatures the Fermi sign problem increases the necessary computational effort, but nevertheless in many cases the quantum regime can still be reached.

Another path integral method is the quasi-adiabatic propagator path integral (QUAPI) [35, 36, 37]. It employs the path integral approach, based on an intelligent splitting

of the Hamiltonian instead of the standard splitting into kinetic and potential terms. Based thereon it derives an influence functional that decays on a short timescale if the spectral density is sufficiently smooth and slowly varying. This timescale increases for lower temperatures though, rendering these regimes computationally challenging due to multi-dimensional integrals that grow exponentially with the integration time.

Another popular method, invented by Kubo and Tanimura in 1989, is the hierarchy equations of motions (HEOM) [38, 39, 40]. It accounts for non-Markovian effects by introducing auxiliary density matrices, thus avoiding perturbative approximations. However it tends to be computationally expensive, especially in the case of low temperatures. Also it requires the environment's spectral density to be Lorentzian with a Drude cutoff. This is mitigated however due to the fact that many functions can be expressed as a sum of Lorentzian peaks and thus be treated by the HEOM formalism.

The present work develops and extends the relatively new TEDOPA scheme (see Section 3.4) which overcomes difficulties that other methods exhibit (i.e. in the low-temperature regime) and is establishing its place next to the previous methods as a numerically exact tool able to treat open quantum systems.

# CHAPTER 3

# Numerical preliminaries

In this section we introduce the numerical tools and principles which are constantly employed in the remainder of this thesis. We start out by carefully looking at the basic tools and its properties, quickly continuing towards advanced algorithms that provide a framework to deal with quantum many-body and open quantum systems.

## 3.1 Singular value decomposition

The singular value decomposition (SVD) is a crucial part of the numerical schemes developed in Section 3.3, thus we invest some time here to carefully cover its properties. The SVD is a method that factorizes a matrix $A \in \mathbb{C}^{m\times n}$ into three matrices $U \in \mathbb{C}^{m\times m}$, $S \in \mathbb{R}^{m\times n}$, and $V \in \mathbb{C}^{n\times n}$ where $U$ and $V$ are unitary and $S$ is diagonal. This factorization is possible for every matrix and can in some sense be seen as a generalization of the eigenvalue decomposition to arbitrary matrices. Due to the properties of the resulting three matrices, these can be interpreted as a rotation, followed by a shearing, followed by another rotation. This defines the most general action a matrix can have. Note that for $A \in \mathbb{R}^{n\times m}$ the matrices $U$ and $V$ can be chosen to be real.
The diagonal elements $\{\sigma_i\}$ of $S$ are usually ordered by size, thus $\sigma_1 \geq \sigma_2 \geq \cdots \geq \sigma_n$. They are uniquely determined by the non-negative square roots of the eigenvalues of $AA^\dagger$. The number of non-zero singular values is given by $k = \operatorname{rank}(A)$, upper bounded by $\min(m, n)$. The left (right) singular vectors are the eigenvectors of $AA^\dagger$ ($A^\dagger A$).

For a normal, positive semidefinite $n \times n$ matrix $A$ the singular values are equal to the eigenvalues. In general, however, this is not the case. Consider the simple example from the Matlab "gallery(3)" command

$$A = \begin{pmatrix} -149 & -50 & -154 \\ 537 & 180 & 546 \\ -27 & -9 & -25 \end{pmatrix}, \tag{3.1}$$

yielding an eigenvalue spectrum of $(3, 2, 1)$ but a singular value spectrum of $(817, 2.47, 0.003)$. This difference between SVD and eigenvalue decomposition is often played down, since

Hermitian matrices are ubiquitous in quantum mechanics and thus not much difference is seen in practice. However, some of the fundamental points are that the SVD uses two different sets of basis vectors instead of one, that the SVD uses bases which are orthonormal (which is in general not the case for the eigenvalue decomposition), and that the SVD exists for all matrices, as opposed to the eigenvalue decomposition.
Ultimately, the difference becomes visible in the various forms of applications. Methods that rely on iterated forms of the matrix $A$, such as the exponential $\exp(A)$ (for time evolution) or matrix powers $A^k$ (as in Krylov methods), tend to be determined by the eigenvalue spectrum. On the other hand, tasks that involve $A$ itself or its inverse, such as solving a system of linear equations $Ax = b$, are determined by the singular values [41, 42].

The SVD can also be used to define a matrix norm: The *spectral norm* is defined as the maximal singular value. Further it is useful to define a pseudo-inverse $A^p$ which approximates the inverse $A^{-1} \approx A^p$ of the matrix $A$ when it is non-existent: $A^p = V\tilde{S}U^\dagger$ where $\tilde{S}$ is a diagonal matrix with entries $A^p_{ii} = 1/\sigma_i$ for $\sigma_i \neq 0$ and $A^p_{ii} = 0$ otherwise. This definition has the additional benefit that it allows to introduce cutoffs for singular values that are below machine precision, as to not introduce some large numerical errors. Further applications of the SVD include challenges such as least squares fitting, principle component analysis, or to determine rank, range, and null space of a matrix.
Errors in $A$ directly lead to errors in the diagonal matrix $S$. The SVD of a matrix $\tilde{A}$ with $\tilde{A} = A + \delta A$ (where $\delta A$ is some error with $\|\delta A\| \leq \eta \|A\|$ and generally $\eta \ll 1$) yields singular values $\{\tilde{\sigma}_i\}$ with $|\sigma_i - \tilde{\sigma}_i| \leq \eta\|A\| = \eta\sigma_1$ (employing the spectral norm) [43]. Another important property, quantified by the SVD, is the condition number $\kappa(A)$ of a matrix $A$, defined as the largest singular value divided by the smallest, $\kappa \equiv \sigma_1/\sigma_n$.

Since $A^\dagger A = VS^\dagger SV^\dagger$, a straight-forward way to compute the SVD would be to build $A^\dagger A$, perform the eigenvalue decomposition $A^\dagger A = VDV^\dagger$, find $S$ as the $m \times n$ non-negative diagonal square root of S and solve $US = AV$ for a unitary matrix U (i.e. by QR-factorization). Yet this approach, based on the *covariance matrix* $A^\dagger A$, is unstable due to the reduction to a possibly much more sensitive eigenvalue decomposition. A stable method is given by computing the eigenvalues of the matrix $A'$ defined by

$$A' = \begin{pmatrix} 0 & A^\dagger \\ A & 0 \end{pmatrix}. \tag{3.2}$$

It can be shown that the singular values of $A$ are equal to the absolute values of the eigenvalues of $A'$. Further the singular vectors pertaining to $A$ can be extracted from the eigenvectors of $A'$ [41].
Standard algorithms mimic this trick in a two-step process. In a first step, the matrix $A$ is brought into bidiagonal form, requiring $\mathcal{O}(m \cdot n^2)$ flops. This is easily performed, i.e. by a Golub-Kahan bidiagonalization, which applies Householder reflectors from both sides alternately. In a second step the SVD of this bidiagonal matrix is determined. While this procedure in principle requires an infinite number of operations, only a finite number $\mathcal{O}(n)$ steps is required to reach machine precision. Traditionally this second step is done by performing a QR decomposition, yet more advanced schemes employ a divide-and-conquer algorithm here [41].

## 3.2 Orthogonal polynomials

Covering orthogonal polynomials, we lay some ground work for the introduction of the TEDOPA algorithm in Section 3.4. The algorithm is based on a mathematical transformation of the underlying physical system, relying heavily on orthogonal polynomials, largely drawing on the definitions and properties given below. A large part of the formulae in this section are developed in analogy to [6]. It also presents a more extensive, mathematical treatment of this matter which exceeds the scope of this work.

We define an orthogonal polynomial $p_n(x)$ of degree $n$ as

$$p_n = \sum_{i=0}^{n} a_i x^i \tag{3.3}$$

with the coefficients $a_i \in \mathbb{R}$ and $x$ being some real variable. We then employ the *measure* $d\mu(x)$ resulting from a non-decreasing and differentiable function $\mu(x)$ on some interval $[a, b] \in \mathbb{R}$ that has finite moments of all orders $r$,

$$\int_a^b x^r d\mu\,(x) \leq \infty, \qquad r = 0, 1, 2, \dots\ . \tag{3.4}$$

With this measure we are able to define, for two polynomials $p(x)$ and $q(x)$, an inner product as

$$\langle p, q\rangle_\mu = \int_a^b d\mu\,(x)\, p\,(x)\, q\,(x)\,. \tag{3.5}$$

This in turn yields a norm via

$$\|p\|_\mu = \sqrt{\langle p, p\rangle_\mu} = \left(\int_a^b p^2\,(x)\, d\mu\,(x)\right)^{\frac{1}{2}} \geq 0. \tag{3.6}$$

Thus the orthogonality of two polynomials $p$ and $q$ can be defined by requiring its inner product to be zero.

If for some polynomial $p_n(x)$ the leading coefficient $a_n = 1$, then this polynomial is called *monic* and will be denoted by $\pi_n(x)$. Of course every polynomial can be made monic, simply by dividing it by its leading coefficient. The orthogonality relation changes then though, it becomes

$$\langle \pi_n, \pi_m\rangle_\mu = \|\pi_n\|_\mu^2 \delta_{n,m}, \quad n, m = 0, 1, 2, \dots\ . \tag{3.7}$$

The non-monic form can be restored via $p_n(x) = \pi_n(x)/\|\pi_n\|$.
For any non-zero measure $d\mu(x)$, a unique family of monic orthogonal polynomials can be constructed. An easy way to do so is to perform the Gram-Schmidt orthogonalization procedure on the sequence $\{1, x, x^2, \dots\}$. The non-monic version of this sequence is often used; the corresponding orthogonality relation is

$$\int_a^b d\mu\,(x)\, p_m\,(x)\, p_n\,(x) = \delta_{m,n}. \tag{3.8}$$

Another incredibly useful property is the *recurrence relation*. It can be shown that every set of monic orthogonal polynomials with respect to the measure $d\mu(x)$ exhibits a recurrence relation

$$\pi_{k+1} = (x - \alpha_k)\,\pi_k(x) - \beta_k \pi_{k-1}(x), \qquad k = 0, 1, 2, \ldots \tag{3.9}$$

with $\pi_{-1}(x) \equiv 0$ and the *recurrence coefficients*

$$\alpha_k = \frac{\langle x\pi_k, \pi_k\rangle}{\langle \pi_k, \pi_k\rangle} \tag{3.10}$$

$$\beta_k = \frac{\langle \pi_k, \pi_k\rangle}{\langle \pi_{k-1}, \pi_{k-1}\rangle}. \tag{3.11}$$

The corresponding relation for the non-monic case is given by

$$\tilde{p}_{k+1}(x) = (C_k x - A_k)\,\tilde{p}_k(x) - B_k \tilde{p}_{k-1}, \qquad k = 0, 1, 2, \ldots \tag{3.12}$$

with $\tilde{p}_{-1}(x) \equiv 0$. The coefficients of both these recurrence relations are related by

$$A_k = \frac{\alpha_k}{\sqrt{\beta_{k+1}}} \tag{3.13}$$

$$B_k = \frac{\sqrt{\beta_k}}{\sqrt{\beta_{k+1}}} \tag{3.14}$$

$$C_k = \frac{1}{\sqrt{\beta_{k+1}}}. \tag{3.15}$$

A stable numerical procedure to calculate these recurrence coefficients can be found in [44], with both Fortran and Matlab implementations freely available. Several routines provide useful features around orthogonal polynomials, like the *mcdis*-routine which returns the recurrence coefficients given a measure $d\mu(x)$. For further applications (see Section 3.4.1) it is especially important that this routine is able to handle both discrete features as well as a superposed functional background.

For testing purposes it is convenient to be able to verify the obtained results, checking for convergence or errors. This can easily be done by arranging the recurrence coefficients in the Jacobi matrix

$$J = \begin{pmatrix} \alpha_0 & \sqrt{\beta_0} & & & \\ \sqrt{\beta_0} & \alpha_1 & \sqrt{\beta_1} & & \\ & \sqrt{\beta_1} & \ddots & \ddots & \\ & & \ddots & \alpha_{n-1} & \sqrt{\beta_{n-1}} \\ & & & \sqrt{\beta_{n-1}} & \alpha_n \end{pmatrix}. \tag{3.16}$$

The $x$-coordinates are given by the eigenvalues of the matrix $J$, the $k$'th $y$-coordinate by the first element of the $k$'th eigenvector $v_k$ of $J$, thus $y(k) = v_k(1)$.

## 3.3 Time evolving block decimation

The Time Evolving Block Decimation (TEBD) algorithm in its basic formalism is an algorithm that is able to handle pure states of one-dimensional quantum systems, subject to a nearest-neighbor Hamiltonian. For these systems it can obtain their ground

states (via an imaginary time evolution, for non-degenerate ground states), perform time evolutions, apply gates and perform measurements [45, 46, 47].
Its capabilities are based on the following points. The ability to store the quantum state efficiently is due to the description as a matrix product state, reducing the number of coefficients that need to be stored from an exponential to a polynomial number. How, why, and when this is possible is discussed in Section 3.3.1. The next ingredient is the ability to perform time evolutions. This is possible due to the invention of an efficient two-site update procedure for a matrix product state, applied together with a splitting scheme exploiting the nearest-neighbor structure of the Hamiltonian, thus enabling a variety of evolutions. Finally the prescription of how to perform measurements on the matrix product states completes the simulation framework.
Most of the restrictions are mitigated or removed by appropriate extensions of the TEBD formalism. This includes such as infinite-size systems (with a translational invariance) [48], multi-dimensional systems [49, 50], and thermal states [51].

### 3.3.1 Matrix product states

The usual description of pure quantum state of a chain of $N$ quantum systems, or *sites*, in terms of the coefficients $c_{i_1 i_2 \ldots i_N}$, is given by

$$|\psi\rangle = \sum_{i_1, i_2, \ldots, i_N} c_{i_1 i_2 \ldots i_N} \; |i_1 i_2 \ldots i_N\rangle. \tag{3.17}$$

Each site is assumed to possess $d$ levels. This yields $d^N$ coefficients necessary to describe the state. In order to reduce this polynomial amount of coefficients, one can introduce a *matrix product state* (MPS) consisting of matrices $A^{[k] i_k}$ for each site $k \in [1, N]$ for each state $i_k \in [0, d_k - 1]$ (with $d_k$ as dimension of site $k$). For notational convenience from now on we consider all dimensions $d_k$ to be equal, $d_k = d$, without affecting the generality of the procedure. The state now can be described by a function of these matrices $A$ as

$$|\psi\rangle = \sum_{i_1, i_2, \ldots, i_N} f\left(A^{[1]}_{i_1} A^{[2]}_{i_2} \ldots A^{[N-1]}_{i_{N-1}} A^{[N]}_{N}\right) \; |i_1 i_2 \ldots i_N\rangle. \tag{3.18}$$

The function $f(\cdot)$ determines the boundary conditions of this one-dimensional system, at the same time limiting the matrix sizes to a certain degree. For periodic boundary conditions (PBC) – i.e. site 1 bonds to the left to site $N$, thus essentially forming a ring – the function $f(\cdot)$ is the trace. This yields arbitrarily large matrix sizes for the MPS with the constraint that the number of rows $\alpha_1$ of the matrices of site 1 has to be equal to the number of columns $\alpha_N$ of the matrices assigned to site $N$. For open boundary conditions (OBC) on the other hand, the leftmost matrices are row vectors and the rightmost ones are column vectors, requiring $\alpha_1 = \alpha_N = 1$. While in the case of PBC often (at least after some simulation time) every matrix has the same dimensions $\chi \times \chi$ (if a finite cutoff $\chi$ for these matrices has been enforced), for an OBC MPS the matrix sizes (starting from the left) are $1 \times d$, $d \times d^2$, $d^2 \times d^3, \ldots$ until at most $d^{\lceil \frac{N}{2} \rceil}$, then shrinking in reversed order until $d \times 1$ [52]. In the following we will restrict our notation and analysis to OBC.

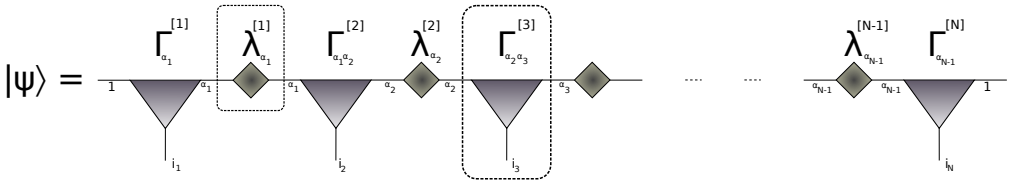


Figure 3.1: Graphical representation of the state $|\psi\rangle$ as an MPS in Vidal form. The triangles correspond to the matrices $\Gamma$, the three lines connected to one triangle indicate its indices (two to the neighboring $\lambda$-matrices and one open, "physical" index). The squares denote the $\lambda$-matrices assigned to these "bonds". The left and right 1-index indicates OBC.

An equivalent form of the MPS is given in the *Vidal form*. The coefficients from Eq. (3.17) are rewritten like in Eq. (3.18), but with matrices $\Gamma^{[k]i_k}$ instead of $A^{[k]i_k}$ and some additional matrices $\lambda^{[k]}$, yielding

$$c_{i_1 i_2 \ldots i_N} = \sum_{\alpha_1, \alpha_2, \ldots, \alpha_{N-1}} \Gamma^{[1]i_1}_{\alpha_1} \lambda^{[1]}_{\alpha_1} \Gamma^{[1]i_1}_{\alpha_1 \alpha_2} \cdots \Gamma^{[N-1]i_{N-1}}_{\alpha_{N-2}\alpha_{N-1}} \lambda^{[N-1]}_{\alpha_{N-1}} \Gamma^{[N]i_N}_{\alpha_{N-1}}. \tag{3.19}$$

Similar to the previous form, the matrix $\Gamma^{[k]i_k}$ is assigned to site $k$ in state $i_k$. Each of the additional matrices $\lambda^{[k]}$ is assigned to the bond $k$ that connects sites $k$ and $k+1$, compare also Fig. 3.1. Bond $k$ thus has at most dimension $\chi_k^{\max} = d^k$. This form can always be achieved by performing successive Schmidt decompositions (see Eq. (3.20) below) which yield the diagonal matrices $\lambda^{[k]}$ with the Schmidt values on the diagonal.

Matrix product states have first been introduced by Rommer and Östlund in 1997 [53] and have since become a general-purpose tool, especially in condensed matter and numerical applications. While the concept is inherently appealing, we still need to show its viability. Indeed, some given state can *always* be written as an MPS, given that the matrix dimensions $\chi$ are large enough. This description is only *efficient* though if the matrix dimensions are restricted sufficiently. Only then MPS are an incredibly useful tool [54, 46].
The condition for this is that only low entanglement is present in the system, as can be seen directly from their relation to the Schmidt decomposition

$$|\psi\rangle = \sum_i \lambda_i |\psi\rangle_i^A |\psi\rangle_i^B. \tag{3.20}$$

Here the $|\psi\rangle_i$ constitute a complete set of basis states (the Schmidt vectors) for the spaces $A$ and $B$, respectively, and $\sum_i \lambda_i^2 = 1$ with non-negative real numbers $\lambda_i$ [17]. This splits the quantum state into products of states with constituents residing in subspaces $A$ and $B$ of the total Hilbert space, with the values $\lambda_i$ characterizing the entanglement properties of the state between these two subspaces. The less values $\lambda_i$ are non-zero and the faster they decay, the less the state is entangled. This also means that the matrices $\lambda^{[k]}$ of the MPS are sufficiently small and thus the total number of coefficients necessary to store the state is manageable. Luckily this is the case for plenty of interesting cases. While for completely random states the decay of Schmidt values will be linearly, for

systems exhibiting a certain kind of structure this decay will usually be exponential – offering the possibility of an early cutoff without loosing too much accuracy. The fact of exponentially decaying Schmidt values is often observed in many-body systems. It relates to the inherent, underlying structure – the system (even if exhibiting complex properties) yet is far different from a completely random state. Especially states like lowly entangled states or states near the ground state (for gapped systems, i.e. systems with a finite gap between the two states of lowest energy) offer these possibilities. These considerations can be made more rigorous by considering *area laws* [55, 56, 57, 58, 59, 60, 61].
When dealing with actual simulations, the question of how to obtain the initial state arises. In theory an MPS can be constructed from a given state vector [47]. However, usually this is not necessary. And for large states it is also not feasible due to limited memory and storage (which already is insufficient to store the state alone). In practice we do not have these problems though. Simple states, like the factorizable $|001\ldots0110\rangle$ or such, can be written down manually. Some states also exhibit a non-trivial, exact MPS representation, like the ground state of the AKLT-Hamiltonian, the GHZ-states, or the W-states [52]. Ground states can be obtained by performing an imaginary time evolution that starts from some completely random state [46]. Thus all states that are commonly used as initial states to start a time evolution are accessible without transforming the complete state vector into an MPS.

### 3.3.2 Gate applications

Now that we are able to store some state efficiently as a matrix product, the next relevant ingredient is a rule of how to update it. Let us start out with a single-site operator (or gate) $A$ acting on the state $|\psi\rangle$. We assume to have the gate represented in the basis of the MPS, thus

$$A = \sum_{i,j} A_{ij}|i\rangle\langle j| = \sum_{i,j}\langle i|A|j\rangle|i\rangle\langle j| \tag{3.21}$$

or, analogous for a two-site gate,

$$A = \sum_{i_1,i_2}\sum_{j_1,j_2}\langle i_1 i_2|A|j_1 j_2\rangle|i_1 i_2\rangle\langle j_1 j_2| \tag{3.22}$$

For simplicity we denote by $\{i_n\}$ the summations over $i_1$ until $i_N$ and by $\{\alpha_n\}$ those from $\alpha_1$ until $\alpha_{N-1}$, yielding for the application of gate $A$ acting only on site $l$ the expression

$$\begin{aligned} A|\psi\rangle = &\sum_{\{i_n\}}\sum_{\{\alpha_n\}}\Gamma^{[1]i_1}_{\alpha_1}\ldots\lambda^{[l-1]}_{\alpha_{l-1}}\Gamma^{[l]i_l}_{\alpha_{l-1}\alpha_l}\lambda^{[l]}_{\alpha_l}\ldots\Gamma^{[N]i_N}_{\alpha_{N-1}} \\ &\times|i_1\ldots i_{l-1}\rangle A|i_l\rangle|i_{l+1}\ldots i_N\rangle. \end{aligned} \tag{3.23}$$

By introducing an identity for site $l$, we manage to extract the action of the operator and move it into the matrix product

$$\begin{aligned} A|\psi\rangle = &\sum_{\{i_n\}}\sum_{\{\alpha_n\}}\Gamma^{[1]i_1}_{\alpha_1}\ldots\lambda^{[l-1]}_{\alpha_{l-1}}\left(\sum_{j_l}\langle j_l|A|i_l\rangle\Gamma^{[l]i_l}_{\alpha_{l-1}\alpha_l}\right)\lambda^{[l]}_{\alpha_l}\ldots\Gamma^{[N]i_N}_{\alpha_{N-1}} \\ &\times|i_1\ldots i_{l-1}\rangle|j_l\rangle|i_{l+1}\ldots i_N\rangle. \end{aligned} \tag{3.24}$$

After switching the summations of $i_l$ and $j_l$, as well as interchanging $i_l$ and $j_l$, we obtain the matrix product in a similar form as before (Eq. (3.23))

$$A|\psi\rangle = \sum_{\{i_n\}} \sum_{\{\alpha_n\}} \Gamma^{[1]i_1}_{\alpha_1} \dots \lambda^{[l-1]}_{\alpha_{l-1}} \left( \sum_{j_l} \langle i_l|A|j_l\rangle \Gamma^{[l]j_l}_{\alpha_{l-1}\alpha_l} \right) \lambda^{[l]}_{\alpha_l} \dots \Gamma^{[N]i_N}_{\alpha_{N-1}} |i_1 \dots i_N\rangle \quad (3.25)$$

and thus can identify the action of the gate $A$ as

$$\tilde{\Gamma}^{[l]i_l}_{\alpha\beta} = \sum_{j_l} \langle i_l|A|j_l\rangle \Gamma^{[l]j_l}_{\alpha\beta} \quad \forall\ \alpha, \beta \quad (3.26)$$

Note that this procedure does only update the MPS locally. An operator acting on site $l$ only changes the matrices belonging to this specific site, rendering this update not only feasible but even highly efficient.

Now that the procedure of how to apply a single-site operator is clear, we proceed to the more important case of two-site operators. Given a nearest-neighbor Hamiltonian, the ability to apply two-site operators will enable us to perform a time evolution on the MPS (see Section 3.3.6).
Since we already know that the action of such an operator is local, we restrict the MPS description to the sites $l$ and $l+1$ that the operator $A$ acts, retaining the Schmidt vectors $|\Phi\rangle$ for the remaining pats of the state. This gives

$$\begin{aligned} |\psi\rangle &= \sum_{i_l, i_{l+1}} \sum_{\alpha_{l-1}, \alpha_l, \alpha_{l+1}} \left( \lambda^{[l-1]}_{\alpha_{l-1}} \Gamma^{[l]i_l}_{\alpha_{l-1}\alpha_l} \lambda^{[l]}_{\alpha_l} \Gamma^{[l+1]i_{l+1}}_{\alpha_l\alpha_{l+1}} \lambda^{[l+1]}_{\alpha_{l+1}} \right) |\Phi^{[i_1 \dots i_{l-1}]}\rangle |i_l i_{l+1}\rangle |\Phi^{[i_{l+2} \dots i_N]}\rangle \\ &= \sum_{i_l, i_{l+1}} \sum_{\alpha_{l-1}, \alpha_{l+1}} \Theta^{i_l i_{l+1}}_{\alpha_{l-1}\alpha_{l+1}} |\Phi^{[i_1 \dots i_{l-1}]}\rangle |i_l i_{l+1}\rangle |\Phi^{[i_{l+2} \dots i_N]}\rangle \end{aligned} \quad (3.27)$$

with the (fourth order) tensor $\Theta$ as

$$\Theta^{i_l i_{l+1}}_{\alpha_{l-1}\alpha_{l+1}} = \sum_{\alpha_l} \lambda^{[l-1]}_{\alpha_{l-1}} \Gamma^{[l]i_l}_{\alpha_{l-1}\alpha_l} \lambda^{[l]}_{\alpha_l} \Gamma^{[l+1]i_{l+1}}_{\alpha_l\alpha_{l+1}} \lambda^{[l+1]}_{\alpha_{l+1}}. \quad (3.28)$$

This tensor can be seen as a compound that represents sites $l$ and $l+1$, thus it is updated the same way as a single-site gate in Eq. (3.26), yielding

$$\tilde{\Theta}^{i_l i_{l+1}}_{\alpha\beta} = \sum_{j_l j_{l+1}} \langle i_l i_{l+1}|A|j_l j_{l+1}\rangle \Theta^{j_l j_{l+1}}_{\alpha\beta} \quad \forall\ \alpha, \beta. \quad (3.29)$$

Unfortunately this procedure delivers only an updated tensor $\tilde{\Theta}$ and thus does not retain the MPS structure with $\Gamma$-matrices for sites $l$ and $l+1$. Therefore the tensor $\Theta$ needs to be split in some way to re-create the MPS structure with updated matrices $\tilde{\Gamma}^{(l)}$ and $\tilde{\Gamma}^{(l+1)}$. This can be done similar to the way an MPS is obtained from a state – by employing a SVD. It breaks up the tensor $\Theta$ in such a way that we obtain two sets of new matrices, $\tilde{\Gamma}^{[l]i_l}$ and $\tilde{\Gamma}^{[l]i_l}$, with a common diagonal matrix $\tilde{\lambda}^{[l]}$ in between (illustrated in Fig. 3.2). By multiplying the inverse of the outer matrices $\lambda^{[l-1]}$ and $\lambda^{[l+1]}$ we can fully restore the previous structure Eq. (3.27) and complete the update [45].

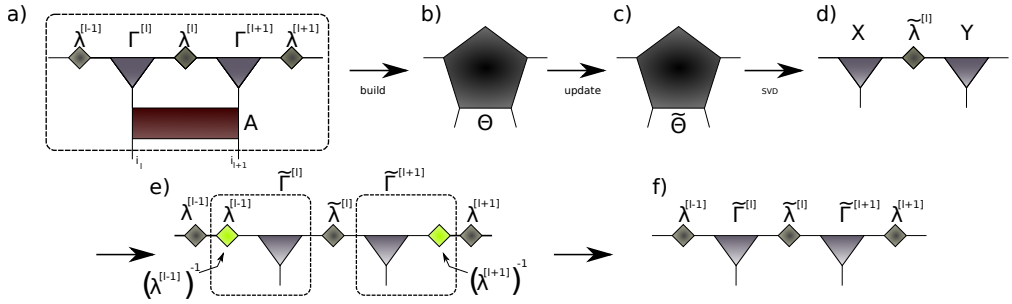


Figure 3.2: Application of the two-site update $A$ on the MPS (a). First the constituents are contracted to the tensor $\Theta$ (b) which is then updated (c) and singular value decomposed (d). To obtain the original structure, the inverse of the outer matrices $\lambda$ are introduced (e) and the according parts are contracted, yielding the original structure (f).

Upon checking carefully the dimensions of the new matrices $\tilde{\Gamma}^{[l]}$ and $\tilde{\Gamma}^{[l+1]}$, one immediately sees that the dimension $\tilde{\chi}_l$ of the updated diagonal matrix $\tilde{\lambda}^{[l]}$ (of bond $l$) has grown by a factor of $\min(d_l, d_{l+1})$. And since the adjacent matrices of the MPS have the same dimension, subsequent updates on them propagate this growth of the matrices through the whole MPS. For periodic boundary conditions this spread is in principle unlimited, for open boundary conditions it is upper bounded by $d^{N/2}$ (due to the structure of the $\theta$-matrix). This is not acceptable already for small systems, much less larger ones. Thus in practice one introduces an upper bound $\tilde{\chi}_{\mathrm{l,max}}$ for $\tilde{\chi}_l$ which is enforced once it has been exceeded. The $\tilde{\chi}_l - \tilde{\chi}_{\mathrm{l,max}}$ smallest singular values are simply discarded, leaving $\tilde{\lambda}^{(l)}$ with a dimension sufficiently small to allow computations but still capturing and describing the relevant part of the quantum system. This of course holds especially for the cases, as highlighted above, where an MPS is able to faithfully describe a quantum state. A more refined treatment of the error this approximation incurs is given in Section 3.3.7. As long as the employed update $A$ represents a unitary evolution, the orthogonalization properties of the Schmidt decomposition (here performed by the SVD) already deliver the elements $\tilde{\lambda}_i^{llrrql}$ in a normalized form (their squared sum is 1). If this is not the case, however, this normalization needs to be performed manually [45]. One example where this becomes necessary are imaginary time evolutions employed to build ground and thermal states.

### 3.3.3 Implementation and scaling considerations

Since the two-site update, especially with the SVD it employs, is usually the costliest part of the simulation process, it is worthwhile to optimize it as thoroughly as possible. For the present analysis we will count basic operations (additions and multiplications) to determine the cost of the single parts of the update process. These considerations are of fundamental nature and thus deliberately exclude speed-ups like those yielded by vectorization of operations, as performed in modern processors.

The first expensive step is to build the matrix $\Theta$, requiring a time $t$ about

$$t_{\mathrm{build}(\Theta)} = \mathcal{O}\left(d_l \cdot d_r \cdot \chi^3\right) \tag{3.30}$$

The next step is the update of the matrix $\Theta$ to the matrix $\tilde{\Theta}$, performed by applying the two-site gate $A$ (as in Eq.(3.29)). The matrix $\Theta$ consists of $d_l d_r \chi^2$ elements and its update includes sums over $d_l$ and $d_r$ each - thus the total operation count delivers

$$t_{\text{update}(\Theta)} \propto \mathcal{O}\left(d_l^2 \cdot d_r^2 \cdot \chi^2\right) \tag{3.31}$$

The sum in Eq. (3.29) over $d_l$ and $d_r$ requires $d_l \cdot d_r$ basic operations. However, Hamiltonians are often sparse; for the ordinary spin-boson two-site gate the number of non-zero elements drops to less than 10% at $d = 8$ dimensions of the environmental oscillators. This can reduce the operation count for the update-step by a full order of magnitude.
The last step to consider is the SVD. Since for an $m \times n$-matrix it scales with $\mathcal{O}\left(m \cdot n^2\right)$, the total scaling is $d_l \cdot d_r^2 \cdot \chi^3$, yielding

$$t_{\text{svd}(\Theta)} \propto \mathcal{O}\left(d_l \cdot d_r^2 \cdot \chi^3\right). \tag{3.32}$$

The scalings presented in Vidal's original work [46] were intended for qubit-based problems and thus ignored the dimensional component in the scaling analysis. However, especially for TEDOPA-based simulations, $d$ may lie in a far broader range and this scaling behaviour becomes quite non-trivial. Setting the stage for Chapter 8, consider the scaling for oscillators of dimension $d = 7$ for a mixed-state simulation (see below), leading to $d_l = d_r = 49$. When setting them to 50 for the sake of easier computability, we obtain $t_{\text{build}(\Theta)} \approx 2.5 \cdot 10^9$ with $t_{\text{update}(\Theta)} \approx 6.25 \cdot 10^{10}$ and $t_{\text{svd}(\Theta)} \approx 1.25 \cdot 10^{11}$.
Now imagine we manage to reduce the time the SVD takes considerably (possibly more than an order of magnitude). Then suddenly the update of the $\Theta$-matrix is the costliest step! The above reduction of the update-step by one order of magnitude then puts all three contributions on equal footing.

### 3.3.4 Measurements

Performing measurements, i.e. calculating the expectation value of the operator $O = A_k \otimes B_l$ where $A$ acts on site $k$ and $B$ on site $l$, is given by $\langle\psi|O|\psi\rangle$. The calculation of this quantity is straight-forward in the MPS picture. Since Hermitian conjugation yields the bra $\langle\psi|$ and the action of the operators $A$ and $B$ on the MPS are known, we can write down the full formula for this expectation value as

$$\begin{aligned}\langle\psi|O|\psi\rangle = &\sum_{i_1,\ldots,i_N} \left( \sum_{\beta_1,\ldots,\beta_N} \Gamma^{[1]i_1}_{\alpha_1} \lambda^{[1]}_{\alpha_1} \Gamma^{[2]i_2}_{\alpha_1\alpha_2} \ldots \Gamma^{[N-1]i_{N-1}}_{\alpha_{N-2}\alpha_{N-1}} \right) \\ &\times \left( \sum_{\alpha_1,\ldots,\alpha_{N-1}} \Gamma^{[1]i_1}_{\alpha_1} \ldots \left[ \sum_{j_k} \langle i_k|A|j_k\rangle \Gamma^{[k]j_k}_{\alpha_{k-1}\alpha_k} \right] \ldots \left[ \sum_{j_l} \langle i_l|B|j_l\rangle \Gamma^{[l]j_l}_{\alpha_{l-1}\alpha_l} \right] \ldots \Gamma^{[N]i_N}_{\alpha_{N-1}} \right).\end{aligned}$$

Reordering the sums and regrouping the single terms leads to

$$\begin{aligned}\langle\psi|O|\psi\rangle = &\sum_{\beta_1\ldots\beta_N} \sum_{\alpha_1,\alpha_2,\ldots,\alpha_{N-1}} \left( \sum_{i_1} \lambda^{[1]}\beta_1 \Gamma^{[1]i_1}_{\beta_1} \Gamma^{[1]i_1}_{\alpha_1} \lambda^{[1]}_{\alpha_1} \right) \left( \sum_{i_2} \lambda^{[2]}_{\beta_2} \Gamma^{[2]i_2}_{\beta_1\beta_2} \Gamma^{[2]i_2}_{\alpha_1\alpha_2} \lambda^{[2]}_{\alpha_2} \right) \\ &\times \ldots \left( \sum_{i_k} \lambda^{[k]}_{\beta_k} \Gamma^{[k]i_k}_{\beta_{k-1}\beta_k} \left[ \sum_{j_k} \langle i_k|A|j_k\rangle \Gamma^{[k]j_k}_{\alpha_{k-1}\alpha_k} \right] \lambda^{[k]}_{\alpha_k} \right) \\ &\times \ldots \left( \sum_{i_l} \lambda^{[l]}_{\beta_l} \Gamma^{[l]i_l}_{\beta_{l-1}\beta_l} \left[ \sum_{j_l} \langle i_l|B|j_l\rangle \Gamma^{[l]j_l}_{\alpha_{l-1}\alpha_l} \right] \lambda^{[l]}_{\alpha_l} \right) \ldots \left( \sum_{i_N} \Gamma^{[N]i_N}_{\beta_{N-1}} \Gamma^{[N]i_N}_{\alpha_{N-1}} \right),\end{aligned}$$

which in turn simplifies to

$$\langle\psi|O|\psi\rangle = \sum_{\beta_1\ldots\beta_N}\sum_{\alpha_1,\alpha_2,\ldots,\alpha_{N-1}} (G_1)_{\beta_1\alpha_1}\,(G_2)^{\beta_1\alpha_1}_{\beta_2\alpha_2}\ldots(G_k)^{\beta_{k-1}\alpha_{k-1}}_{\beta_k\alpha_k}\ldots \times\ldots(G_l)^{\beta_{l-1}\alpha_{l-1}}_{\beta_l\alpha_l}\ldots(G_N)^{\beta_{N-1}\alpha_{N-1}} \tag{3.33}$$

where the elements $G$ are given by

$$\begin{aligned}
(G_1)_{\beta_1\alpha_1} &= \left(\sum_{i_1}\lambda^{[1]}_{\beta_1}\Gamma^{[1]i_1}_{\beta_1}\Gamma^{[1]i_1}_{\alpha_1}\lambda^{[1]}_{\alpha_1}\right)\\
(G_2)^{\beta_1\alpha_1}_{\beta_2\alpha_2} &= \left(\sum_{i_2}\lambda^{[2]}_{\beta_2}\Gamma^{[2]i_2}_{\beta_1\beta_2}\Gamma^{[2]i_2}_{\alpha_1\alpha_2}\lambda^{[2]}_{\alpha_2}\right)\\
&\vdots\\
(G_k)^{\beta_{k-1}\alpha_{k-1}}_{\beta_k\alpha_k} &= \left(\sum_{i_k}\lambda^{[k]}_{\beta_k}\Gamma^{[k]i_k}_{\beta_{k-1}\beta_k}\left[\sum_{j_k}\langle i_k|A|j_k\rangle\Gamma^{[k]j_k}_{\alpha_{k-1}\alpha_k}\right]\lambda^{[k]}_{\alpha_k}\right)\\
&\vdots\\
(G_l)^{\beta_{l-1}\alpha_{l-1}}_{\beta_l\alpha_l} &= \left(\sum_{i_l}\lambda^{[l]}_{\beta_l}\Gamma^{[l]i_l}_{\beta_{l-1}\beta_l}\left[\sum_{j_l}\langle i_l|B|j_l\rangle\Gamma^{[l]j_l}_{\alpha_{l-1}\alpha_l}\right]\lambda^{[l]}_{\alpha_l}\right)\\
&\vdots\\
(G_N)^{\beta_{N-1}\alpha_{N-1}} &= \left(\sum_{i_N}\Gamma^{[N]i_N}_{\beta_{N-1}}\Gamma^{[N]i_N}_{\alpha_{N-1}}\right).
\end{aligned}$$

Upon exploiting the orthogonality of the Schmidt vectors, this quantity can even be simplified further.
The $\Gamma^{[n]}$ and $\lambda^{[n]}$ remain unchanged for $n < k$ and $n > l$, thus $|\psi\rangle$ can be written as some partial MPS, much the same way as for the two-site update above. This retains the (orthonormalized) Schmidt vectors $|\Phi^{[1\ldots k-1]}\rangle$ and $|\Phi^{[l+1\ldots N]}\rangle$ yielding

$$|\psi\rangle = \sum_{i_k\ldots i_l}\sum_{\alpha_{k-1}\ldots\alpha_l}\left(\lambda^{[k-1]}_{\alpha_{k-1}}\Gamma^{[k]i_k}_{\alpha_{k-1}\alpha_k}\lambda^{[k]}_{\alpha_k}\ldots\Gamma^{[l]i_l}_{\alpha_{l-1}\alpha_l}\lambda^{[l]}_{\alpha_l}\right)|\Phi^{[1\ldots k-1]}\rangle_{\alpha_{k-1}}|i_k\ldots i_l\rangle|\Phi^{[l+1\ldots N]}\rangle_{\alpha_l}.$$

The orthogonality of the Schmidt values then reduces the number of necessary operations and leads to

$$\begin{aligned}
\langle\psi|O|\psi\rangle = \sum_{i_k\ldots i_l}\sum_{\beta_{k-1}\ldots\beta_l}\sum_{\alpha_{k-1}\ldots\alpha_l}&\delta_{\alpha_l,\beta_l}\cdot\delta_{\alpha_{k-1}\beta_{k-1}}\left(\lambda^{[k-1]}_{\beta_{k-1}}\Gamma^{[k]i_k}_{\beta_{k-1}\beta_k}\lambda^{[k]}_{\beta_k}\ldots\Gamma^{[l]i_l}_{\beta_{l-1}\beta_l}\lambda^{[l]}_{\beta_l}\right)\\
&\times\left(\lambda^{[k-1]}_{\alpha_{k-1}}\left[\sum_{j_k}\langle i_k|A|j_k\rangle\Gamma^{[k]j_k}_{\alpha_{k-1}\alpha_k}\right]\lambda^{[k]}_{\alpha_k}\ldots\left[\sum_{j_l}\langle i_l|B|j_l\rangle\Gamma^{[l]j_l}_{\alpha_{l-1}\alpha_l}\right]\lambda^{[l]}_{\alpha_l}\right).
\end{aligned}$$

With the elements $G$ from above we arrive at the final form

$$\langle\psi|A_kB_l|\psi\rangle = \sum_{\beta_{k-1}\ldots\beta_l}\sum_{\alpha_k\ldots\alpha_{l-1}}\left|\lambda^{[k-1]}_{\beta_{k-1}}\right|^2(G_k)^{\beta_{k-1}\beta_{k-1}}_{\beta_k\alpha_k}\ldots(G_l)^{\beta_{l-1}\alpha_{l-1}}_{\beta_l\beta_l}. \tag{3.34}$$

### 3.3.5 Matrix product operators

Albeit we are mainly covering the TEBD algorithm in its base form, here we introduce the for our purposes most useful extension which we rely on heavily in the remainder of this work. Upon choosing a suitable basis $\mu_k$ instead of the Fock basis $i_k$ for a single site, we are able to extend the matrix product formalism and define a *matrix product operator* (MPO) which is able to describe a density matrix and thus mixed states and quantum systems at finite temperatures [51, 47].
Whereas for pure states the Fock basis was sufficient to describe the state, we now need some Hermitian matrix basis with elements $P_i$ ($i = 0, \ldots, d^2 - 1$) to describe a density matrix. For qubits this could be the Pauli matrices, for higher-dimensional sites the (generalized) Gell-Mann matrices or some manual extension of the Pauli basis can be employed. For practical reasons highlighted below it is advisable to include the unity matrix $\mathbb{1}$ as the only traceless matrix in this orthonormal set, usually belonging to index 0: $P_0 = \mathbb{1}$.
The scalar product for the basis elements $P_i$ and $P_j$ is given by

$$\langle P_i | P_j \rangle = \mathrm{tr}\left[P_i^\dagger P_j\right] \tag{3.35}$$

if the matrices $P_i$ for a site of dimension $d$ are scaled by $1/\sqrt{d}$. While this is the symmetric form, the scaling factor of both matrices could also be included in the trace operation. In either case, the expansion of the matrix $A$ in this basis is given by

$$A = \sum_i \langle P_i | A \rangle P_i. \tag{3.36}$$

Because the relation $\mathrm{tr}\,[A \otimes B] = \mathrm{tr}\,[A] \otimes \mathrm{tr}\,[B]$ holds, the density matrix can be written as

$$\rho = \sum_i \langle \rho | P_i \rangle P_i = \sum_{j_1 \ldots j_N} \langle \rho | P_{j_1} \otimes \ldots \otimes P_{j_N} \rangle \; P_{j_1} \otimes \ldots \otimes P_{j_N}. \tag{3.37}$$

This conserves its trace property; since $\mathrm{tr}\,[P_{j_1} \otimes \ldots \otimes P_{j_N}] = \delta_{j_1,0} \cdot \delta_{j_N,0}$, only the trace of exactly one basis element is zero, yielding

$$\mathrm{tr}\,[\rho] = \sum_{j_1 \ldots j_N} \langle \rho | P_{j_1} \otimes \ldots \otimes P_{j_N} \rangle \; \mathrm{tr}\,[P_{j_1} \otimes \ldots \otimes P_{j_N}] \tag{3.38}$$

$$= \tilde{c} \langle \rho | P_0 \otimes \ldots \otimes P_0 \rangle = \langle \rho | \mathbb{1} \otimes \ldots \otimes \mathbb{1} \rangle = \mathrm{tr}\,[\rho] = 1 \tag{3.39}$$

with the constant $\tilde{c} = \sqrt{\Pi_{k=1}^N j_k}$. Thus the normalization condition for the MPO is to set the coefficient $c_{0\ldots0} = 1$. This coefficient can easily be obtained by contracting the MPO; thus a normalization can be performed by simply dividing the complete MPO by the obtained coefficient.

The MPO formalism requires a slight change in the way the two-site update is obtained. Now a local gate does not consist of one exponentiated Hamiltonian that is applied, but of two. The MPO however requires some matrix-vector like action where some operator acts on the basis state, so that the insertion of an identity can yield the update rule (as seen for pure states before). Therefore we resort to the super-operator formalism,

denoting super-operators that act on operators by the subscript #. We obtain the required super-operator by rewriting

$$\rho_i(t+\delta t) = \mathrm{tr}\left[P_i e^{-\frac{i}{\hbar}H\delta t}\rho(t)\, e^{\frac{i}{\hbar}H\delta t}\right] \tag{3.40}$$

$$= \mathrm{tr}\left[P_i e^{-\frac{i}{\hbar}H\delta t}\left(\sum_j \rho_j(t) P_j\right) e^{\frac{i}{\hbar}H\delta t}\right] \tag{3.41}$$

$$= \sum_j \rho_j(t)\,\mathrm{tr}\left[P_i e^{-\frac{i}{\hbar}H\delta t} P_j e^{\frac{i}{\hbar}H\delta t}\right] \tag{3.42}$$

$$\stackrel{!}{=} \sum_j (A_\#)_{i,j}\,\rho_j(t) \tag{3.43}$$

where the last line denotes the structure of a matrix-vector multiplication we want to achieve for the super-operator $A_\#$. Now by comparison we can identify the elements of $A$ as

$$(A_\#)_{i,j} = \mathrm{tr}\left[P_i e^{-\frac{i}{\hbar}H\delta t} P_j e^{\frac{i}{\hbar}H\delta t}\right]. \tag{3.44}$$

Thus we obtained an update rule similar to this of Eq. (3.22) in the case of pure states. The general update routine of the numerical implementation does not require any changes and simply is passed the different update matrix.

This procedure of how to define some super-operator action on a mixed state easily generalizes to various other cases, like imaginary time evolution to build a thermal state (see next section) or the application of Lindblad-type operators.
As the third and last ingredient we need a way to perform measurements. This is pretty straight-forward in this new formalism and oftentimes even cheaper than for pure states. Since the expectation value of an operator $O$ is given by $\langle O\rangle = \mathrm{tr}[O\rho]$, it is simply the combination of first applying the gate $O$ on the state $\rho$ and subsequently measuring $\mathrm{tr}[\rho]$ of this new state.

#### 3.3.5.1 Thermal states

A common class of useful initial states are thermal states. In the TEDOPA scheme often an environment is prepared in a thermal state, to couple it to some system at time $t = 0$. The thermal state $\rho(\beta)$ for some inverse temperature $\beta = 1/k_B T$ is given by

$$\rho(\beta) = \frac{e^{-\beta H}}{Z(\beta)} = \frac{1}{Z(\beta)}\sum_s e^{-\beta E_s}|E_s\rangle\langle E_s| \tag{3.45}$$

with the partition function $Z(\beta) = \mathrm{tr}[\exp(-\beta H)]$. Since it usually is neither feasible nor sensible to calculate all eigenstates $|E_s\rangle$ and average them to achieve the thermal state, another procedure is necessary.
By means of an imaginary time evolution we can build the thermal state for any given inverse temperature $\beta$ by starting from infinite temperature $T \to \infty$ and gradually lowering it until the desired temperature is reached. The thermal state at infinite temperature is given by the (normalized) unity matrix, which then can be imaginary time evolved by

$N$-fold successive symmetric applications of the operator $\exp(-\delta t H)$ with the property $N \cdot \delta t = \beta$. The $n$'th application is given by

$$\rho_n = e^{-\frac{\delta t}{2}H} \rho_{n-1} e^{-\frac{\delta t}{2}H} \tag{3.46}$$

where the iteration starts from $\rho_0 = \mathbb{1}$. A super-operator for this iteration is then obtained the same way as above for an ordinary time evolution [51].

### 3.3.6 Time evolution

To apply a time evolution to a pure quantum state, usually it is necessary to build the quantity $\exp\left(-\frac{i}{\hbar} H \delta t\right)$ for the complete Hamiltonian $H$ and the time step $\delta t$. Especially for quantum many-body systems this is in general impossible due to the Hamiltonian's dimensions. However, by exploiting its structure one often can find a way to come up with a sufficiently good approximation. The same challenge appears for other tasks, like imaginary time evolution to obtain a ground state, for building thermal states or for negative-time evolutions. Thus such approximations are heavily employed. The most famous one is the Suzuki-Trotter expansion which is possible if the Hamiltonian exhibits a nearest-neighbor interaction (as does the Hamiltonian introduced in Section 3.4).
For two (in general non-commuting) matrices $A$ and $B$, the Zassenhaus formula [62] gives the exponential of their sum as

$$e^{A+B} = e^A \; e^B \; e^{\frac{1}{2}[A,B]} \; e^{\frac{1}{3}[[B,A],A]} \; e^{\frac{1}{6}[[B,A],B]} \cdot \ldots \tag{3.47}$$

For a Hamiltonian $H$ with nearest-neighbor interaction

$$H = \sum_{i=1}^{N-1} H_{i,i+1} \tag{3.48}$$

of a $N$-particle quantum many-body system we have the convenient property that all even terms $H_{i,i+1}$ commute with each other, as well as all odd terms commute amongst themselves. This immediately suggest the splitting

$$F = \sum_{i=1}^{\lfloor N/2 \rfloor - 1} H_{2i,2i+1} \tag{3.49}$$

$$G = \sum_{i=1}^{\lfloor N/2 \rfloor} H_{2i-1,2i} \tag{3.50}$$

where $F$ contains all even terms and $G$ all odd terms. The successive application of the Zassenhaus formula shows that $\exp(\alpha F)$ ($\alpha \in \mathbb{C}$) is easily accessible, as well as $\exp(\alpha G)$. Thus to obtain the exponentiation of the complete Hamiltonian, the easiest possible solution is given by

$$e^{(F+G)\delta t} = e^{F\delta t} \; e^{G\delta t} + \mathcal{O}\left(\delta t^2\right). \tag{3.51}$$

This leads to a deviation of the order of $\delta t^2$. However, it should be noted that due to the discarded nested commutator relations from the Zassenhaus formula, this error in general has a non-trivial dependence on the operator norm of $F$ and $G$ as well.

A plethora of possible expansions ensues. The first non-trivial and widely used version is the third-order (referring to the error term) Suzuki-Trotter expansion $s(F, G, \delta t)$ given by [63]

$$e^{H\delta t} = e^{(F+G)\delta t} = s\left(F, G, \delta t\right) = e^{\frac{1}{2}F\delta t}\ e^{G\delta t}\ e^{\frac{1}{2}F\delta t} + \mathcal{O}\left(\delta t^3\right). \tag{3.52}$$

This formula propagates the system for one time step $\delta t$. One application of the exponential containing $F$ or $G$ is termed one *sweep*. Note that, if no measurement or application of some gate operation is required between two consecutive time steps, then the last sweep of a time step can be joined with the fist sweep of the next time step, reducing the numerical effort by one third.
While this formula provides an amazing trade-off between accuracy and computational effort, sometimes a more exact scheme is desirable. Especially for applications where smaller, lower-dimensional systems are investigated with high accuracy. While many of such high-accuracy higher-order schemes exist, and are often developed for or tailored to very special applications, one of the general-purpose schemes is the fifth order expansion that results from applying five successive second-order type terms yielding [63]

$$e^{H\delta t} = e^{(F+G)\delta t} = \prod_{i=1}^{5} s\left(F, G, q_i\delta t\right) + \mathcal{O}\left(\delta t^5\right). \tag{3.53}$$

The coefficients are given by $q_i = q = (4 - 4^{1/3})^{-1}$ for $i = 1, 2, 4, 5$ and $q_3 = 1 - 4q < 0$, resulting in four forward propagations of step size $q\delta t$ as well as one propagation backwards in time of step size $q_3\delta t$ [63].

It should be noted that especially in algorithms like the TEBD, where the application of one time step is quite costly (or even incurs an additional error), lower-order schemes with smaller time steps are often preferable to higher-order schemes due to the smaller number of necessary sweeps.
A different propagation possibility is given by iterative methods for differential equations. Some algorithms developed in the DMRG context for example employ Runge-Kutta iterations, built by applying the (non-exponentiated) Hamiltonian, scaled by the time step, thus determining the state at other times [64]. Starting from there, further methods developed, i.e. based on the Lanczos method [65], or even applying these Runge-Kutta schemes to MPS [66].

### 3.3.7 Error analysis

Now that all ingredients are introduced to allow a simulation by means of MPS or MPO, we are in a place to ask the question how good such an approximation is. The errors introduced into the quantum state are due to several effects. The first error is due to the MPS/MPO approximation, introduced by the cutoff in the matrix sizes, whereas a second error is introduced by the Trotter decomposition in the time evolution. While further minor error sources exist, these are the major, unavoidable ones. Thus we focus on them in the present analysis.

The Trotter error $\varepsilon_{\text{trotter}}$ comes about due to the Trotterization of the time evolution explained in Section 3.3.6. The various sweeps created by this Trotterization all scale

with the size of the time step. Thus the error $\varepsilon$ that a decomposition of order $p$ introduces is of order $\mathcal{O}\left((\delta t)^{p+1}\right)$. This order-notation can be misleading at times – it should be noted that in spite of the absence of the system's size the total Trotter error in general scales roughly linear with the system size $N$. This is due to the nested commutators occurring in the error term of the Suzuki-Trotter decomposition, as can be seen when applying the Baker-Campbell-Hausdorff formula [67].
Since the number of time steps taken is the total time $T$ divided by the number of time steps $T/\delta t$, the total Trotter error is

$$\varepsilon_{\text{trotter}} \propto \mathcal{O}\left((\delta t)^p NT\right). \tag{3.54}$$

The Trotterization also may lead to a loss of orthogonalization due to the non-consecutive application of gates. This can be circumvented by resorting to schemes that employ consecutive gate applications [68].

However, in most cases the Trotter error is the lesser problem. The more relevant error source is the truncation error. It stems from the truncation of the singular values during the application of a two-site gate. For pure states this can easily be seen due to the direct relation to the Schmidt decomposition, which splits a state as

$$|\psi\rangle = \sum_{i=1}^{\chi'} \lambda_i |\psi_i^{\text{left}}\rangle |\psi_i^{\text{right}}\rangle + \sum_{i=\chi'+1}^{\chi} \lambda_i |\psi_i^{\text{left}}\rangle |\psi_i^{\text{right}}\rangle \tag{3.55}$$

$$= |\psi_{\text{trunc}}\rangle + |\psi_\perp\rangle \tag{3.56}$$

where the left sum until $\chi'$ denotes the kept part $|\psi_{\text{trunc}}\rangle$ and the right sum starting from $\chi'+1$ denotes the discarded part $|\psi_\perp\rangle$. Due to the fact that the $|\psi_i^{\text{left}}\rangle$ are mutually orthogonal (as are those of the right subsystem), the discarded part is orthogonal to the retained part. Given that the squared Schmidt values sum up to one, this truncation leads to a deviation in the norm of the state

$$\langle\psi_{\text{trunc}}|\psi_{\text{trunc}}\rangle = 1 - \sum_{i=\chi'+1}^{\chi} \lambda_i^2 = 1 - w \tag{3.57}$$

where we defined the *discarded weight*

$$w = \sum_{i=\chi'}^{\chi} \lambda_i^2. \tag{3.58}$$

Thus when renormalizing the $|\psi_{\text{trunc}}\rangle$ we pick up a factor of $1/(1-w)$. Thus upon $n$ truncations we are off by a factor of about $(1-w)^{n_t}$ with $n_t$ being the number of truncations performed. Truncating each bond in each time step results in $n_t \propto \frac{NT}{\delta t}$ and thus the truncation error is about

$$\varepsilon_{\text{trunc}} = (1-w)^{\frac{NT}{\delta t}} = \exp\left(\frac{NT}{\delta t}\ln(1-w)\right) \tag{3.59}$$

Thus we end up with the need of a careful balancing of the two errors, depending on the size of the time step $\delta t$. For smaller $\delta t$ we have a smaller truncation error. Yet this requires more truncations due to the larger number of time steps taken and thus in a larger truncation error. Also Eq. (3.59) shows that the error grows exponential with the number of truncations performed which determines some kind of *runaway time* after which the error starkly rises and renders further time evolution impossible [67].

## 3.4 TEDOPA

The Time Evolving Density Matrix with Orthogonal Polynomial Algorithm (TEDOPA) [5, 6, 69, 70] is a numerically exact and certifiable simulation method for open quantum system dynamics [71]. It applies to general systems under arbitrarily strong linear interaction with an environment that is modeled by a set of independent harmonic oscillators. This underlying spin-boson model (cf. Section 2.5) with an arbitrary spectral density is treated exactly by mapping it onto a semi-infinite, one-dimensional configuration subject to a nearest-neighbor Hamiltonian. In this new configuration the system couples only to the chain's first site. This allows for the deployment of algorithms able to treat such one-dimensional configurations – like the TEBD encountered in Section 3.3 or time-dependent density matrix renormalization group (t-DMRG) methods [72].
Thus TEDOPA can be summarized as a two-stage sequence to enable full treatment of the system and environment degrees of freedom. The first step employs the *chain mapping* presented in Section 3.4.1 below, an ingenious transformation based on orthogonal polynomials to convert the star-shaped system-environment structure into a one-dimensional configuration. For arbitrarily shaped spectral densities (especially those structured by sharp modes) a numerically stable approach has been developed [5, 44] to perform this mapping. Some details for the second step – the numerical treatment of the emerging configuration – are given in Section 3.4.2 below.

A large number of applications becomes accessible by TEDOPA. First and foremost are settings that feature richly structured environments, such as photosynthetic complexes. We will thoroughly investigate these in Chapters 5 and 6. Note however that the TEDOPA approach is completely general. Any system that is coupled linearly to bosonic or even fermionic environments with arbitrary spectral densities can be treated, as shown for photosynthetic crystals in [73].
Another important fact is that TEDOPA provides complete information about the environment, at every step of the time evolution. This directly offers the possibility to study system-environment correlations and thus allows access to effects based on these correlations, like long-lasting coherences or entanglement. We exploit this fact in our investigation of PPCs in Chapter 5, observing the time evolution of environmental properties that relate to the microscopic mechanism we are looking to identify.

### 3.4.1 The chain mapping

We now return to the spin-boson model which we introduced in Section 2.5 to model the environment of an open quantum system. To facilitate the numerical treatment of this model we aim at recasting it in a one-dimensional form; the procedure to do so is thus termed *chain mapping*. The present account is based on [5, 6], for further extensions, proofs, and subtleties see also [70, 71].

The spectral density

$$J(\omega) = \pi h^2 \left[g^{-1}(\omega)\right] \frac{dg^{-1}(\omega)}{d\omega} \tag{3.60}$$

encapsulates the information of the environment in this model. It does not, however, uniquely define the dispersion relation $g(x)$ and coupling function $h(x)$. The chain

mapping employs the particular choice $g(x) = g \cdot x$, resulting in an especially simple transformation of the bosonic modes.

The set of oscillators $a_x$, $a_x^\dagger$ describing the environment in the spin-boson model is replaced by a new set of oscillators $b_n$, $b_n^\dagger$ which fulfill the bosonic commutation $\left[b_n, b_m^\dagger\right] = \delta_{nm}$ relations as well.
This can be thought of as a change of basis. Whereas in the original picture we had separated oscillators for every frequency, now we group them in a specific way. The mapping is constructed in such a way that a discrete chain of harmonic oscillators emerges. This extends an idea dating back to the numerical renormalization group (NRG) and its logarithmic discretization [74].

To design the transformation $U_n(x)$ accordingly, we make use of the theory of orthogonal polynomials (as introduced in Section 3.2). Therefore we define a family $\tilde{p}_n(x)$ of (normalized monic) orthogonal polynomials

$$\tilde{p}_n(x) = \frac{\pi_n(x)}{\|\pi_n(x)\|} \tag{3.61}$$

with respect to the measure $d\mu(x) = h^2(x)dx$. This measure is, according to Eq. (3.60) and the convention $g(x) = gx$, only the rescaled spectral density multiplied by a constant. $J(\omega)$ is positive by definition, thus $h(x)$ is real, and so $d\mu(x)$ is indeed a valid measure. Now the rule after which the new oscillators $b$ are built is

$$b_n^\dagger = \int_0^{x_{\max}} dx\ U_n(x)\, a_x^\dagger \tag{3.62}$$

with the unitary transformation

$$U_n(x) = h(x)\, \tilde{p}_n(x)\,. \tag{3.63}$$

The inverse transformation is given by

$$a_x^\dagger = \sum_n U_n(x)\, b_n^\dagger. \tag{3.64}$$

Employing this transformation, the full spin-boson Hamiltonian $H$ is thus transformed from its original form

$$H = H_{\text{sys}} + \int_0^{x_{\max}} dx\ g(x)\, a_x^\dagger a_x + \int_0^{x_{\max}} dx\ h(x)\, A_{\text{sys}} \left(a_x + a_x^\dagger\right) \tag{3.65}$$

to the new form $\tilde{H}$

$$\tilde{H} = H_{\text{sys}} + \eta_0 A_{\text{sys}} \left(b_0 + b_0^\dagger\right) + \sum_{n=0}^{\infty} \omega_n b_n^\dagger b_n + \sum_{n=0}^{\infty} \eta_n \left(b_n^\dagger b_{n+1} + b_n b_{n+1}^\dagger\right), \tag{3.66}$$

which represents a one-dimensional, semi-infinite configuration. The new environment with oscillators described by $b_n$ and $b_n^\dagger$ depends on the new parameters $\omega_n$ and $\eta_n$, identified as on-site energies and couplings of a chain. The multiple couplings between the system and the environmental sites have been replaced by a single coupling between the

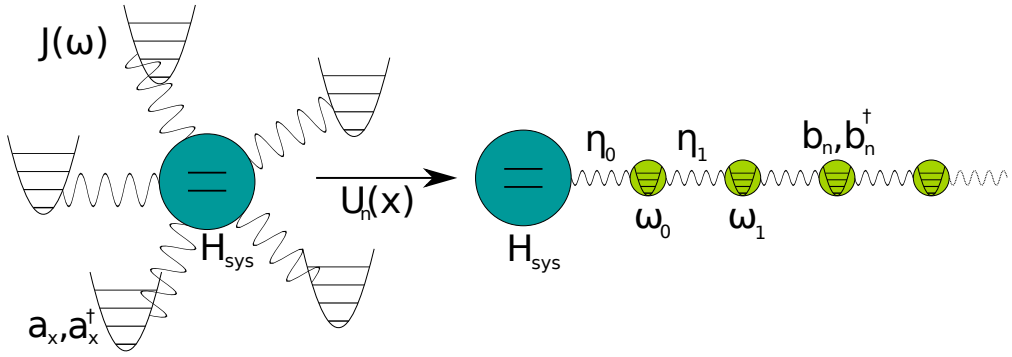


Figure 3.3: Illustration of the chain mapping. The spin-boson model on the left (with spectral density $J(\omega)$) is transformed into the one-dimensional configuration on the right (with coefficients $\omega_n$ and $\eta_n$ determined by the chain mapping). The transformation is performed by the unitary transformation $U_n(x)$ for the oscillators with operators $a_x$ and $a_x^\dagger$, resulting in the new oscillators $b_n$ and $b_n^\dagger$.

system and the chain's first site (with coupling $\eta_0$), as can be seen in Fig. 3.3. Note also that the resulting Hamiltonian exhibits only nearest-neighbor interactions, making its interactions local and thus avoiding long-ranging interactions that are often difficult to treat numerically.

To see how this change of geometry happens, we look more closely at the transformation of the interaction part of the Hamiltonian (3.65) – performed by applying Eq. (3.64) – which yields

$$H_{\text{int}} = A_{\text{sys}} \int_0^{x_{\max}} dx\ h(x) \left(a_x + a_x^\dagger\right) \tag{3.67}$$

$$= A_{\text{sys}} \sum_n \int_0^{x_{\max}} dx\ h(x)\, U_n(x) \left(b_n + b_n^\dagger\right) \tag{3.68}$$

$$= A_{\text{sys}} \sum_n \int_0^{x_{\max}} dx\ h^2(x)\, \frac{\pi_n(x)}{\|\pi_n\|} \left(b_n + b_n^\dagger\right). \tag{3.69}$$

However, for monic polynomials we have $\pi_0 = 1$ which we now introduce and which, together with $\pi_n(x)$, creates a Kronecker delta $\delta_{n,0}$ that cancels all terms from the sum except the one for $n = 0$, leaving us with

$$H_{\text{int}} = A_{\text{sys}} \sum_n \int_0^{x_{\max}} dx h^2(x)\, \frac{\pi_n(x)\,\pi_0(x)}{\|\pi_n\|} \left(b_n + b_n^\dagger\right) \tag{3.70}$$

$$= A_{\text{sys}} \sum_n \frac{\|\pi_n\|^2 \delta_{n,0}}{\|\pi_n\|} \left(b_n + b_n^\dagger\right) \tag{3.71}$$

$$= A_{\text{sys}} \|\pi_0\| \left(b_0 + b_0^\dagger\right) \tag{3.72}$$

$$= \tilde{H}_{\text{int}}. \tag{3.73}$$

This not only shows the change in geometry induced by the orthogonality of the polynomials, but also identifies the constant $\eta_0$ from Eq. (3.66) as $\eta_0 = \|\pi_0\|$. The environmental

Hamiltonian is transformed in a similar manner; by inserting the transformation for $a_x$ and $a_x^\dagger$ one obtains

$$H_{\mathrm{env}} = \int_0^{x_{\max}} dx\ g(x)\, a_x^\dagger a_x \tag{3.74}$$

$$= \sum_{m,n} \int_0^{x_{\max}} dx\ U_n(x)\, U_m(x)\, g(x)\, b_x^\dagger b_x \tag{3.75}$$

$$= g \sum_{m,n} \int_0^{x_{\max}} dx\ h^2(x) \left[x\tilde{p}_n(x)\right] \tilde{p}_m(x)\, b_x^\dagger b_x \tag{3.76}$$

where the linear dispersion relation $g(x) = g \cdot x$ was employed. Until now all modes still couple to each other. But now we make use of the recurrence relation Eq. (3.12) for orthogonal polynomials to substitute the term $x\tilde{p}_n(x)$ which leaves us with

$$\tilde{H}_{\mathrm{env}} = g \sum_{m,n} \int_0^{x_{\max}} dx\ h^2(x) \left[\frac{1}{C_n}\tilde{p}_{n+1}(x) + \frac{A_n}{C_n}\tilde{p}_n(x) + \frac{B_n}{C_n}\tilde{p}_{n-1}(x)\right] \tilde{p}_m(x)\, b_x^\dagger b_x \tag{3.77}$$

$$= g \sum_n \frac{1}{C_n} b_n^\dagger b_{n+1} + \frac{A_n}{C_n} b_n^\dagger b_n + \frac{B_{n+1}}{C_{n+1}} b_n b_{n+1}^\dagger \tag{3.78}$$

$$= g \sum_n \omega_n b_n^\dagger b_n + \sum_n \eta_n \left(b_n^\dagger b_{n+1} + b_n b_{n+1}^\dagger\right) \tag{3.79}$$

where the second equality is due to orthogonality of the polynomials and the final form introduces the constants $\omega_n$ and $\eta_n$ depending on the constants $\alpha_k$ and $\beta_k$ of the recurrence relations of the monic polynomials

$$\omega_n = g\alpha_n \tag{3.80}$$

$$\eta_n = g\sqrt{\beta_{n+1}}. \tag{3.81}$$

The relation between the $A_k$, $B_k$, $C_k$ and the $\alpha_k$, $\beta_k$ is given by Eq. (3.15). The existence of a stable numerical algorithm and publicly available implementation to obtain the coefficients $\alpha_n$ and $\beta_n$ makes this procedure not only feasible but also easy to use. We again refer to the ORTHOPOL package from [44] whose *mcdis*-routine returns, given a suitable measure, the $\alpha_k$ and $\beta_k$ coefficients.

### 3.4.2 Numerical treatment

The subsequent numerical treatment of the one-dimensional configuration is in principle open to the method of choice. We employ the TEBD algorithm from Section 3.3, which perfectly fulfills our needs. Due to the nearest-neighbor interaction of the resulting Hamiltonian it is perfectly applicable.

To suit numerical needs, in the next step it is necessary to further adjust the configuration resulting from the chain mapping. The number of levels for the environment's oscillator on site $k$ can be restricted to $d_{k,\max}$ to reduce required computational resources. A suitable value for $d_{k,\max}$ is related to this site's average occupation, depending on the environment's structure and temperature. The number of sites that is required to faithfully represent the environment has to be sufficiently large to completely give the

appearance of a "large" reservoir – one that avoids unphysical back-action on the system due to finite-size effects that lead to reflections at the system boundaries (cf. Chapter 7 for an extensions of TEDOPA that can alleviate this problem considerably). Those are native TEDOPA error sources and they have a direct effect on the maximum temperature that may be simulated and the recurrence time of the simulation, respectively. It should be noted that these truncations, while feasible numerically and easily justifiable in a hand-waving kind of argument, in the end can also be *rigorously certified* by analytical bounds [71]. These adjustments yield an emerging system-environment configuration which is now conveniently accessible by TEBD. The final one-dimensional configuration consisting of a systems plus its environment is then treated by TEBD, exploiting its full simulation power for one-dimensional systems. TEBD itself introduces some numerical error too. The error's nature and how to choose parameters according to minimize it is well-known however (see also Section 3.3.7).

Typical simulations start out with the environment in a ground or thermal state $\rho_{\text{env}}$ (both obtainable by imaginary time evolution) and the system in some separately prepared initial state of choice. At time $t = 0$ the environment is coupled to the system, followed by the full time evolution of system plus environment, allowing the observation of the system by measuring expectation values (due to the fact that the system has not been transformed). Even some properties of the environment are accessible this way, a fact that is exploited in Chapter 5. The time dependence of arbitrary observables $O$ of the system or the environment are obtained from $\langle O \rangle(t) = \operatorname{tr}[\rho(t)O]$, where $\rho(t)$ is the total state of the system and the bath. Clever reordering of terms also makes the calculation of various experimentally accessible spectra possible. In Section 7.6.3 we present this for a dimer's absorption spectrum.

For an assessment and comparison to other numerical methods, i.e. those presented in Section 2.6, we conclude this introduction by highlighting TEDOPA's main advantages. Three aspects distinguish it from other open quantum-system methods. First, it does not restrict the ratio $\lambda$ between inner-system couplings and system-environment couplings, unlike other methods which assume either $\lambda \gg 1$ or $\lambda \ll 1$. Second, the spectral density characterizing the system-environment interaction may assume any arbitrary shape, including a wide variety of sharp features as they occur in biological settings. And third, while applicable to all temperatures, due to its scaling properties TEDOPA is inherently well-suited for simulations in the low-temperature domain.

# CHAPTER 4

## Quantum Biology

Nowadays, the amazing achievements of experimental quantum physics are found aplenty in ion traps, optical lattices, Bose-Einstein condensates and similar applications. All of these produce remarkable results, verifying the laws of quantum mechanics over and over again. And they all make use of the unique quantum resources, entanglement and coherence. At extremely low temperatures and under almost utter isolation from external influences, these resources can easily be used to exploit quantum properties to build modern quantum machines, maybe a full quantum computer one day.
However, in recent years the question is arising again whether these effects can indeed be found not only under such extremely isolated conditions, but in our daily life. Or more specifically, in naturally evolved biological structures. Since evolution did an awesome job on many of the existing species, is it conceivable that it actually did exploit quantum mechanics at some point? Already Jordan and Schrödinger pondered whether it is possible that quantum effects play a role in complex biological structures [75, 76].
Intuition denies that readily. Compared to the modern experimental set-ups, these "noisy, warm and wet" conditions that biology provides cannot conceivably host quantum effects. However, for the smallest of systems, i.e. atoms, we know for sure that quantum mechanics does play a role. When we enlarge these systems, we often still can measure quantum effects – superposition patterns of fullerene molecules being a prominent example [77]. But for comparatively huge systems, like cells, we know quantum effects to be absent for sure. So where do we cross this boundary? And is it a sharp boundary or more like a transition zone? These are questions that the arising field of quantum biology deals with.
The field of quantum biology mostly evolves around three astonishing effects in biology for which it is highly likely that the underlying biological structure exploits the quantum nature of its constituents. These are bird navigation, olfaction (the sense of smell), and excitation energy transport in photosynthetic pigment protein complexes. The current prominence of the field mainly dates back to 2007, when Engel *et al.* [7] published the results of their seminal experiments on photosynthetic protein complexes of marine algae, employing an intricate spectroscopic set-up that revealed quantum beatings in the exciton dynamics. This gave rise to researchers flocking into the field and subsequently

even resulted in the launching of the conference series "Quantum Effects in Biological Systems" (QuEBS), until very recently it culminated in the first comprehensive book presenting an introduction to quantum biology [78].
The focus of the present work is mainly on the quantum effects in photosynthetic complexes. Yet for the sake of completeness we will superficially introduce the remaining two areas of quantum biology as well – for a more complete account refer to the provided references. Thereafter we continue towards the photosynthetic complexes and lay the ground work for the results presented in Chapters 5 and 6. All covered topics, as well as the underlying deeper connections between them, can extensively be reviewed in [79, 78].

## 4.1 Bird navigation

It is well-known that animals such as birds, reptiles and insects are able to sense the earth's magnetic field and use it to their advantage; bird migration being a well-known example [80].
This navigational sense of birds exhibits three properties that have been determined experimentally. First, it is restricted to work only at field strengths that are in a very narrow window around the earth's magnetic field strength. Second, it is sensitive to the field's inclination and is not based on the magnetic field's polarity. And third, it needs the presence of light at wavelengths between UV and green [81].
Solidly founded explanations for such detection-mechanisms are rare. Amongst them only two remained over the last years. One is basically classical and proposes clusters of ferrimagnetic iron oxide particles in the upper beak of birds. Forces acting upon these particles make them act as a magnetometer, allowing the determination of the geographical position. The competing theory is the *radical pair mechanism* which is able to explain these observed properties. It proposes spin-chemical processes that can occur in the chryptochrome present in the retina of migratory birds. This theory is corroborated by experiments employing radio frequency fields on birds such as the European robin [82], used as diagnostic tool for radical pair processes [78, 79].
The idea of this *chemical compass* is based on a donor-acceptor pair where the donor is equipped with an electron pair in the singlet state. Upon optical excitation (i.e. by ambient light) an electron transfer is induced, passing one of the electrons to the acceptor. This creates a radical pair – two molecules, each of them with an unpaired electron. Magnetoreception becomes possible then due to the (quantum) interaction between the electron spin and its nuclear spin environment. This highly non-trivial process can be understood from a quantum metrology perspective in analogy to a quantum interferometer that exploits global quantum coherence [83].

## 4.2 Sense of smell

In analogy to bird navigation, the explanation for olfaction – the sense of smell – still is not fully understood yet. And as before, there are two predominant concepts which we briefly sketch here; for a more detailed introduction and further references refer to [84, 79].
Until about two decades ago, the lock-and-key description, dating back to 1963, was generally accepted as explanation of this process [85]. The spatial shape of an odorant

was assumed to be the "key" that fits the "lock" provided by the receptor, leading to a signal response creating the sensation of smell.
While this explanatory mechanism is indeed often useful, for example in enzyme recognition processes, there is experimental evidence that it does not work in olfaction. For instance, oftentimes two molecules that could fit the same receptor exhibit quite different smells. Several experiments, i.e. with rodent olfactory receptor neurons [86], have shown that odorants with distinct shapes can easily elicit reactions from the same olfactory cells.
A different explanation for olfaction was developed in parallel [87, 88]. Such proposals suggest the scent of a molecule to be determined by its vibrational spectrum, in much the same way as the wavelength of light is determined by its color. A neat illustration of the importance of the vibrational spectrum are experiments showing that Drosophila flies indeed are able to discriminate between odorants in their hydrogenated and their deuterated form [89]. Since these forms exhibit virtually the same shape but a disparate vibrational spectrum, this is evidence in favour of a vibrational explanation for olfaction instead of a lock-and-key mechanism depending on the molecules spatial structure.
While this does suggest vibrations to play a role in the olfactory process, a *purely* vibrational theory has its own shortcomings thus can be excluded [84]. However, it served as starting point for the biophysicist Luca Turin to extend this theory employing quantum mechanics [90]. The key idea is that the receptor contains as well an electron donor as an electron acceptor, separated in energy by $\delta E$. This $\delta E$ is exactly the energy of a vibrational quantum of the odorant that is able to "dock" to this receptor. The docking launches an electron tunneling event where the (vibrational) phonon bridges the energy difference.
The beauty of this theory lies in its simplicity and the fact that it actually manages to explain as well the experimental results that refute the lock-and-key theory as well as those that contradict the purely vibrational model [91]. Thus the presence of quantum (tunneling) effects in the model of olfaction might easily be a physical fact.

## 4.3 Photosynthetic complexes

We now turn towards the most active area of research in the field of quantum biology, namely the evidence of quantum effects in photosynthetic complexes. To set the stage we briefly introduce the photosynthetic process in general, followed by looking more closely at the types of organism relying on photosynthesis. This summary is largely based on the discussions in [92], which offer a much more detailed summary than possible in the scope of this work. Focusing on pigment-protein structures that play a key role during this process, we introduce experimental set-ups that are able to investigate these complexes and why their outcome hints at the presence of quantum effects. We conclude by focusing on prevalent theoretical models of these complexes that manage to incorporate the underlying biological structure into a simplified description, treatable numerically, thus leading towards new insights and offering explanations of experimentally observed effects.

### 4.3.1 Photosynthesis

All living organisms are built up of cells or syncytia (which basically are fused cell complexes). Interestingly, in all different cells of all living organisms, every process conducted by cells can be traced back to *adenosine triphosphate* (ATP) as power source. These are entirely disparate processes like chemical, osmotic, or mechanical work, eventually all powered by enzymes-catalyzed hydrolysis of ATP into adenosine diphosphate (ADP) or adenosine monophosphate (AMT).
The way this ATP is restored from the chemical end products ADP or AMT varies widely across the range of cells. One such mechanism is the photosynthetic process, which in itself again varies widely over the different types of phototropic organisms (i.e. organisms that use light as energy source). However it always starts with the absorption of light in chlorophyll and results in the oxidation of some electron donor which then is used in some manner to produce ATP. A very general way to write the photosynthetic reaction is

$$CO_2 + 2\ H_2A \rightarrow (CH_2O) + 2\ A + H_2O \tag{4.1}$$

where $H_2A$ is some electron donor that becomes oxidized.

Plants are readily thought of when talking about photosynthesis. But they are by far not the only phototropic organisms; plenty of algae for example do so too. These are all of the eukaryotes that perform photosynthesis. In addition several prokaryotes are phototropic, namely the following five groups of bacteria:

- purple bacteria
- green sulphur bacteria
- green nonsulfur bacteria
- heliobacteria
- cyanobacteria.

The first four are anoxygenic, meaning no oxygen is produced during their photosynthetic process. Of all photosynthetic organisms, the green sulfur bacteria are those that can survive at the lowest light intensities. They can even be found more than 2 km deep in the ocean, fueled by thermal radiation from hot springs at the bottom of the sea [93]. This is only possible due to their complex and highly specialized *chlorosomes* which are antenna structures allowing for an amazingly effective absorption of radiation.
Due to these extreme low-light conditions, efficiency in the light absorption and excitation transport processes is much more significant than in environments with an abundance of light. This is the reason why they constitute such a suitable starting point to check for quantum effects; highly optimized and effective systems grown by nature are amongst those which we would first suspect to exploit all possible advantages – even of quantum nature.
One genus of green sulphur bacteria is Chlorobium. Amongst the species belonging to this genus, Chlorobium tepidum became the model organism of this group (albeit a number of experiments is also performed on further members of this group, i.e. on

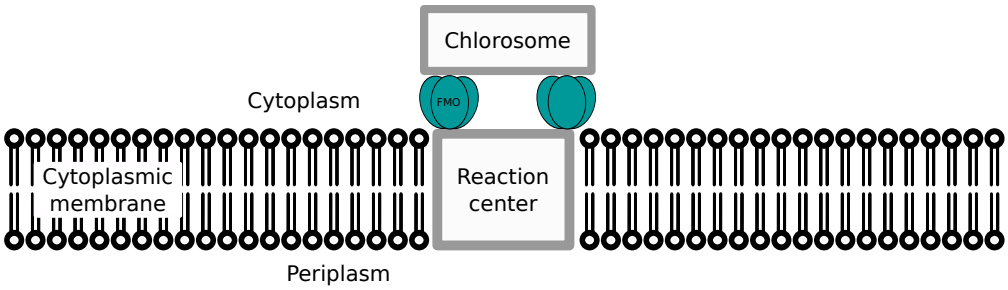


Figure 4.1: Position and composition of the organelles in green sulfur bacteria that are important for the photosynthetic process (analogous to [95])

Prosthecochloris aestuarii). It thrives at around 50 °C and has first been extracted from acidic hot springs in New Zealand [94].

Due to the vast differences between eukaryotic and prokaryotic cells, the photosynthetic process, structures, and components can be found in plenty of variations. Exemplary we focus on the gram-negative Chlorobium tepidum here; the mainly involved components are sketched in Fig. 4.1. The inside of the bacterial cell is filled with cytoplasm, enclosed by the cytoplasmic (or inner) membrane. Outside of this membrane the outer membrane can be found, separating the cell from the outer world. The space between these two membranes is filled by the periplasm. This two-membrane structure is crucial for plenty of trans-membrane chemical-biological processes that employ some separating process to build a concentration gradient.
To shed light onto the importance and function of these structural parts, lets have a closer look at the photosynthetic process. It consists of four stages:

1. light absorption
2. primary electron transfer in the reaction center
3. energy stabilization by secondary processes
4. synthesis and the export of stable products.

The actual photochemistry cannot be carried out by every pigment in the cell. It is quite economic for a cell to possess designated reaction centers (RC) for that and to employ a separate strategy to expand the activity radius of those existing RCs. This is the employing of antenna pigments to harvest light. A photon absorbed by one of these antenna pigments creates an excitation which, through migration from molecule to molecule, is transferred to the RC. Compared to single pigments, these antennae greatly increase the amount of energy that can be absorbed [92].
This transfer to the RC, the second step in the photosynthetic process, usually follows an *energetic* and a *spatial* funnel. Pigments further away from the RC absorb higher-energy photons and those closer to the RC lower-energy ones. Funneling then transfers the excitation from higher-energy to lower-energy pigments, thus automatically nearing the RC.

The RC is a pigment-protein complex (PPC) , containing a special dimeric pigment pair that acts as donor upon electronic excitation due to transfer by neighboring harvesting pigments. This excited dimer then sets off an electron transfer cascade, transferring the electron from the initial acceptor molecule which becomes the donor for a secondary, spatially separated acceptor. This electron transfer process is coupled to the transfer of protons across a membrane, creating a proton gradient which then is used to drive the synthesis of ATP.

The main focus of quantum biology lies in the excitation energy transfer (EET) process, although nowadays the RC oxidation process is being increasingly more studied too. In green sulphur bacteria this transfer process takes place in a PPC which connects the chlorosome to the RC, as can be seen in Fig. 4.1, and is known as the Fenna-Matthews-Olson (FMO) complex (named after their discoverers) [96]. It is a bit like the "Drosophila melanogaster" of quantum biology – plenty of research centers around it since it exhibits a simple structure with nice properties. Indeed, it is the simplest PPC known and, even more important, it is relatively easy to isolate and crystallize, so that its structure is long since known. It even was the first chlorophyll-containing protein whose structure has been determined completely by X-ray crystallography (of Chlorobium limicola) [96]. The FMO possesses a trimeric structure with a C3-symmetry, one of its subunits is depicted in Fig. 4.2. Each of its three subunits consists of a protein scaffold (depicted semitransparent in the background) on which seven bacteriochlorophyll a (BChl a) molecules are attached. The spatial structure of each of the trimer's units is such that lowest-energy sites 3 and 4 (according to the original labeling by Fenna [96]) lie closest to the RC [97]. It should be noted that recently an eighth BChl a has been discovered [98, 99]. Easily discernible in Fig. 4.2, it is located somewhat outside (here to the right) of the rest of the chromophores of a given monomer, and closer to the next monomer of the C3 structure. Our discussion will be limited to the traditional seven-site complex though; for its influence on the EET we refer to [100].

### 4.3.2 Evidence of quantum effects in transport processes

Experimental evidence shows that energy transport through pigment-protein complexes is highly efficient [101]. For the extreme low-light conditions in which some phototropic species have been found, this of course is of vital importance. Recent studies on these highly specialised and evolved systems actually found traces of quantum, wave-like energy transport in the FMO complex [7, 9, 11]. While the first of these experiments were performed at cryogenic temperatures around 77 K, surprisingly subsequent studies yielded similar results for temperatures at 277 K, which is about room temperature [8]. At the moment a further increase of this temperature is not possible due experimental restrictions in working with the FMO probes.
In the following we first present the experimental method and the underlying physical principles to show why the results hint at the presence of quantum coherence in these complexes. Thereafter we turn towards theoretical modeling and analysis in Section 4.3.4, justifying the occurrence of the observed quantum effects. Deeper analysis with regard to the mechanism causing these effects are performed in Chapter 5.

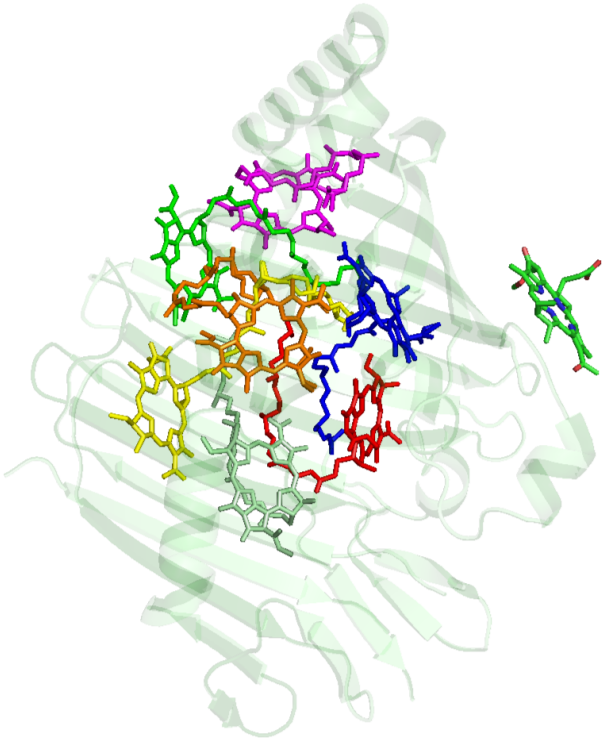

Figure 4.2: One of the FMO trimer's subunits. The protein environment, consisting mainly of alpha helices and beta sheets, is semitransparent in the background. Each BChl a molecule is colored differently. This representation is based on the protein data base entry with access number 3ENI, plotted with pymol.

### 4.3.3 Experimental methods

Among the basic experimental methods to investigate probes are absorption and fluorescence spectroscopy. However, PPCs generally exhibit a broad absorption band. Finer details – which would yield insightful information about their structure, function and EET dynamics – therefore are not accessible by these methods. Thus one resorts to more advanced spectroscopic techniques such as those presented below. The underlying physics of the light-matter interaction are exceptionally detailed exposed in [102]; a much more detailed account of spectral analysis is given in [103].

For a probe that exhibits sharp transition frequencies, the absorption band would in principle be highly structured. However, several effects lead to a broadening and smearing of these sharp features and result in a loss of structure and clearness of the spectrum. Among the most prominent of these effects are homogeneous and inhomogeneous broadening. Electronic transitions are accompanied by vibrational transitions in the protein environment and the chromophore itself, since for the electronic ground and excited states the nuclei have different equilibrium positions. These vibrational transitions lead to a broadening of the bare electronic transition which is termed "homogeneous broadening". Further broadening is achieved due to the so-called "static disorder". The different

chromophores in a protein ensemble usually exhibit slightly varying transition energies, due to effects like varying orientations of parts of the chemical structure or protein structure distortions. This "inhomogeneous broadening" also leads to broadening of spectra. Further discussion of these effects in the light of photosynthetic complexes can be found in [104, 105]. These effects, and especially the overlay of them, aggravate the interpretation of experimentally obtained spectra. Thus more advanced methods – such as non-linear spectroscopy – are necessary that allow for the separation, removal or identification of the single contributions to overcome this obstacle.

To describe the interaction between some material and an electric field, the electric displacement $D = \varepsilon_0 E + P$ is necessary. Here $\varepsilon_0$ is the vacuum permittivity and $P$ the (macroscopic) polarization as a response to the incident electric field $E$. In linear optics this response is assumed to be linear, $P = \varepsilon_0 \chi^{(1)} \cdot E$ (with the linear susceptibility $\chi^{(1)}$). When progressing to non-linear optics, higher-order effects become important and the polarization contains contributions by higher-order powers of the electric field

$$P = \varepsilon_0 \left( \chi^{(1)} \cdot E + \chi^{(2)} \cdot E \cdot E + \chi^{(3)} \cdot E \cdot E \cdot E + \ldots \right). \tag{4.2}$$

Since even-order susceptibilities vanish in media with inversion symmetry, the first observable non-linear contribution is the third. The polarization is given by the expectation value of the dipole operator which, with help of the density matrix $\rho$, is given by $P(t) = \mathrm{tr}\left[\mu\rho(t)\right]$. Thus the $n$'th order polarization can be obtained by the density matrix expansion $P^{(n)} = \mathrm{tr}\left[\mu\rho^{(n)}\right]$; the interaction with the electric field is given by an interaction Hamiltonian $H_{\mathrm{int}}(t) = \mu \cdot E(t)$ in the interaction picture. Thus with the $n$'th-order expansion of the density matrix and formal integration of the master equation we obtain

$$\begin{aligned} \rho^{(n)}(t) = \left(-\frac{i}{\hbar}\right) \int_{-\infty}^{t} d\tau_n \int_{-\infty}^{\tau_n} d\tau_{n-1} \ldots \int_{-\infty}^{\tau_2} d\tau_1 E(\tau_n) E(\tau_{n-1}) \cdot \ldots \cdot E(\tau_1) \\ \times U_0(t, t_0) \cdot \left[\tilde{\mu}(\tau_n), \left[\tilde{\mu}(\tau_{n-1}), \ldots \left[\tilde{\mu}(\tau_1), \rho(-\infty)\right] \ldots\right]\right] \cdot U_0^{\dagger}(t, t_0), \end{aligned} \tag{4.3}$$

where $U_0(t, t_0)$ is the propagator of the free evolution subject to Hamiltonian $H_0$ (with $H_0 = H - H_{\mathrm{int}}$ where $H$ is the full Hamiltonian) from time $t_0$ to time $t$, and the tilde again denotes moving to the interaction picture, one can transform this to reach the form

$$\begin{aligned} P^{(n)} = \int_0^{\infty} dt_n \int_0^{\infty} dt_{n-1} \ldots \int_0^{\infty} dt_1 E(t - t_n) \\ \times E(t - t_n - t_n - 1) \cdot \ldots \cdot E(t - t_n - \ldots - t_1) \cdot S(t_n, t_{n-1}, \ldots, t_1). \end{aligned} \tag{4.4}$$

Here a different time set has been adopted where times $t_k$ denote time intervals; $\tau_1 = 0$, $t_n = \tau_{n+1} - \tau_n$ and $t_n = t - \tau_n$. The newly defined $n$'th order nonlinear *response function* $S$ is given by

$$\begin{aligned} S^{(n)}(t_n, \ldots, t_1) = \left(-\frac{i}{\hbar}\right)^n \\ \times \mathrm{tr}\Big[\tilde{\mu}(t_n + \ldots + t_1) \left[\tilde{\mu}(t_{n-1} + \ldots + t_1), \ldots, \left[\tilde{\mu}(0), \rho(-\infty)\right] \ldots\right]\Big]. \end{aligned} \tag{4.5}$$

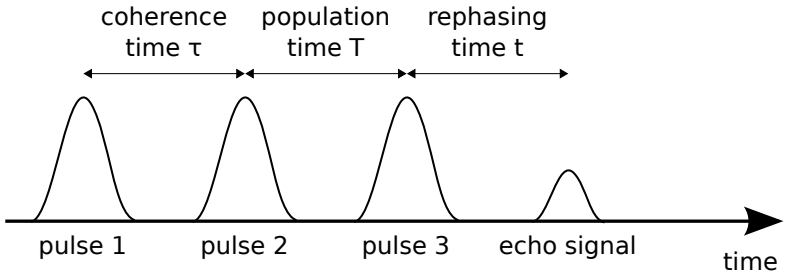


Figure 4.3: The three-pulse order used in typical two-dimensional photon echo spectroscopy and similar methods. Three pulses and the according evolution times in between them are denoted, followed by a response signal.

We now look at the experimental scheme briefly before highlighting its relation to the response function. The relevant phenomenon one exploits in such experiments is the "spin echo", or "photon echo" occurring in the rephasing direction. Upon applying a pulse to an ensemble of systems, a superposition between energy levels is created (using a $\pi/2$-pulse). Due to the slightly varying transition energies, each of the ensemble members starts oscillating at different frequencies for some time $\tau$. The ensemble dephases, each system accumulates a different phase. Then a reversing pulse ($\pi$-pulse) is applied, reversing the oscillation frequency but not changing its absolute value. This reverses the dephasing effect, leading to a rephasing after another time period $\tau$: the spin echo. When the rephasing happens, the probe emits a light pulse which echoes the original pulse. The great advantage of this procedure is that the static disorder is removed and no longer leads to an (inhomogeneous) broadening effect.
The spectroscopic methods use ultrafast pulses on the femtosecond timescale, i.e. of the order of $10^{-15}$. This pulse time scale is smaller than the fastest energy transfer times between chromophores, thus their dynamical processes become accessible. Typical experimental schemes apply three pulses to the probe implementing an advanced spin-echo scheme; their sequence is indicated in Fig. 4.3. The first pulse, as in the standard scheme, initialises the dephasing process which continues for the *coherence time* $\tau$. Then another pulse stops this dephasing, creating a population term which evolves for the *population time* $T$. The third pulse then reverses the dephasing process, leading to a photon echo in the rephasing direction, after the *echo time* $t$ – if each of the ensemble's systems remembers its initial phase and frequency.
However, if the individual phases and frequencies are subject to change, i.e. by the coupling to vibrational motions of the environment, the rephasing is attenuated or even completely avoided due to destructive interference. This allows to draw conclusions from the response signal (in the rephasing direction) about the environment's structure, but also about dynamical processes. The latter comes due to the fact that with increasing population time $T$ the chromophore is subject to interactions or energy transfer processes and thus loses its ability to fully rephase again. That way experimental variation of $T$ makes it possible to observe dynamical processes.

The actual experimental set-up is sketched in Fig. 4.4, which shows that the pulses in reality also have different directions with wave vectors $k_1$, $k_2$, and $k_3$. Due to con-

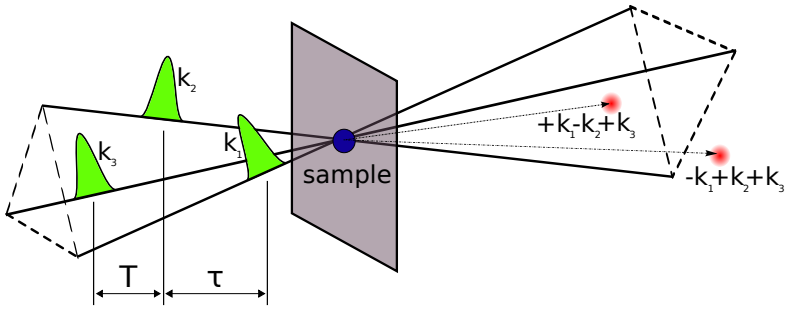


Figure 4.4: The three-dimensional set-up for a typical non-linear spectroscopy experiment. Three pulses hit the sample from three different spatial directions at three different times. The resulting rephasing and non-rephasing directions for homodyne detection pulses are indicated by red dots.

servation of momentum the photon echo occurs in a particular, predictable, so-called *phase-matched* direction. These directions can be selected for measurement by a mask behind the probe.
Experimental set-ups vary among different spectroscopic methods. Besides other techniques, like i.e. the three-pulse photon echo peak shift (3PEPS) spectroscopy, the two-dimensional photon echo spectroscopy (2D-PES) is one of the most powerful tools [104, 106]. With its help one can measure quantum beatings, a clear sign of quantum coherence between excitonic eigenstates in the protein complex, allowing quantification of quantum effects during energy transport.
The experimental response signal is accessible by analysing the response function from Eq. (4.5). In a more succinct form its third order is given by

$$S^{(3)}(t_1, t_2, t_3) = \frac{i}{\hbar^3} \mathrm{tr}\left[d\mathcal{G}_0(t_3)\,\mathcal{D}\mathcal{G}_0(t_2)\,\mathcal{D}\mathcal{G}_0(t_1)\,\mathcal{D}\rho(0)\right] \tag{4.6}$$

where the commutator is $\mathcal{D} = [d, \rho]$, the initial state is given by $\rho(0) = |g\rangle\langle g|$ and with $\mathcal{G}_0(t) = \exp(\mathcal{L}_0 t)\,\Theta(t)$ as the free evolution according to the Liouville superoperator $\mathcal{L}_0$ (times the Heaviside step function). This defines a nested commutator; in the resulting sum the dipole operator $\mu$ can act from the left and right side on the density matrix. This defines different physical processes, like absorption or stimulated emission. Since each of the pulses can have different effects, a variety of possible processes results. Double-sided Feynman diagrams, as in Fig. 4.5, allow to keep track of these and give them an easy representation. The vertical direction denotes time and the system's density matrix is given for the time intervals $\tau$, $T$ and $t$. Interactions with laser pulses are indicated by diagonal arrows. The time in between two interactions is subject to free time evolution. The result of such experiments is plotted as a function of $\omega_\tau$ and $\omega_t$ – the Fourier transform of the two varying times $\tau$ and $t$ for a fixed time $T$– yielding a two-dimensional spectrum. One fictitious two-dimensional spectrum is shown for a fixed time $T$, times $\tau$ and $t$ are Fourier transformed to yield the representation domain. The cross-section through the diagonal gives approximately the absorption spectrum, while off-diagonal peaks give information about energy transfer processes.
The already mentioned seminal paper by Engel *et al.* [7] produced evidence for quantum effects in these pigment-protein complexes through off-diagonal beatings. Subsequent

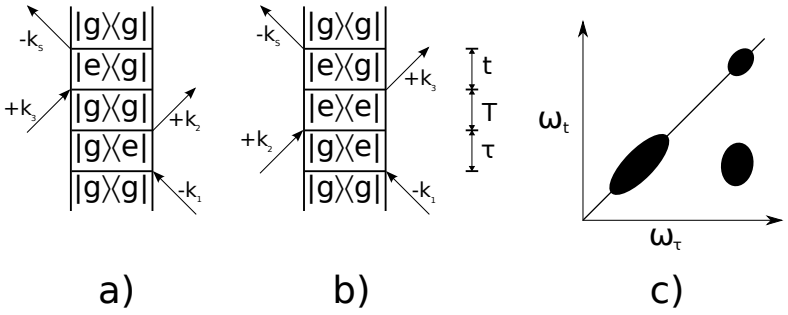


Figure 4.5: Feynman diagrams for three-pulse photon echo spectroscopy of a two-level system. (a) denotes a process called "ground state bleaching", whereas (b) shows "stimulated emission". $k_1$, $k_2$, and $k_3$ are the wave vectors of incoming pulses; $k_s$ is the system response (c) Sketch of a fictitious two-dimensional spectrum with one diagonal and one off-diagonal feature. The axis correspond to Fourier transformations of times $\tau$ and $t$; the plot is for a fixed population time $T$.

experiments [7, 9, 107, 11, 8] corroborated such evidence and lead the development of the field of quantum biology.

### 4.3.4 Theoretical methods

A manageable theoretical model for one of the FMO subunits is to consider it as a transport network where every of the $N$ chromophores can host an electronic excitation (a Frenkel exciton). Their spatial distribution is set by the surrounding protein scaffold to which these bacteriochlorophyll molecules are attached. This configuration can be simplified by reducing the bacteriochlorophyll molecules to two-level systems that can be excited or de-excited and that are coupled to each other via dipolar interaction. Furthermore the protein scaffold is replaced by a suitably modeled environment. The treatment of this last approximation is where the main difficulty and the great discrepancies of theoretical results in different numerical simulations come from, since the environment can be accounted for in almost arbitrarily complex ways.

The general form of the PPC thus is given by

$$H = \sum_{i=1}^{N} E_i |i\rangle\langle i| + \sum_{i \neq j} J_{ij} |i\rangle\langle j| + \sum_i H_{\mathrm{int},i} + \sum_i H_{\mathrm{env},i} \tag{4.7}$$

where $|i\rangle$ is the state of a single chromophore with label $i$ and $E_i$, $J_{ij}$ denote its energy and couplings to sites $j$. While the first two terms describe the excitonic part $H_{\mathrm{ex}}$ of the complex in itself, the second two introduce a single environment $H_{\mathrm{env},i}$ for each site $i$ as well as the interaction $H_{\mathrm{int,i}}$ with it as

$$H_{\mathrm{env},i} = \sum_k \hbar\omega_k a_{i,k}^\dagger a_{i,k} \tag{4.8}$$

$$H_{\mathrm{int},i} = \sum_k g_{ik}\omega_k \left(a_{i,k}^\dagger + a_{i,k}\right) |i\rangle\langle i|. \tag{4.9}$$

The environments are modeled by harmonic oscillators here, the oscillator of environment $i$ and frequency $\omega_k$ is described by the annihilation and creation operators $a_{i,k}$ and $a_{i,k}^\dagger$. The coefficients $g_{ik}$ define the spectral density for site $i$ as $J_i(\omega) = \sum_k g_{ik}\omega_k^2\delta(\omega-\omega_k)$. Thus each site $i$ is connected to its own, independent bath. This is an assumption corroborated by numerical studies on photosynthetic complexes [108, 109].
As a last ingredient the rates $\gamma_{\text{loss}}$ and $\gamma_{\text{out}}$ need to be accounted for. The former represents the spontaneous loss of the excitation into the general environment while the latter represents the (intended) exiting of the excitation from site 3 into the RC. These two contributions are accounted for by typical Lindblad terms [16].
The full equation of motion for the photosynthetic complexes with density matrix $\rho$ then is described by

$$\begin{aligned}\frac{d}{dt}\rho = &-\frac{i}{\hbar}\left[H,\rho\right]\\ &-\gamma_{\text{loss}}\sum_{i=1}^{N}\left(|n\rangle\langle n|\rho+\rho|n\rangle\langle n|-2|0\rangle\langle n|\rho|n\rangle\langle 0|\right)\\ &-\gamma_{\text{out}}\left(|3\rangle\langle 3|\rho+\rho|3\rangle\langle 3|-2|0\rangle\langle 3|\rho|3\rangle\langle 0|\right),\end{aligned} \tag{4.10}$$

where $|0\rangle$ is the electronic ground state of the pigment protein complex and $H$ is the full Hamiltonian (4.7).

The necessary parameters – site energies $E_i$ and dipolar coupling strengths $J_{ij}$ – are subject to experimental identification. In 2006, Adolphs *et al.* introduced an electrostatic method to calculate optical transition energies of pigments in protein environments. Applied to the FMO of Prosthecochloris aestuarii and Chlorobium tepidum they were able to calculate experimental optical spectra instead of fitting them; the calculation was based on dipolar energies of pigments calculated largely from first principles [97].
We apply these parameters from [97]; namely site energies from Table 4, obtained by the fitting of optical spectra for FMO-monomers and trimers, as well as dipolar couplings from Table 1, and thus obtain the Hamiltonian

$$H = \begin{pmatrix} 445 & \mathbf{-87.7} & 5.5 & -5.9 & 6.7 & -13.7 & -9.9\\ \mathbf{-87.7} & 520 & \mathbf{30.8} & 8.2 & 0.7 & 11.8 & 4.3\\ 5.5 & \mathbf{30.8} & 205 & \mathbf{-53.5} & -2.2 & -9.6 & 6.0\\ -5.9 & 8.2 & \mathbf{-53.5} & 335 & \mathbf{-70.7} & -17.0 & \mathbf{-63.3}\\ 6.7 & 0.7 & -2.2 & \mathbf{-70.7} & 490 & \mathbf{81.1} & -1.3\\ -13.7 & 11.8 & -9.6 & -17.0 & \mathbf{81.1} & 640 & \mathbf{39.7}\\ -9.9 & 4.3 & 6.0 & \mathbf{-63.3} & -1.3 & \mathbf{39.7} & 450 \end{pmatrix} \tag{4.11}$$

where the diagonal elements were shifted by 12000 $\text{cm}^{-1}$ for better readability. Large couplings are written in boldface. All parameters are expressed in units of $\text{cm}^{-1}$ and hold for Chlorobium tepidum; those of Prosthecochloris aestuarii exhibit a similar behaviour [97].
For realistic simulations we also need to model the environment's spectral density in a realistic way. The perfect solution for this is of course to determine the spectral density $J(\omega)$ defined by the protein environment, inserting with its help the couplings $g_{i,k}$ into Eq. (4.9) and thus solve Eq. (4.10) where the description of the environment enters via the full Hamiltonian $H$. In general however this procedure is nearly unfeasible due to the

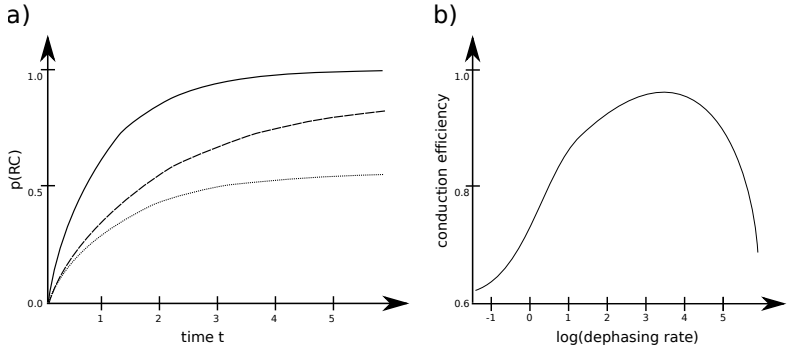


Figure 4.6: Transport properties of the PPC network. (a) Probability $p(RC)$ for an excitation to reach the RC instead of being lost to the environment, shown for different dephasing rates. The lowest line results from zero dephasing, the highest from an optimal value. (b) The complex conductivity for excitation transport from site 1 through the PPC to site 3. An intermediate level of noise is clearly beneficial to maximize transport. For details see [111, 79].

resulting complexity of the system-plus-environment combination. Therefore, to obtain a first intuition of the dynamics, FMO complexes from Chlorobium tepidum [110] and Prosthecochloris aestuarii [111] have been investigated employing simpler environment models.

Following the investigations in [111], the system-environment interaction can be treated perturbatively, deriving a master equation for the FMO complex. Excitation injection is modeled by a rate $\gamma_{\text{in}}$, feeding excitations to site 1. It is taken to be much smaller than the rate $\gamma_{\text{out}}$ at which excitations leave the network to the RC. These properties define low-light conditions, the mean population in the network thus remains well below unity at all times.
While the employed assumptions are far from the actual situation, this procedure still yields interesting insights. In Fig. 4.6 the approximate conductivity of the PPC is shown. Two regimes can be discerned. The first is the classical case. Plenty of noise is present, quantum effects are suppressed by the environment due to instant dephasing of any present coherences. Transport in this regime is described by a classical rate equation, describing the "hopping" of excitations between neighboring sites. The physical model corresponding to this hopping is Förster resonance energy transfer (FRET) [112], enabling EET between a donor- and an acceptor chromophore. In the second case, the quantum case, transport instead happens in a "wave-like" fashion. Quantum coherence is exploited to propagate a wave packet through all possible pathways of this complex at once. Interference effects come into play, possibly blocking or enabling different pathways.
As can be seen in Fig. 4.6, the absence of dephasing (essentially quantum) as well as the presence of plenty of dephasing (essentially classical) leads to poor results with low conduction efficiency. The intermediate regime however, with some noise present, shows increased transfer to the RC [113, 114, 78]. The fact that the dynamics of this complex stand in the intermediate regime between quantum and classical can already be inferred

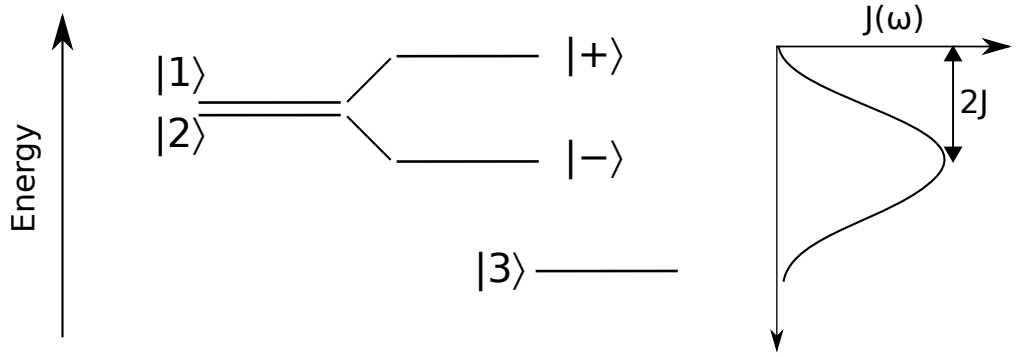


Figure 4.7: Schematic representation of the phonon antenna principle. The levels $|1\rangle$ and $|2\rangle$ exhibit a small energy difference but strong dipolar coupling, leading to their splitting into an excitonic manifold $|\pm\rangle$. When the energy difference of the manifold's states matches the environment's maximum, transport to the level $|3\rangle$ is optimized. Thus the levels $|1\rangle$ and $|2\rangle$ act as an antenna, harvesting environmental fluctuations and concurrently enhancing transport.

from the fact that the intra-system couplings in Hamiltonian (4.11) are of the same order of magnitude than the couplings to the environment. A more detailed analysis of the actual role the environment and its properties play in the system's dynamics is deferred to Chapter 5; a first, qualitative understanding is already accessible though.

Reducing complexity to highlight the effect, let us regard a transport complex built of three sites. Two of them are fixed in energy, namely site 1 which receives an excitation and thus acts as the source, as well as site 3 which is coupled to the target and thus acts as a drain. Given complete freedom of parametric choices upon adding the site 2 to this configuration, how should one choose its energy and dipolar couplings to guarantee optimal transport properties of the resulting configuration?
The spectral density is assumed to possess only a single maximum, shaped as depicted in Fig. 4.7, and is accounted for by the use of Redfield equations (see Section 2.3). Numerical studies then find that site 2 exhibits a similar excitation energy as site 1, as well as a strong dipolar coupling between the two. This strong dipolar interaction arises due to spatial proximity. Theoretical and numerical details of this procedure can be found in References [113, 114].
This set-up constitutes a *phonon antenna*. Due to the strong dipolar interaction between sites 1 and 2, it is reasonable to employ an excitonic picture (corresponding to the quantum optical dressed-state picture). Then the interaction Hamiltonian (4.9) can be rewritten in the excitonic eigenstates $|e_n\rangle$ which are related to the site-basis eigenstates $|i_n\rangle$ via $|i\rangle = \sum_n c_n^i |e_n\rangle$, yielding

$$H_{\mathrm{int},i} = \sum_{n,m} \left(Q_{nm} |e_n\rangle\langle e_m| + \mathrm{h.c.}\right) \tag{4.12}$$

with coupling coefficients

$$Q_{nm} = \sum_i \sum_k g_{ik}\omega_k \left(a_{i,k}^\dagger + a_{i,k}\right) c_{i,n} c_{i,m}. \tag{4.13}$$

This results in a two-fold effect. The environment-induced dephasing now couples excitonic manifolds, facilitating transport to the lower-energy state. Optimally the energy difference between the two excitonic states is now resonant with the spectral density's maximum. This way the environment's fluctuations can ideally support transitions between these states. The magnitude of this gap is tuned by the site energies and dipolar couplings, determining the resulting energy difference in the dressed-state picture [79].
Alone the combination of these two points yields results that are already comparatively close to more exact numerical treatments. Further it should be mentioned that these considerations, albeit achieved for a small subsystem, apply to the full FMO complex as well. Experimental evidence has been found that for the pathway from site 1 to site 3 (in one FMO subunit) the BChl are located spectrally and spatially in such a way that they efficiently sample the environment's spectral density [113, 114].
These results fit in well with the observation of increased transport in intermediate noise regimes. The presence of a certain amount of noise is necessary to exploit the advantage provided by the splitting in excitonic states. Given that too much noise leads to essentially classical behaviour, the intermediate regime combines the advantages of both regimes to provide efficient energy transfer [79, 78].

### 4.3.5 Numerical methods

Despite their comparatively simple nature, these theoretical studies however already provide some enlightening physical insights that lead towards the understanding of the role that an environment plays in such complex biological systems. It is only natural to extend these models – mostly by introducing more sophisticated descriptions of the environment – largely drawing on open quantum system methods such as, but not limited to, those presented in Chapter 2 and especially in Section 2.6. An introductive overview of numerical studies on light-harvesting PPCs is given in [115].
A first step towards the understanding of the influence that a more intricate environment has usually consists of employing the HEOM method for simulation. Although it draws on an infinite hierarchy of coupled equations, for a finite timescale of phonon dynamics this hierarchy can be truncated at a finite depth [78]. Especially the extension of this algorithm to GPUs has largely increased its applicability. In spite of the difficulties that arise due to highly connected auxiliary density matrices, progress can be made by minimizing communication between parallel execution threads such as achieved by advanced partitioning schemes. Adaptive integration methods yield further speed improvements. The combination of these methods, implemented on the highly parallelized platform yielded by GPUs, makes advanced analysis even of complex systems like light harvesting antenna complexes feasible [116].
In the finite temperature regime, QUAPI also has yielded some interesting results. Especially the excitation transport in photosynthetic complexes for the presence of harmonic environments has been investigated thoroughly. While QUAPI largely depends on finite temperatures for a fast enough decay of correlations, temperatures that are not too far below typical system frequencies can be reached [117, 78].
In the next two chapters we proceed towards a more detailed model of the environment, employing TEDOPA to investigate the environment's influence on quantum coherence and dynamics. TEDOPA's capabilities in treating arbitrarily shaped spectral densities surpasses by far the previously mentioned methods and makes it the method of choice to investigate the complex interplay of system and environment in biological systems.

# CHAPTER 5

## Electronic coherence and recoherence in PPCs

In Chapter 4 we encountered recent observations of oscillatory features in the optical response of photosynthetic complexes that revealed evidence for surprisingly long-lasting electronic coherences which can coexist with energy transport. These observations have ignited multidisciplinary interest in the role of quantum effects in biological systems, including the fundamental question of how electronic coherence can survive in biological surroundings. In this chapter we show that the non-trivial spectral structures of protein fluctuations can generate non-equilibrium processes that lead to the spontaneous creation and sustenance of electronic coherence, even at physiological temperatures. To account for such complex environmental structures we need to model it in a more sophisticated manner. By employing TEDOPA simulations (see Section 3.4) to treat such PPCs exemplary, we provide a firm microscopic basis to successfully reproduce the experimentally observed coherence times in the FMO complex and illustrate how detailed quantum modeling and simulation can shed further light on a wide range of other non-equilibrium processes which may be important in different photosynthetic systems.
The material presented in this chapter has first been published in [1] and this chapter is largely based on the accounts given in it.

## 5.1 Motivation

Uncovering the underlying biological design principles of the remarkable quantum efficiency of almost 100% that EET in PPCs feature could inspire important new developments in artificial light harvesting technologies [118]. Indeed, the potential novelty of a biomimetic approach to light-harvesting is underlined by the unexpected observation of robust, long-lasting oscillatory features in 2-D spectra of PPCs extracted from bacteria, algae and higher plants. Using ultrafast nonlinear spectroscopy, sustained beating *between* optically excited states lasting several hundreds of fs at room temperature, and up to nearly 2 ps in the FMO complex at 77 K, have been observed [7, 8, 9, 10, 11]. These experiments have been interpreted as evidence for *electronic* coherences between excitons, with lifetimes which are, surprisingly, over an order of magnitude larger than coherences between electronic ground and excited states [10]. Such coherence times

are long enough for EET and excitonic coherence to coexist, conditions under which a sophisticated interplay of quantum and dissipative processes theoretically optimises transport efficiency [110, 111, 119, 120].

While many proposals for how quantum effects might enhance biological light-harvesting have been advanced over the last five years, most of these have used simple, phenomenological methods to *include* decoherence [110, 111, 119, 120, 121]. In this letter we tackle the more fundamental problem of elucidating the microscopic mechanisms through which the wide range of electronic coherence times observed in PPCs actually arise. By including full temperature dependence into the numerically exact TEDOPA, we show that the presence of resonant structure in the spectral function of PPC chromophores leads to non-equilibrium quantum dynamics in which picosecond electronic coherence can be driven and supported by quasi-coherent interactions between excitons and spectrally sharp vibrational environment modes [122, 123, 124, 125]. Moreover, both the decay of ground-excited state coherences and the excitation energy transport exhibit the correct time scales, thus explaining three crucial observations within the same model. We complement our numerics with an approximate semiclassical model that illustrates the essential physical mechanisms by which discrete modes, driven far from equilibrium by exciton injection, may *spontaneously generate* and sustain oscillatory EET and electronic coherence against aggressive background decoherence, and which also helps to isolate the roles of other processes, such as non-Markovian pure dephasing [126, 127]. Under these conditions, energy transport proceeds in a non-equilibrium fashion, transiently violating the detailed balance conditions which are often invoked to set fundamental limits on light harvesting efficiency [128]. The requirements for observing this striking behaviour in ensemble experiments are discussed in Section 5.7.

## 5.2 The microscopic model

The electronic Hamiltonian of a PPC consists of a network of chromophoric sites, denoted $|i\rangle$, each supporting a single optical excitation of energy $\epsilon_i$ which can transfer coherently onto another site $j$ via a (dipolar) interaction amplitude $J_{ij}$

$$H = \sum_i \left( (\varepsilon_i + X_i) \, |i\rangle\langle i| + H_{\mathrm{env},i} \right) + \sum_{i \neq j} J_{ij} |i\rangle\langle j|. \tag{5.1}$$

Each excitation is also linearly coupled in their excited states to local environmental fluctuations which are modeled as independent continua of harmonic vibrational modes [110, 111]. These fluctuations can be due to vibrations in the surrounding protein matrix and/or intra-chromophore vibrational modes. Defining bosonic annihilation and creation operators $a_{i,k}, a_{i,k}^\dagger$ for the $k$'th independent oscillator coupled to site $i$, and denoting an optical excitation on site $i$ by the state $|i\rangle$, the Hamiltonian ($\hbar = 1$) for a single electronic

excitation can be written as

$$H = H_{\text{sys}} + H_{\text{int}} + H_{\text{env}} \tag{5.2}$$

$$H_{\text{sys}} = \sum_i \epsilon_i |i\rangle\langle i| + \sum_{i \neq j} J_{ij} |i\rangle\langle j| \tag{5.3}$$

$$H_{\text{int},i} = \sum_i X_i |i\rangle\langle i| \tag{5.4}$$

$$H_{\text{env},i} = \sum_{i,k} \omega_k a_{i,k}^\dagger a_{i,k} \tag{5.5}$$

where coupling to the vibrational modes of the environment induces local energy fluctuations via the mode displacement operators $X_i = \sum_k g_{i,k}(a_{i,k} + a_{i,k}^\dagger)$ with $\omega_k$ being the frequencies of the vibrational fluctuations and $g_{i,k}$ their coupling strength to state $|i\rangle$. The optical excited states $|i\rangle$ have coherent coupling matrix elements (arising from dipolar coupling) $J_{ij} = J_{ji}$. This coupling leads to delocalized *excitonic* eigenstates $|e_n\rangle$ which obey $E_n|e_n\rangle = H_{\text{sys}}|e_n\rangle$ with energies $E_n$ (we order the states such that $E_1$ is the lowest energy excitation). Finally, we assume, for simplicity only, identical, independent vibrational environments on each site characterised by a spectral density $J(\omega) = J_i(\omega) = \sum_k g_{i,k}^2 \delta(\omega - \omega_k)$. Defining the Huang-Rhys factor $S_{i,k} = \sqrt{\frac{g_{i,k}}{\omega_k}}$, we arrive at the form $J_i(\omega) = \sum_k S_{i,k}\omega_k^2 \delta(\omega - \omega_k)$ for the spectral function.

Rewriting the Hamiltonian of Eq. (5.2) in the exciton basis using $|i\rangle = \sum_n C_n^i |e_n\rangle$, we obtain

$$H = \sum_n E_n |e_n\rangle\langle e_n| + \sum_{n,m} Q_{nm} |e_n\rangle\langle e_m| + \sum_{i,k} \omega_k a_{i,k}^\dagger a_{i,k}, \tag{5.6}$$

where the new couplings to the bath are given by

$$Q_{nm} = \sum_{i,k} \sqrt{S_{i,k}}\omega_k C_n^i C_m^i \left(a_{i,k} + a_{i,k}^\dagger\right). \tag{5.7}$$

The coefficients $C_n^i$ can be taken as real, so $Q_{nm} = Q_{mn}$. All bath modes are taken to be independent, i.e. $\left[a_{i,k}, a_{j,l}^\dagger\right] = \delta_{ij}\delta_{kl}$. In this basis, we see that the environment now couples to both the energy level populations (diagonal coupling) and can induce transitions between exciton states (off-diagonal coupling). Although transverse terms are important for the semiclassical driving of new exciton coherences by the modes, the diagonal terms are important in the initial excitation of the mode oscillations, especially when starting from an exciton population state.

The spectral function used to characterize the environment acting on each site in the TEDOPA simulations is given by

$$J(\omega) = J_0(\omega) + \sum_{i=1}^{2} S_i \omega_i^2 \delta(\omega - \omega_i), \tag{5.8}$$

$$J_0(\omega) = \frac{\lambda\left[1000\omega^5 e^{-\sqrt{\frac{\omega}{\omega_a}}} + 4.3\omega^5 e^{-\sqrt{\frac{\omega}{\omega_b}}}\right]}{9!(1000\omega_a^5 + 4.3\omega_b^5)}. \tag{5.9}$$

Equation (5.8) shows that this spectral function contains two distinct components, a broad spectrum $J_0(\omega)$ - which we refer to as the "background" spectral density - and couplings to specific (discrete) vibrational modes which are sharp/underdamped. The exciton dynamics generated by interactions with these two contributions are very different. The key findings presented here only arise from the consideration of this *structured* spectral functions.
The bath parameters used throughout are $S_1 = 0.12, S_2 = 0.22, \omega_a = 0.57\text{cm}^{-1}$ and $\omega_b = 1.9\text{cm}^{-1}$. These parameters were extracted from experiments in [97, 129]. Vibrational modes with similar frequencies have also been experimentally observed in the FMO complex in [123, 125]. The reorganization energy used in our simulations is $\lambda = 35\text{cm}^{-1}$, taken again from [97]. The same spectral function is used for the semiclassical simulations, except the $37\text{cm}^{-1}$ mode is excluded. Due to the authors (Adolphs and Renger) of [97], we denote this spectral density as AR.

## 5.3 The physical mechanism of vibration-induced electronic coherence

From Eqs. (5.6) and (5.7), we see that the exciton-environment interaction contains transverse (non-adiabatic) terms which couple *different* excitonic states through the bath displacement operators. Neglecting non-Markovian effects, the strongly-damped response of the background environment drives incoherent exciton relaxation through these terms [123]. However, coupling to sharp (underdamped), quasi-resonant discrete modes allows for the possibility of *coherent* and reversible inter-exciton transitions via the long-lasting mechanical (coherent) motion of the mode displacements. From Eqs. (5.6) and (5.7), the initial (fast) injection of an exciton, *either* coherently or incoherently, creates a sudden force on the discrete modes which initiates transient oscillations at approximately their natural frequency $\omega_k$. To first order these transients can be treated as coherent oscillations and their back action on the excitons then acts essentially like a time-dependent field that drives *coherent*, Rabi-like transitions between dissipative exciton states via the Hamiltonian terms

$$H_{driving} \approx \frac{1}{2} \sum_{n \neq m} (\langle Q_{nm} \rangle(t) |e_n\rangle\langle e_m| + h.c.), \tag{5.10}$$

where $\langle Q_{nm} \rangle(t) \propto \sum_{i,k} \sqrt{S_k}\omega_k C_n^i C_m^i \sin(\omega_k t)$.
Heuristically, this non-equilibrium, laser-like driving essentially generates *new* electronic coherences in the system to replace those that are continuously damped out by the fluctuations of the smooth background environment. The actual (coupled) motion of the excitons and modes is more complex, and may also interact with non-Markovian dynamics of the background, but the physical picture presented here illustrates a key point: electronic coherence may emerge from transiently exciting robust, *weakly* dephasing vibrational coherences which are then used to later back-transfer coherence to the excitons, a novel type of coherence generation and storage (see [130, 131, 132, 133, 134, 135] for related observations that non-equilibrium systems may generate or maintain quantum entanglement).
We should stress that this (re)generating of electronic coherence is a very different concept from *protection* of coherences by spatial correlations, non-Markovianity, or intrinsically weak environmental dephasing [136, 120, 126, 127]. Crucially, mode-driven

coherences will be prominent whenever vibrational modes have frequencies comparable to exciton energy differences of strongly coupled chromophores and have dephasing times on picosecond timescales. Many examples of such modes have been observed experimentally in PPCs, such as the FMO complex [122, 123, 124, 125], but their importance as elements in designing efficient transport structures – such as the recently proposed "phonon antenna" [113] – and for interpreting experimental observations in multidimensional spectroscopy has only just begun to be appreciated [5, 137, 138]. This mechanism, based on resonant driving of inter-exciton transitions, will not regenerate or sustain ground to excited state coherence, as the environment does not couple these states. This framework provides a natural understanding of the distinct coherence time scales in the problem which may also be of relevance for photosynthetic charge transfer dynamics [139].

## 5.4 Semiclassical equations of motion

We have developed a theory in which the key process mediated by the discrete modes can be interpreted as a quasi-coherent driving of the exciton system by the coherent displacement of the modes. This suggests that a significant part of the interactions between the discrete modes and the excitons could be accounted for in a semiclassical approximation. To derive the semiclassical equations of motion which were used to investigate exciton dynamics in the FMO complex, we treat the discrete modes as part of the system and account for the effects of the background environment using a simple Bloch-Redfield approach. The effective system Hamiltonian is the same as Eq. (5.6), but the sum over bath modes is restricted to just the two discrete modes that appear in the spectral function of Eq. (5.8). We then use the Heisenberg picture to compute exact equations of motion for the mode displacements $X_{i,k}(t) = \langle a_{i,k}(t) + a^\dagger_{i,k}(t)\rangle$ and their momenta $P_{i,k}(t) = \langle a_{i,k}(t) - a^\dagger_{i,k}(t)\rangle$, where $A(t) = e^{iHt}Ae^{-iHt}$ denotes operators in the Heisenberg picture. The expectation value refers to the operation $\langle A\rangle = \mathrm{tr}\,[\rho_{total}(t)A]$. In this notation the index $i$ refers to modes coupled to site $i$ and the $k$ index labels the different discrete modes at each site i.e. the modes of frequency $\omega_k$ in Eq. (5.8). As an example, the equation of motion for the momentum operator is

$$\begin{aligned}\frac{d}{dt}(a_{i,k}(t) - a^\dagger_{i,k}(t)) = \; & i[H, (a_{i,k}(t) - a^\dagger_{i,k}(t))] \\ = \; & -i\omega_i(a_{i,k}(t) + a^\dagger_{i,k}(t)) \\ & + 2i\sqrt{S_k}\omega_k \sum_n |C^i_n|^2 |e_n\rangle\langle e_n|(t) \\ & + 2i\sqrt{S_k}\omega_k \sum_{n\neq m} C^i_n C^i_m |e_m\rangle\langle e_n|(t).\end{aligned} \tag{5.11}$$

Taking the expectation value of this equation of motion by using the result $\langle |e_m\rangle\langle e_n|(t)\rangle = \mathrm{tr}\,[\rho_{total}(t)|e_m\rangle\langle e_n|] = \rho_{e_n e_m}(t)$, where $\rho_{e_n e_m}(t)$ are the matrix elements of the reduced density matrix of the excitons, we arrive at the equation of motion for the expectation

values

$$\begin{aligned}\frac{dP_{i,k}(t)}{dt} =& -i\omega_i X_{i,k}(t) \\ &+ 2i\sqrt{S_k}\omega_k \sum_n |C_n^i|^2 \rho_{e_n e_n}(t) \\ &+ 2i\sqrt{S_k}\omega_k \sum_{n\neq m} C_n^i C_m^i \rho_{e_n e_m}(t)\end{aligned} \tag{5.12}$$

and analogously for the position operator

$$\frac{dX_{i,k}(t)}{dt} = -i\omega_k P_{i,k}(t). \tag{5.13}$$

The semiclassical approximation amounts to replacing the mode operators in Eq. (5.6) by these time-dependent $c$-number expectation values, creating a time-dependent Hamiltonian $H_{X_i}(t)$ for the excitons. We evolve the reduced density matrix of the exciton system according to

$$\frac{d\rho_{\rm sys}(t)}{dt} = -i\left[H_{X_i}(t), \rho(t)\right] + \mathcal{R}(t)[\rho_{\rm sys}(t)], \tag{5.14}$$

where we have added a dissipative term $\mathcal{R}(t)$ that accounts for a background environment described by the smooth background part of the spectral function of Section 5.2. The Redfield relaxation tensor $\mathcal{R}(t)$ in Eq. (5.14) is computed in the absence of the discrete modes and is restricted to secular (energy-conserving) terms only. The full equation and expressions for the relaxation and dephasing rates contained in $\mathcal{R}(t)$ are given explicitly in [20, 140]. However, the time argument is included in $\mathcal{R}(t)$ to denote that some of the rates – corresponding to pure dephasing – are non-standard, and are actually time-dependent. This will described in Section 5.4.1.

In all simulations the initial mode displacements and momenta are drawn from a thermal distribution at temperature $T$. A phenomenological damping rate $\gamma$ for the modes, which is assumed to be the same for both modes, is set to give a typical damping time for vibrational motion of 1 ps [97, 122]. Thus Eq. (5.12) is replaced by

$$\begin{aligned}\frac{dP_{i,k}(t)}{dt} =& -2\gamma P_{i,k}(t) - i\omega_i X_{i,k}(t) \\ &+ 2i\sqrt{S_k}\omega_k \sum_n |C_n^i|^2 \rho_{e_n e_n}(t) \\ &+ 2i\sqrt{S_k}\omega_k \sum_{n\neq m} C_n^i C_m^i \rho_{e_n e_m}(t).\end{aligned} \tag{5.15}$$

For completeness, the equation of motion for the density matrix elements $\rho_{e_n e_m}(t) = \langle e_n|\rho_{\rm sys}(t)|e_m\rangle$ are

$$\begin{aligned}\frac{d\rho_{e_n e_m}(t)}{dt} =& -iE_{nm}\rho_{e_n e_m}(t) - i\sum_j Q_{nj}(t)\rho_{e_j e_m}(t) \\ &+ i\sum_j Q_{jm}\rho_{e_n e_j}(t) + \sum_{j,l} \mathcal{R}_{nmjk}\rho_{e_j e_l}(t),\end{aligned} \tag{5.16}$$

where $Q_{nm}(t) = \sum_{i,k} \sqrt{S_k}\omega_k C_n^i C_m^i X_{i,k}(t)$. From Eq. (5.16) we see that the mode displacements lead to time-dependent couplings of populations and coherences which generate the "driving" of inter-exciton transitions mentioned in the previous section to enhance coherence lifetimes and generate new coherences. Oscillatory population dynamics also appear through the coupling of populations to coherences mediated by the discrete modes. One can immediately see from the structure of these equations that discrete modes cannot drive $|e_n\rangle\langle g|$ coherences, and thus do not regenerate or support ground-excited coherence. However, these equations do predict $\rho_{e_n g} \rightarrow \rho_{e_m g}$ coherence transfers due to coherent motion of the discrete modes which lead to rapid suppression of coherence except for the lowest exciton. For each set condition of initial mode conditions drawn from the thermal distribution, the equations of motion for $X_i(t), P_i(t)$ Eqs. (5.13), (5.15), and Eq. (5.16) are integrated together, and these trajectories are averaged over to obtain the results of Fig. 5.3 in the next section.
We finally note that in this simple description, quantum fluctuations of the discrete modes are neglected, as are the renormalization effects of the background environment. This last approximation is appropriate for the relatively weak coupling parameters used for the background spectral density. All of these effects are captured by the TEDOPA simulations. The main qualitative differences were observed in the $|e_n\rangle\langle g|$ coherences, where amplitude modulations due to quantum fluctuations of the discrete modes could not be reproduced by the semiclassical approach, leading to an overestimate of coherence times.

### 5.4.1 Non-Markovian pure dephasing rates

In standard, secular Bloch-Redfield theory, the Markovian pure dephasing rate $\Gamma_{pd}$ (which causes decoherence of energy eigenstate superpositions in the absence of energy relaxation) at temperature $T$ for a spectral density $J(\omega)$ is (neglecting matrix elements) proportional to

$$\begin{aligned}
\Gamma_{pd} &\propto \lim_{\epsilon\to 0} \int_0^\infty dt \int_0^\infty d\omega J(\omega) \coth\left(\frac{\beta\omega}{2}\right) \cos\left((\omega-\epsilon)t\right), \\
&\propto \lim_{\epsilon\to 0} \pi \int_0^\infty d\omega J(\omega) \coth\left(\frac{\beta\omega}{2}\right) \delta(\omega-\epsilon), \\
&\propto \lim_{\epsilon\to 0} \left[\pi J(\epsilon) \coth\left(\frac{\beta\epsilon}{2}\right)\right], \\
&\propto \lim_{\epsilon\to 0} \left[2\frac{\pi}{\beta\epsilon} J(\epsilon)\right], \qquad (5.17)
\end{aligned}$$

where $\beta$ is the inverse temperature $\beta = 1/k_B T$. The pure dephasing rate is thus controlled by the behaviour of the spectral function approaching zero frequency [126, 127], as one would expect for a process that involves no energy dissipation. Typical spectral densities have power-law dependences at low frequency $J(\omega) \propto \omega^s$, with $s$ some exponent. For super-Ohmic damping, the limit in Eq. (5.17) is zero, and thus pure dephasing is apparently absent for this class of spectral functions [127]. This can considerably weaken the temperature dependence of dephasing, which can now only occur through energy relaxation in Bloch-Redfield theory [126]. The AR spectral function of Section 5.2 is in this class. The commonly encountered Ohmic spectral density ($s = 1$) leads to a finite limit and a pure dephasing rate proportional to temperature [126]. The relevance of this observation has recently been discussed in the context of PPC dynamics

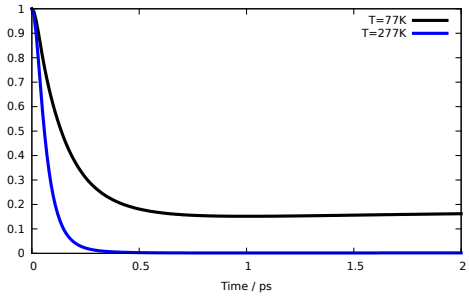


Figure 5.1: Plot of the coherence element $\rho_{12}(t) = \rho(0)e^{-\int_0^t \Gamma_{pd}(t')dt'}$ over time. Initial condition is $\rho(0) = 1$ and the transient, non-Markovian pure dephasing rate is computed using Eq. (5.18) for the spectral density from Section 5.2. Results are shown at $T = 77$ K and $T = 277$ K. The vanishing of the dephasing rate at long times leads to the survival of a finite value of coherence at long times.

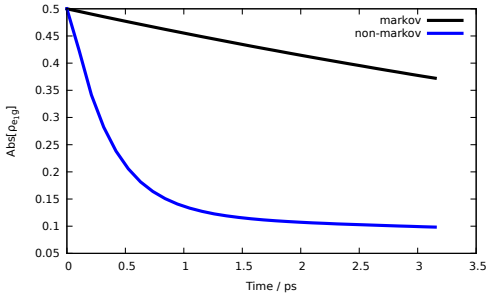


Figure 5.2: Abs$[\rho_{e1g}(t)]$, for the standard, secular Bloch-Redfield theory (Black line) and for the generalised theory which includes a time-dependent pure dephasing rate (Blue line). Initial condition is $2\rho(0) = |e_i\rangle\langle e_i| + |g\rangle\langle g| + |e_i\rangle\langle g| + |g\rangle\langle e_i|$ and the bath is at $T = 77$ K. Calculations are for the full FMO system.

[126, 127], and the absence of pure dephasing in super-Ohmic spectral densities has been put forward as a means of prolonging excitonic coherence whilst maintaining efficient energy transport [127].
However, the pure dephasing *rate* goes to zero in the full Markov approximation due to the fact that the upper limit in the integral over time in Eq. (5.17) is taken to infinity, leading to the delta function that picks out the zero frequency component. However, a more accurate treatment would take the upper limit to be $t$ (finite) so that the (now time-dependent) pure dephasing rate also remains finite (it samples a *range* of finite frequencies proportional to $1/t$) at short times, and, at least at those early times, may contribute significantly to the dephasing of coherences. To take account of this, we introduce a time-dependent pure dephasing rate $\Gamma_{pd}(t)$ in place of the vanishing Markovian rates in our Redfield tensor proportional to

$$\Gamma_{pd}(t) \propto \int_0^t dt \int_0^\infty d\omega J(\omega) \coth\left(\frac{\beta\omega}{2}\right) \cos(\omega t). \tag{5.18}$$

The key point is that while $\Gamma_{pd}(t) \to 0$ as $t \to \infty$, the evolution of a coherence $\rho_{12}(t)$ obeying the equation of motion $\dot{\rho}_{12}(t) = -\Gamma_{pd}(t)\rho_{12}(t)$ is [141]

$$\rho_{12}(t) = \rho_{12}(0)e^{-\int_0^t \Gamma_{pd}(t')dt'}, \tag{5.19}$$

and the exponential suppression resulting from the integral over the transient time-dependent rate can be non-negligible. Figure 5.1 illustrates this, showing this suppression factor for the AR background spectral density at $T = 77$ K and $T = 277$ K, taking $\Gamma_{pd}(t)$ to be equal to the right-hand side of Eq. (5.18). Theses curves show a fast initial suppression which then stops and plateaus as the pure dephasing rate vanishes.

The "residual" coherence is suppressed at higher temperature, in line with expectations based on exactly solvable, non-Markovian pure dephasing models which also predict the residual coherence for super-Ohmic spectral densities [141]. Despite the long-time absence of pure-dephasing, Fig. 5.1 clearly demonstrates the importance of accounting for the early time suppression, and naive applications of standard Bloch-Redfield theory for super-Ohmic spectral densities are likely to over-estimate effective coherence times without this correction.
We illustrate this further with Fig. 5.2, which shows $Abs[\rho_{e_1 g}(t)]$ for the full FMO complex computed with and without the super-Ohmic time-dependent pure dephasing. The Bloch-Redfield lifetime of the (lowest exciton energy) $|e_1\rangle$ state at $T = 77$ K is 2.4 ps, implying a very long dephasing time of 4.8 ps in the absence of pure dephasing. This is completely inconsistent with the TEDOPA results in Fig. 5.4 in Section 5.6, while the corrected non-Markovian dephasing result actually gives much better agreement with respect to overall dephasing rates and the long-time value of the coherence. One sees that the dephasing is dominated by the early-time non-Markovian correction, with the much weaker dephasing arising from the relaxation of the $|e_1\rangle$ state leading to a slow decay of the residual coherence plateau.
We note, however, that the inclusion of a time-dependent, non-Markovian pure dephasing rate in our simple time-local master equation is an approximation, and for some spectral densities, the time-local master equation may be invalided. Fortunately, this important, transient pure dephasing effect is handled exactly by TEDOPA, and the results of this section are provided to show the necessity of using advanced techniques for the open-quantum dynamics of PPCs, as well as the improvements to numerically cheaper techniques that insight from TEDOPA can generate.

## 5.5 Fundamental mechanisms supporting long lived coherence

To illustrate the physical mechanism of coherence regeneration through *coherent* (deterministic) motion of discrete modes in excitonic dynamics, we now present semiclassical simulations obtained by treating the coordinates and momenta of the discrete vibrations classically (as explained in the previous session). In the following simulations, interactions with a classical mode of frequency 180cm$^{-1}$ and $S_k = 0.22$ were included and the spectral function Eq. (5.8) used for the background bath. The mode parameters and dephasing rate (1ps$^{-1}$) are taken from hole burning or estimated from fluorescence line narrowing experiments, as is the background spectral function [97, 122, 123]. The background bath and modes are initially in thermal equilibrium at temperature $T$, the background reorganization energy is $\lambda = 35$ cm$^{-1}$ and the seven-chromophore FMO Hamiltonian of Chlorobium tepidum was taken from [97]. We denote the matrix elements $\langle e_n|\rho(t)|e_m\rangle = \rho_{e_n e_m}(t)$.
Figure 5.3 **a** shows results at $T = 77$ K. Motivated by current experimental data [8], which focuses on the two lowest exciton states, we present in Fig. 5.3 (bottom) the coherences $\mathrm{Re}[\rho_{e_1 e_2}(t)]$ between exciton states $(|e_1\rangle, |e_2\rangle)$ with a symmetric superposition of these as the initial state to resemble the laboratory condition after excitation with multiple laser pulses.
In the presence of the 180cm$^{-1}$ modes, which are nearly resonant with $E_1 - E_2 =$ 150cm$^{-1}$, after a transient behaviour in the first 250 fs the coherence exhibits prominent oscillations with an effective coherence time of $\approx 950$ fs.

This is consistent with the coherence times of beating signals observed in FMO experiments [8]. In contrast, for the same background spectral density but neglecting the 180cm$^{-1}$ mode, oscillations decay with a coherence time of just 280 fs after 250 fs. A multi-frequency beating pattern in the oscillations is apparent in the presence of resonant modes until about 850 fs. This is caused by the beating and dynamical coupling between the electronic coherence initially prepared by the laser excitation and the coherence induced later by the discrete mode motion. The vanishing of this pattern at the same rate as the exciton coherence in the background-only simulation provides direct evidence that initial coherences are not protected but *replaced* by mode interactions at later times. Both results also show a fast, time-dependent pure dephasing component at early times due to the background environment.
Figure 5.3 **b** also shows the absolute value of the coherence between $|e_{1,2}\rangle$ and the optical ground state $|g\rangle$, starting from a symmetric superposition of $|e_{1,2}\rangle$ and $|g\rangle$ which closely resembles the evolution probed through accumulated photon echo experiments [142] and recently developed single molecule femtosecond pulse shaping techniques [143]. An additional faster component to the coherence decay is seen for both coherences at early times when the 180cm$^{-1}$ mode is included, but the dynamics are qualitatively similar to the background-only case. The residual, slowly decaying component of $\rho_{e_1 g}$ is due to the relatively long ($\approx$ 2.4 ps) lifetime of the lowest energy state at $T = 77K$ and the absence of pure dephasing in the long time limit in the AR spectral function in the Markov approximation, as detailed in Section 5.4.1.
Figures 5.3 **c** and **d** show corresponding results at $T$ = 277 K. Coherent oscillations lasting up to at least 600 fs have been observed in FMO [8] at this near-ambient temperature. Here we find that the mode interactions lengthen the effective coherence time relative to the background-only simulations even more dramatically, with mode-induced coherence lasting up to 800 fs, compared with just 200 fs in the absence of the mode. The $\rho_{e_{1,2}g}$ coherences all decay with a similar, mono-exponential time constants in the range $80 - 100$ fs, which are dominated by the short (and almost equal) lifetimes and the *transient* pure dephasing rates of the exciton state populations at $T$ = 277 K, as described in Section 5.4.1.

## 5.6 Numerically-exact simulations

The essentially Markovian treatment presented so far to illustrate the principal physical mechanism responsible for long-lived electronic coherences represents an approximation whose validity must be assessed. Therefore we now present numerically exact results which include all possible effects of discrete mode motion, non-adiabatic coupling and fluctuations, as well as the non-Markovian background. For clarity the new physics are presented for a dimer PPC, an important component of a range of natural PPCs [11, 144, 8]. We again consider the same background spectral density $J(\omega)$ and 180cm$^{-1}$ discrete mode of AR [97]. A 37cm$^{-1}$ mode (with $S_k = 0.1$) which has recently been used to describe features of 2D FMO spectra is also included [137], with parameters taken from fluorescence line narrowing experiments [123]. Electronic parameters used in the simulations are $J_{12} = 53.5$cm$^{-1}$, $\epsilon_1 - \epsilon_2 = 130$cm$^{-1}$. This gives two exciton eigenstates with an energy difference of 170cm$^{-1}$, which is based on sites 3 and 4 of the FMO Hamiltonian [97], and which are fairly typical values for exciton pairs in PPCs [97, 7, 8, 9]. The

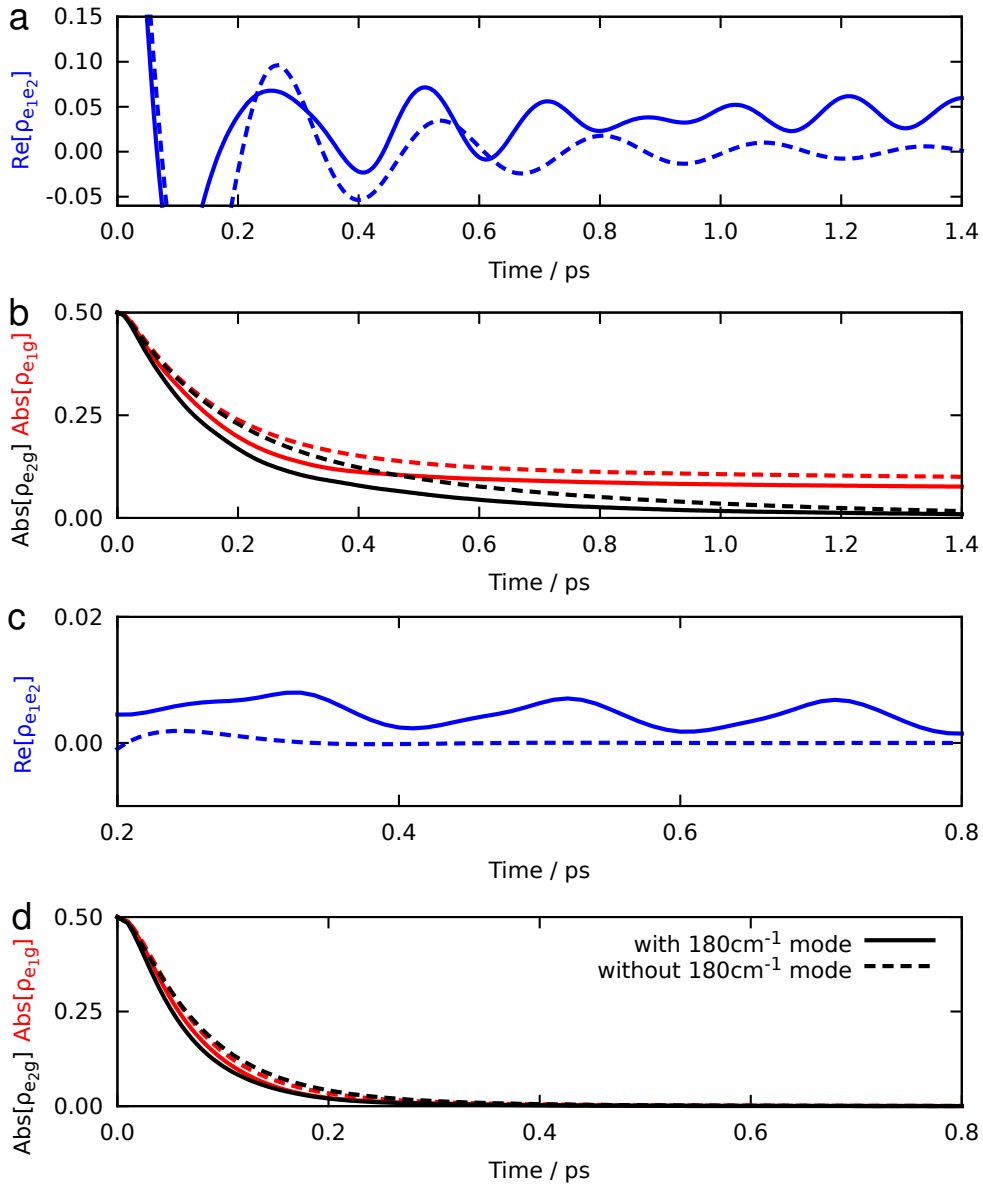


Figure 5.3: In all plots (**a-d**) results including and excluding the resonant 180cm$^{-1}$ mode are shown as full and dashed lines, respectively. **a & b** Semiclassical results at $T = 77$ K. **a** Inter-exciton coherences $\mathrm{Re}[\rho_{e_1e_2}(t)]$ are shown for initial exciton state $2\rho(0) = |e_1\rangle\langle e_1| + |e_2\rangle\langle e_2| + |e_1\rangle\langle e_2| + |e_2\rangle\langle e_1|$. **b**. Ground-excited coherences $\mathrm{Abs}[\rho_{e_1g}(t)]$,$\mathrm{Abs}[\rho_{e_2g}(t)]$ for initial exciton state $2\rho(0) = |e_i\rangle\langle e_i| + |g\rangle\langle g| + |e_i\rangle\langle g| + |g\rangle\langle e_i|$ $(i = 1, 2)$, respectively. Note that the optical high-frequency oscillations of the $\rho_{e_ig}(t)$ coherences have been suppressed by taking the absolute value. Exciton population dynamics following the injection of an excitation on site 1 of the FMO complex were also computed at this temperature, showing that excitons relax to the lowest energy states localised around sites 3 and 4 after $\approx 3$ ps (not shown). This is in line with the experimental transport times of several picoseconds [97]. **c & d** Semiclassical results at $T = 277$ K. The same quantities and initial conditions as **a & b** are plotted and used in **c & d**, respectively. The results at $T = 277$ K in **c & d** are plotted on the interval $[0.2, 0.8]$ ps to highlight the long lived coherences in the presence of the resonant 180cm$^{-1}$ mode on timescale relevant for experiments at this temperature.

evolution of the *global* system-environment density matrix is then computed using the finite-temperature extension of the numerically exact TEDOPA method [5, 6, 69] which was presented in detail in Sections 3.4 and 3.3.5. In all simulations the initial state is a product of an exciton state and a thermal state of the environment (which includes the discrete modes). To show that the main effects arise from the presence of the resonant $180\text{cm}^{-1}$ mode, simulations are carried out both with and without this mode, whilst the non-resonant $37\text{cm}^{-1}$ mode is always retained.

The parameters of the dimer system used throughout are $\epsilon_1 - \epsilon_2 = 130\text{cm}^{-1}$, and $J = 53.5\text{cm}^{-1}$. Diagonalising the dimer Hamiltonian yields two singly-excited exciton states $|e_{1,2}\rangle$ with an energy splitting $E_{12} = E_1 - E_2 = 170\text{cm}^{-1}$. Each constituent of the dimer is linearly coupled to an environment of harmonic oscillators as in the well-known spin-boson model. This problem is then transformed to a physically equivalent setting where each constituent of the dimer is coupled to a linear chain of harmonic oscillators with nearest neighbor interaction [5, 6, 69]. The employed procedure to do so is the one presented in Section 3.4. The initial state of the global system is always taken as $\rho_{total} = \rho(0) \otimes e^{-H_B/k_BT}$ i.e. a product of an arbitrary exciton state and the thermal state of the uncoupled environment at temperature $T$. The initial thermal environment is prepared using imaginary time evolution and the coupling between the system and thermal environment is turned on at time $t = 0$ when the initial thermal state of the environment has been prepared. Hence the problem is now the simulation of the time evolution of this 1-D quantum system. For the present simulations the chains representing the environment are 49 sites long (preventing recurrence effects on the relevant time scale) and are composed of harmonic oscillators truncated to five levels. Using a bond dimension of 100 and 60 (for $77K$ and $277K$ respectively) for the MPS covers all essential physical effects and restricts the required numerical resources to a reasonable limit. The simulations have been carried out using a second order Suzuki-Trotter expansion with time steps of 1/188 and 1/136 of the total time for the imaginary and real time evolution, respectively. These parameters have been adjusted by observation of the norm during the simulation, as to keep the incurred errors due to the truncation of the MPS and the Suzuki-Trotter expansion to a tolerable value.

### 5.6.1 Inter-exciton and ground-exciton coherences

Figure 5.4 **a** shows the evolution of the electronic coherence $\rho_{e_1e_2}(t)$ starting from an initially prepared (pure) symmetric superposition of the exciton states $|e_1\rangle$ and $|e_2\rangle$ at $T = 77$ K. With coupling to the $180\text{cm}^{-1}$ mode, the multi-frequency beating and revival dynamics in the oscillating coherence are seen again, indicating mode-driven coherence. This leads to coherence oscillations with a fast initial dephasing time (200 fs) and a residual, longer lasting component arising from mode driving. Similar revival patterns have been observed in time resolved spectra of FMO [10, 137]. At $T = 277$ K, shown in Fig. 5.4 **c**, the resonant mode also greatly enhances coherent oscillations relative to the background-only coherences over the first 800 fs, which is, again, consistent with experimental results [8]. The non-resonant mode at $37\text{cm}^{-1}$ plays no significant role in these inter-exciton dynamics, as expected.
Fig. 5.4 **b** shows the absolute value of the ground-excited state coherences $\rho_{e_ng}(t)$ at $T = 77$ K for initial symmetric superpositions of states $|e_n\rangle$ and $|g\rangle$. The thermal

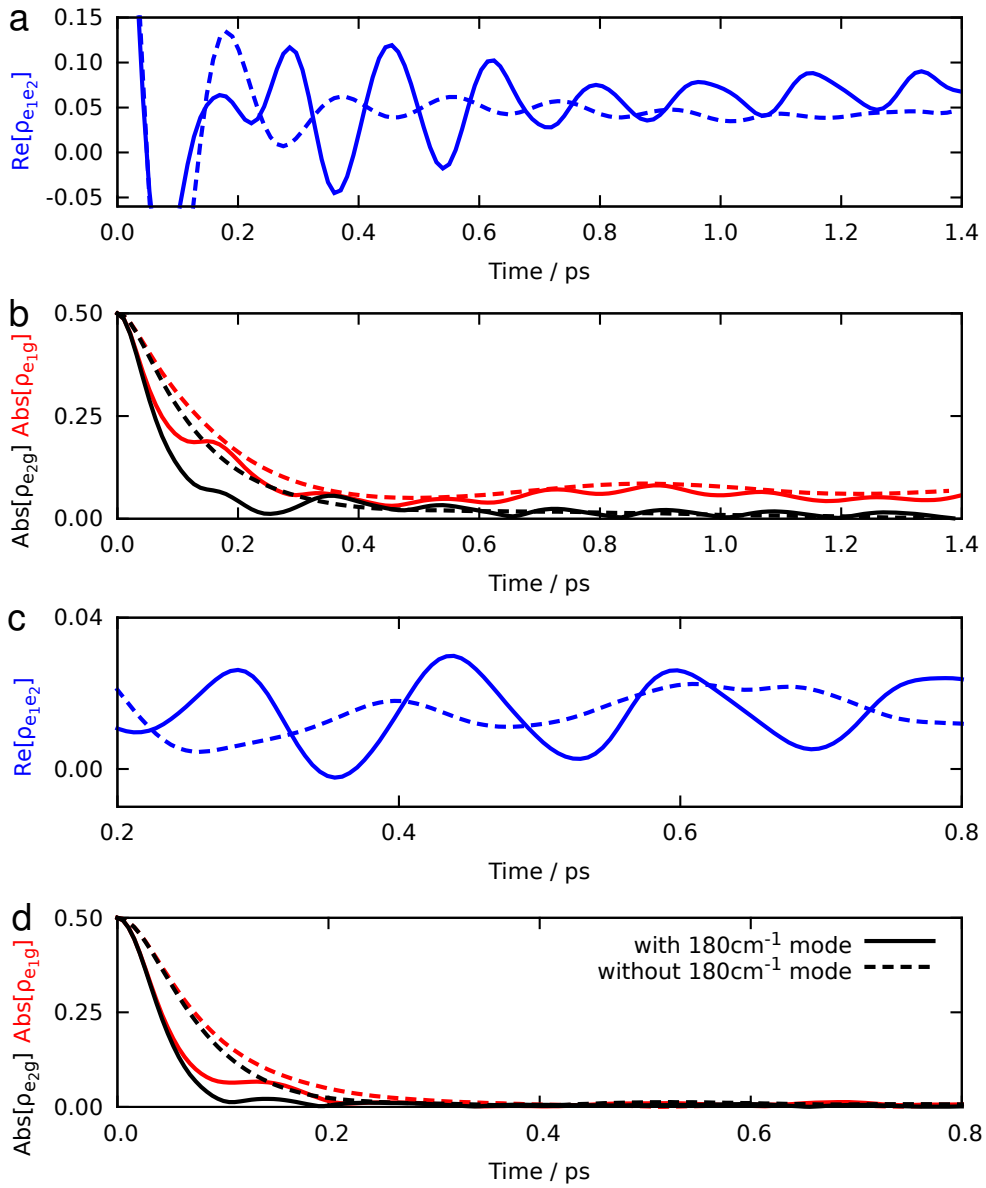


Figure 5.4: In all plots (**a-d**) results including and excluding the resonant 180cm$^{-1}$ mode are shown as full and dashed lines, respectively. **a& b** TEDOPA results at $T = 77$ K. **a**. Inter-exciton coherences $\mathrm{Re}[\rho_{e_1e_2}(t)]$ are shown for initial exciton state $2\rho(0) = |e_1\rangle\langle e_1| + |e_2\rangle\langle e_2| + |e_1\rangle\langle e_2| + |e_2\rangle\langle e_1|$. **b**. Ground-excited coherences $\mathrm{Abs}[\rho_{e_1g}(t)]$,$\mathrm{Abs}[\rho_{e_2g}(t)]$ for initial exciton state$2\rho(0) = |e_i\rangle\langle e_i| + |g\rangle\langle g| + |e_i\rangle\langle g| + |g\rangle\langle e_i|(i = 1, 2)$, respectively. Note that the optical high-frequency oscillations of the $\rho_{e_ig}(t)$ coherences have been suppressed by taking the absolute value. Weak revivals of $\mathrm{Abs}[\rho_{e_2g}(t)]$ (on top of faster amplitude modulations) in the interval $[0.3, 0.6]$ ps arise from coherent population transfer (*against* the energy gradient) and match similar features seen in Fig. 5.5 **a**. **c & d** TEDOPA results at $T = 277$ K. The same quantities and initial conditions as **a & b** are plotted and used in **c & d**, respectively. The results at $T = 277$ K in **c & d** are plotted on the interval [0.2,0.8] ps to highlight the long lived coherences in the presence of the resonant 180cm$^{-1}$ mode on timescale relevant for experiments at this temperature.

and quantum fluctuations of both the 180cm$^{-1}$ and 37cm$^{-1}$ modes induce amplitude modulations of these coherences at the mode frequencies [137], leading to an effectively faster and oscillatory initial decay and then slow oscillations on top of the decaying amplitudes. The short effective time constants for all curves lie in the range $150 - 200$ fs, which are consistent with experimental results [10], and were faster than those found in the semiclassical approach. The coherence $\rho_{e_2g}(t)$ decays through population relaxation from $|e_2\rangle$ to $|e_1\rangle$, however, on top of the periodic modulation caused by modes, additional weak recurrence features result from *oscillatory population transfer* induced by the 180cm$^{-1}$ mode - see Fig. 5.5. The coherence $\rho_{e_1g}(t)$ shows a fast, incomplete and non-Markovian decay ($\approx 150$ fs) initially, and then an extremely slow decay due to the long-time absence of pure dephasing in the AR (super-Ohmic) spectral density and the long ($\approx 2.4$ ps) lifetime of the lowest energy excited state $|e_1\rangle$ at $T = 77$ K. Long $|e_1\rangle\langle g|$ coherence times ($10-100$ ps) have been seen in previous FMO photon echo measurements at low temperatures ($T < 50$ K) [142]. At $T = 277$ K (Fig. 5.4 **d**), both ground-excited coherences decay rapidly due to the fast population relaxation to thermal equilibrium and enhanced pure dephasing. Again, the additional oscillatory decay in the presence of the resonant modes in the TEDOPA simulations leads to significantly faster reduction of coherence (with time constant of 50 fs) compared to the semiclassical approach which neglects the quantum fluctuations of the environment.

### 5.6.2 Population oscillations and environmental variables

For $T = 77$ K, Fig. 5.5 **a** shows the population remaining in $|e_2\rangle$ for the initial state $\rho(0) = |e_2\rangle\langle e_2|$, which does not contain any initial inter-exciton coherence and may be created by incoherent excitation alone. The presence of the 180cm$^{-1}$ mode induces population oscillations in the population decay, which explains the similar oscillations seen in $\rho_{e_1g}(t)$ in Fig. 5.4 **b**, and is also direct evidence of weak coherence transfer (not shown). Population oscillations have also recently been observed in the FMO [145], and imply a partially reversible energy exchange with the "environment" that transiently violates detailed balance. Figure 5.5 **b** shows the spontaneous generation of oscillatory coherences over these population dynamics. Non-Markovian effects (finite reorganization time) and the 37cm$^{-1}$ mode are also seen to generate short-lived spontaneous coherences, however, these are transient and only the 180cm$^{-1}$ mode drives strong long-lasting coherence oscillations. No spontaneous coherence arises in the standard Bloch-Redfield description, as was presented in Section 5.4.1, showing the essential need for going beyond such theories. In Figure 5.5 **c**, we make use of the complete environment information provided by TEDOPA to show the expectation value of the collective environment coordinate $X_1$ [5, 6]. Figure 5.5 **c** shows that the exciton-mode interaction leads to long-lasting coherent environmental oscillations which drive exciton transitions, confirming the semiclassical picture and coherence-generating mechanism previously outlined. In the absence of resonant modes, these strong oscillatory features vanish in the collective mode and exciton populations. Figures 5.5 **d-f** show that, remarkably, the same non-equilibrium and spontaneously coherent dynamics are also present (though less strong) at $T = 277$ K.
We finally observe that the spontaneous coherence in Fig. 5.5 **b** tends to a (small), non-oscillating, non-zero value at long times at $T = 77$ K, indicating that the exciton-mode steady states generated by the dynamics are quantum superpositions of excitonic and vibrational degrees of freedom. Indeed, the prolonged coherent dynamics leading

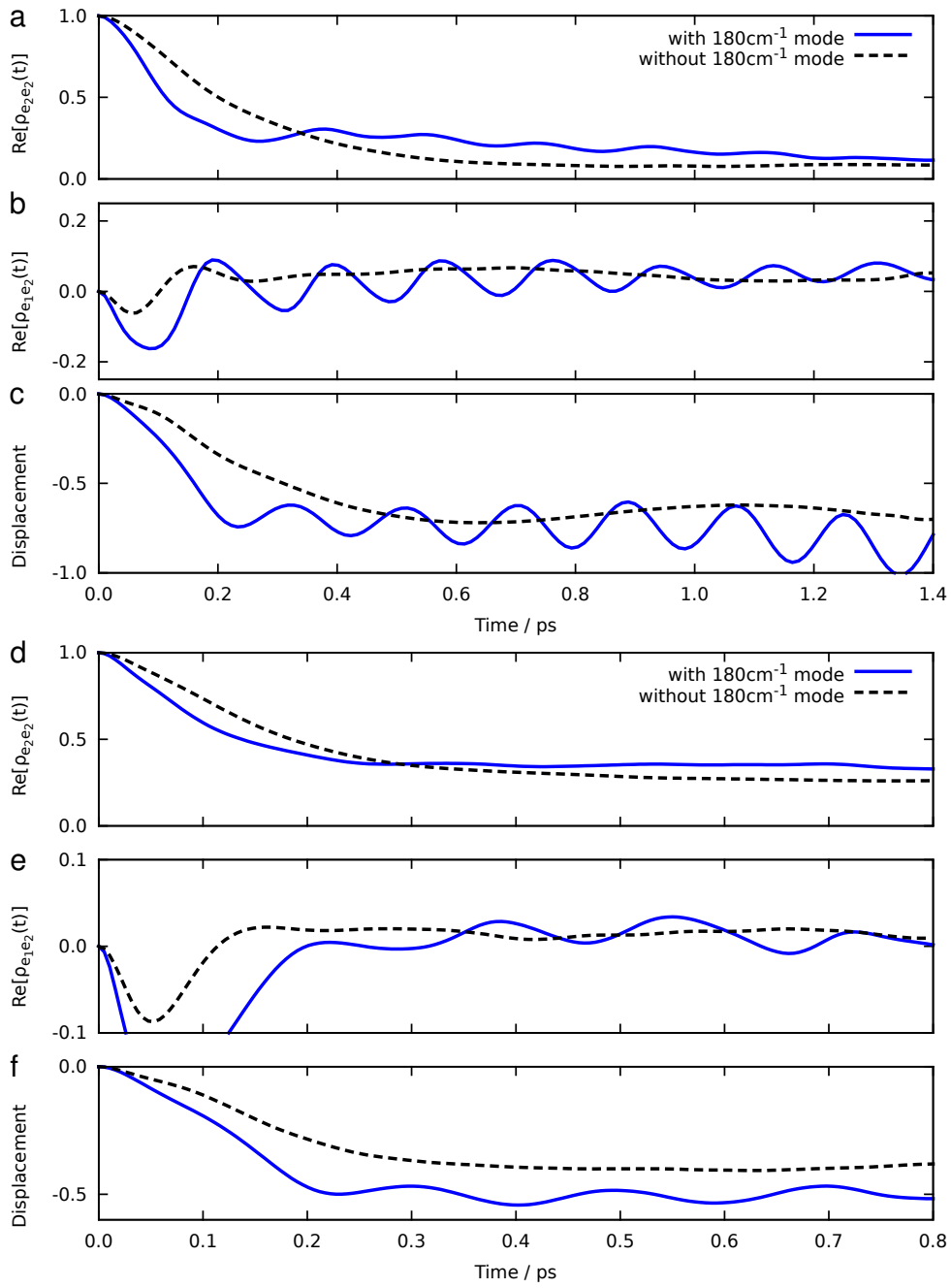


Figure 5.5: **a** Population dynamics, showing $\rho_{e_2e_2}(t)$ for electronic and mode parameters in the text. The initial state is $\rho(0) = |e_2\rangle\langle e_2|$ and environment is at $T = 77$ K. Weak, oscillatory revival of population in the $|e_2\rangle$ state between $0.3-0.6$ ps matches the revival dynamics of $\rho_{e_2g}$ in Fig. 5.4 **b**, indicating coherent population (and coherence) transfer. **b** Spontaneous electronic coherences $Re[\rho_{e_1e_2}(t)]$ for the same parameters and initial conditions. **c** Average displacement $\langle X_1\rangle(t)$ for same parameters an initial conditions. **d-f** The same as **a-c**, respectively, but with the environment initially at $T = 277$ K.

to these steady states could also be looked at in terms of the dynamical hybridization (forming of superposition states) which quantum mechanically mix exciton and (weakly damped) discrete vibrational states. At $T = 277$ K these transient states lead to longer-lasting oscillatory coherence, but the strong dephasing of the background fluctuations prevent these states from being stable in equilibrium. Other examples of how mode interactions may alter the relaxed electronic states are given in Section 5.8, which sets out how discrete modes may provide insight into anomalous oscillations recently observed in conjugated polymers [146, 147].
Our results show that PPCs - as exemplified by the FMO - provide a situation outside of the standard open quantum system paradigm where non-equilibrium processes can compete with the purely dissipative action of the thermal background. The real-time correlations in the exciton-environment state that emerge in this scenario have not yet been explored in great detail, and methods like TEDOPA could be used to look at this new problem in other PPC structures where such conditions could be important and might also drive new, potentially efficient, dynamical phenomena. The experimental verification of the dynamics discussed in this work would provide additional ground for the consolidation of quantum biology as a new, truly multidisciplinary research field with significant implications for the fundamental physics at the border of the quantum and classical domains.

## 5.7 Single system vs. ensemble

In the linear absorption spectra of FMO ensembles, the lowest absorption band – thought to consist of just a single excitonic transition, and possibly some vibrational sidebands [123, 124, 125, 137] – has an inhomogeneous line width of 80cm$^{-1}$ FWHM [123]. This implies an inhomogeneous dephasing time of the $|e_1\rangle\langle g|$ coherences of 130 fs, which is close to the experimental measurements at 77 K [10]. In ensemble 2D spectroscopy experiments, this might completely mask the long (single complex) coherence time of $|e_1\rangle\langle g|$ at $T = 77$ K in Fig. 5.4 **b**, and – moreover – if the inhomogeneous broadening of site energies on each pigment is independent, then signals from *inter-exciton* coherences such as $|e_1\rangle\langle e_2|$ might also dephase on similar timescales due to the resulting width of inter-exciton energy differences [105].
The actual observation of long-lasting inter-exciton coherences in ensemble experiments thus requires further explanation, and could be supported by *correlated inhomogeneous broadening* that preserves energy *differences* between pigments in each complex, or by the dominant contribution of sub-ensembles with resonant exciton-vibration spectra to the oscillatory part of the experimental signals. Both ideas support an interpretation of the experimental quantum beats as arising from *electronic coherence*, with coherence times extended by the mechanisms presented in this article. In addition, the recent theory of Christensson *et al.* also demonstrates that hybridised exciton-vibrational states, which are generated spontaneously during our exact dynamical simulations, might indeed give robust (against inhomogeneous broadening) contributions to the oscillatory part of 2D spectra [138] at $T = 77$ K. Experimental evidence for correlated inhomogeneous broadening has also been observed and discussed in the FMO complex [148, 137].

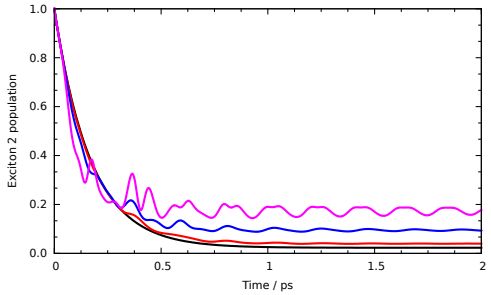


Figure 5.6: Exciton 2 population for initial condition $\rho_{\rm sys}(0) = |e_2\rangle\langle e_2|$ using the semiclassical equations at $T = 77$ K, $t_{vib} = 1$ ps and $S = 0.00, 0.22, 0.50, 1.00$ (black, red, blue, magenta, respectively). Horizontal axis denotes time in ps.

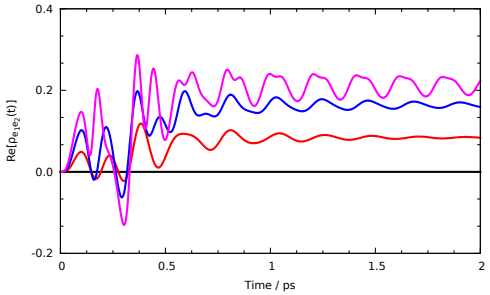


Figure 5.7: Spontaneously generated coherences $\mathrm{Re}[\rho_{e_1e_2}(t)]$ for initial condition $\rho_{\rm sys}(0) = |e_1\rangle\langle e_1|$ using the semiclassical equations at $T = 77$ K, $t_{vib} = 1$ ps and $S = 0.00, 0.22, 0.50, 1.00$ (black, red, blue, magenta curves respectively). Horizontal axis denotes time in ps.

## 5.8 Anomalous anisotropy decay in organic polymers

In a recent paper, Collini and Scholes demonstrated room-temperature inter-exciton coherence in conjugated polymers in chloroform solution [146, 147]. They present some anomalous anisotropy decay data in which long-lasting ($\geq$ 1 ps) coherent oscillations and bi-exponential population transfer in the anisotropy decay were observed [147]. These oscillations had frequencies consistent with vibrational frequencies in the system, but were also rather similar to exciton energy differences as well. The data showed conflicting features (lack of coherence time dependence, long-lasting oscillations) which meant that it was not possible to assign these features unambiguously to either electronic or vibrational coherences. The model and mechanisms presented here may provide some insight into the these data, as they show how the generation of spontaneous coherences by the mode-exciton interaction may induce population oscillations on long time scales even when the exciton system is populated without exciting vibrational coherence. Figure 5.6 shows some illustrative population dynamics obtained using the semiclassical approach of Section 5.4 for a dimer with $\epsilon_1 - \epsilon_2 = 100\mathrm{cm}^{-1}$, $J_{12} = 86\mathrm{cm}^{-1}$, each site of which is coupled to a discrete mode with $\omega_i = 180\mathrm{cm}^{-1}$ and a variable Huang-Rhys factor $S$. The background bath is at zero temperature. Two key features which emerge in the presence of the mode interaction is that the population decay develops a number of new timescales (relative to the case $S_i = 0.0$). The mode leads to a multi-exponential population decay (initially faster when modes are present) on which complex coherent oscillations resulting from the mode interactions are superimposed. These coherent oscillations persist for at least the dephasing time of the modes (1 ps in these simulations), and are stronger and persist longer at stronger coupling.

Figure 5.7 shows the spontaneous generation of the electronic coherence by the discrete modes for the same parameters and initial conditions as in Fig. 5.6. This provides direct evidence that the population oscillations shown in Fig. 5.6 are the result of inter-exciton (electronic) coherences induced by the driving of the discrete modes. The magnitude, oscillation lifetime and final value of these spontaneous coherences increase with coupling

strength, and show interesting dynamical oscillations at very strong coupling, where weak signs of non-rotating wave harmonics can be seen in the driven coherences. The final values show that the discrete modes change the nature of the equilibrium exciton states and both exciton states are significantly hybridised by the modes at strong coupling. Note that these calculation are intended to illustrate the physics which might explain the data of References [146, 147], but the parameters we have chosen are fairly arbitrary and a much more detailed analysis of the physical and experimental set up is required to unambiguously assign a mechanism to the observed behaviour.

# CHAPTER 6

## Phase-dependent exciton transport

In the previous chapter we explored effects that manifest only when going beyond standard theories, such as the Bloch-Redfield description. In the following we again employ TEDOPA on a microscopic model for those PPCs, uncovering and analysing an ultrafast environmental process that causes energy relaxation in the reduced system to depend explicitly on the phase of an initial preparation of eigenstates. Remarkably, for particular phases and system parameters, the net energy flow is uphill, transiently violating the principle of detailed balance, and implying that energy is spontaneously taken up from the environment. The material presented in this chapter is largely based on the accounts of [2].

## 6.1 Motivation

In recent years, new trends have appeared in the field of open quantum system dynamics, particularly in the general area of ultrafast, non-Markovian dynamics and their impact on non-equilibrium quantum thermodynamics. In many cases, this is driven by the prospect of quantum (nano-)technologies, whose optimal operation and efficiency will be determined by such processes. A fascinating test case arose recently, namely the EET in photosynthetic complexes. The observation of long-lasting quantum coherence in a broad range of PPCs has generated tremendous interest in the possible role of quantum effects in exciton transport and charge separation [11, 149, 7, 118, 150, 151, 152], which are often performed with remarkable quantum efficiencies. Early studies of PPCs, such as the FMO complex [153, 154, 110, 119, 97, 155, 156], have already established that a dynamical *interplay* of coherent and dissipative dynamics optimizes targeted exciton transfer. Many subsequent works have developed the theme that *dissipative* quantum dynamics may promote the efficiency of tasks in photosynthetic and other organic light-harvesting materials, with a particular focus on the *complex, structured environments* often found in supra-molecular systems [113, 157, 114, 117, 158, 159, 160].
Motivated by the need to simulate a broad range of systems where the standard approximations such as Born-Markov are unjustifiable, a range of advanced open-system techniques have been developed, some of them already introduced in Section 2.6 [161,

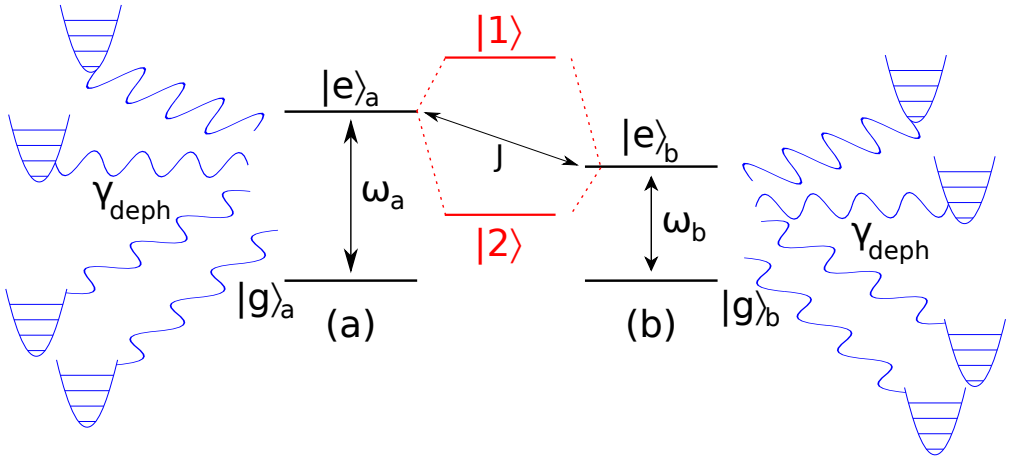


Figure 6.1: Schematic representation of the dimer system. The dynamics in the diagonal (exciton) basis of the system (states $|1\rangle$ and $|2\rangle$ are determined entirely by the action of both transverse (dephasing) and longitudinal (relaxation) environmental processes, the latter only appearing when the eigenstates are delocalised over the sites. In the ultrafast fast regime, these two types of fluctuation may interact, producing (non-secular) effects that are qualitatively different to the standard relaxation and dephasing processes found in secular master equations.

5, 6, 127, 117]. For the treatment of such complex, structured environments as found in PPCs, TEDOPA has established itself as the most powerful method for the evaluation of transient dynamics. Due to its unique ability to track the many-body entangled state of *both* the system and its macroscopic environment, TEDOPA has shed new light into the mechanics of non-equilibrium open dynamics in a range of molecular PPC, solid state and abstract dissipative systems [5, 162, 73].

Here we study a biologically motivated molecular dimer, and again use the finite-temperature TEDOPA (developed in Sections 3.4 and 3.3.5) to explore the dynamics within the correlation (memory) time $\tau$ of the background environment, a regime in which the failure of simple master equation approaches is to be expected.
Most strikingly, we find that the rate and even *direction* of energy transfer becomes dependent on the phase of any prepared superposition of exciton states, essentially allowing certain preparations to extract energy from the non-equilibrium evolution of the environment. With the aid of a Redfield master equation (ME), we pinpoint the physical origin of this effect as the quantum interference of dephasing (transversal) and relaxation (longitudinal) fluctuations becoming comparable to the time-scale of the system dynamics due to an apparent re-scaling of the system-environment coupling. This analysis not only allows us to rationalize the trends seen in the TEDOPA data across the parameter space but in addition demonstrates how the energy harvesting process can occur in a much broader range of open quantum systems. Finally, we suggest how this effect could be observed in biomolecular or artificial devices [152, 149, 150].

## 6.2 Dimer description

Let us begin by describing a model dimer system as composed by two pseudo-spin-1/2 particles (sites), coupled via an exchange interaction of strength $J$, whose Hamiltonian reads $H_{\text{sys}} = \frac{\omega_a}{2}\sigma_z^a + \frac{\omega_b}{2}\sigma_z^b + J\left(\sigma_+^a\sigma_-^b + \sigma_-^a\sigma_+^b\right)$ with **a** and **b** representing each site of the dimer with transition frequency $\omega_{a,b}$ (see Fig. 6.1) and $\sigma$ as the standard Pauli matrices. Each site is subject to the action of a pure dephasing (transversal) local environment that randomises the phases but leaves the populations unaffected. We model the interaction by coupling the system to a continuum of harmonic oscillators $H_{\text{env}} = \sum_i \int_0^\infty dk h_i(k) a_{i,k}^\dagger a_{i,k}$ described for each site $i$ by a set of standard independent bosonic operators $\left[a_k^i, a_l^{j\dagger}\right] = \delta_{k,l}\delta_{i,j}$. The interaction with the dimer is described by the Hamiltonian $H_{\text{int}} = \sum_i \left(\sigma_z^i + \mathbb{1}\right) \int_0^\infty dk g_i(k) \left(a_{i,k} + a_{i,k}^\dagger\right)$. Without loss of generality we will assume that both environments have equal dispersion relation $h(k)$ and coupling strength $g(k)$.

The coherent coupling J leads to the formation of delocalized eigenstates (excitons), whose manifold we restrict to the diagonalization of the one-excitation sector of $H_{\text{sys}}$, spanned by $|e_a g_b\rangle = |e\rangle_a \otimes |g\rangle_b, |g_a e_b\rangle = |g\rangle_a \otimes |e\rangle_b$, justified in this framework by biomolecules usually being under the influence of weak external illumination and/or by doubly excited states being typically strongly suppressed [163]. The exciton energies are then $E_{1,2} = \pm\frac{\omega_0}{2}$ with $\omega_0 = \sqrt{4J^2 + \Delta^2}$, corresponding to the exciton eigenvectors

$$\begin{pmatrix} |1\rangle \\ |2\rangle \end{pmatrix} = \begin{pmatrix} \cos\left(\frac{\theta}{2}\right) & \sin\left(\frac{\theta}{2}\right) \\ -\sin\left(\frac{\theta}{2}\right) & \cos\left(\frac{\theta}{2}\right) \end{pmatrix} \begin{pmatrix} |e_a g_b\rangle \\ |g_a e_b\rangle \end{pmatrix}, \tag{6.1}$$

where $\Delta = \omega_a - \omega_b$ ($\omega_a > \omega_b$), and $\theta$ is the so-called *mixing angle*, defined through the relation $\tan(\theta) = 2J/\Delta$ with $0 \leq \theta \leq \pi/2$.

Using TEDOPA, we study the time evolution of the equal exciton population initial state superposition $\psi = \frac{1}{\sqrt{2}}\left(e^{i\xi}|1\rangle + |2\rangle\right)$. We choose the parameters for the dimer corresponding to those of the two lowest sites in the seven-site FMO Hamiltonian of Chlorobium tepidum as taken from [97, 1], yielding a mixing angle of $\theta \approx \pi/4$.

The parameters chosen for the dimer system in the TEDOPA simulations are $\omega_a = 335\ \text{cm}^{-1}$, $\omega_b = 200\ \text{cm}^{-1}$, and $J = 52\ \text{cm}^{-1}$, yielding a mixing angle of $\theta = \pi/4$. Those parameters correspond to the two lowest site energies and their coupling of the FMO complex [97], those being the spatially closest to the reaction center and thus the most important [1].

Both environments are characterised by the smooth part of the experimentally fitted super-Ohmic spectral function of Adolphs and Renger [97] (AR) for the FMO,

$$J(\omega) = \frac{\lambda\left[1000\omega^5 e^{-\sqrt{\frac{\omega}{\omega_1}}} + 4.3\omega^5 e^{-\sqrt{\frac{\omega}{\omega_2}}}\right]}{9!\left(1000\omega_1^5 + 4.3\omega_2^5\right)} + \sum_{i=1}^{2} g_i\omega_i^2\delta(\omega - \omega_i), \tag{6.2}$$

where the parameters for the continuum part are $\lambda = 35\ \text{cm}^{-1}$ (reorganization energy), $\omega_1 = 0.57\ \text{cm}^{-1}$, and $\omega_2 = 1.9\ \text{cm}^{-1}$ as taken from experimental fitting [97]. The smooth background differs from the standard Drude-Lorentz spectral density in being super-Ohmic, with the high-frequency part of the spectrum responsible for fast thermalization (as required for efficient energy transfer). The vibrational modes are initially in thermal

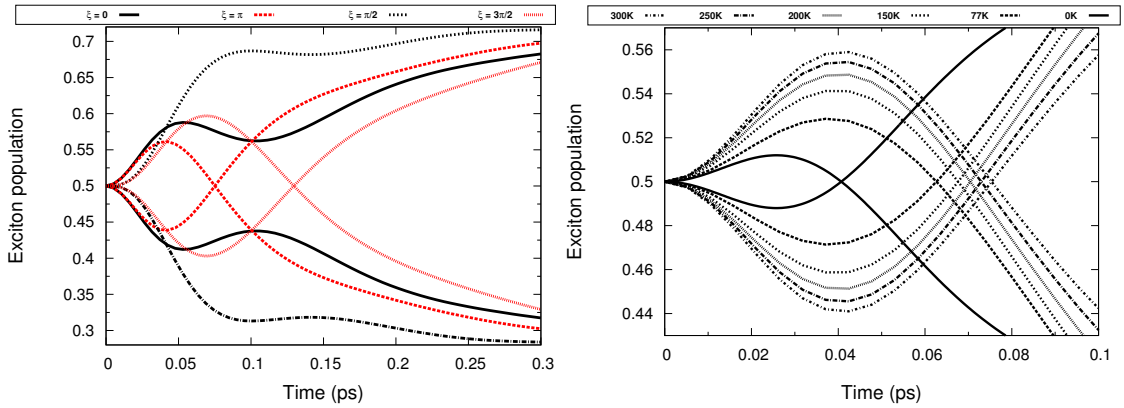


Figure 6.2: Numerical results delivered by TEDOPA for the time evolution of delocalized excitonic populations of a dimer with $\omega_a = 335$ cm$^{-1}$, $\omega_b = 200$ cm$^{-1}$ and $J = 52$ cm$^{-1}$ for representative phases $\xi = 0, \pi/2, \pi, 3\pi/2$ at $T = 277$ K on the left and for temperatures $T = 0 - 300$ K and phase $\xi = \pi$ on the right, both in the super-Ohmic background characterised by the AR spectral density.

equilibrium at temperature $T$. Their parameters are as well motivated experimentally [129, 97], with values $g_1 = 0.12$, $g_2 = 0.22$, $\omega_1 = 180$ cm$^{-1}$, and $\omega_2 = 37$ cm$^{-1}$.
Figure 6.2 on the left shows the time evolution of the excitonic populations at $T = 277$ K for four different initial superposition states with varying phase. We observe that while for an initial phase $\xi = 0$ or $\pi/2$ the system relaxes to the equilibrium state with energy being continuously transferred from the system into the environment, an initial phase of $\xi = \pi$ or $3\pi/2$ differs radically in the early time evolution, with the population of the high energy exciton $|1\rangle$ becoming *greater* (population inversion) than the population of the low energy exciton for $\approx 100$ fs. These results suggest that for a phase chosen on one half of the complex plane, energy flows from the environment into the system at early times, although the subsequent evolution is a relaxation towards a unique equilibrium state.
In Figure 6.2 on the right we set the initial phase to be $\xi = \pi$, ensuring the phase condition for population inversion, and study the behaviour under different temperatures. Interestingly, increasing the temperature enhances the effect, inducing a stronger population inversion and extending the duration of the anomalous dynamics before monotonic (detailed balance) relaxation.

## 6.3 Theoretical analysis

A formal derivation for a ME that ensures evolution under a dynamical semigroup (commonly referred as a Lindblad ME), applied to a non-degenerated system, decouples the evolution of coherences and populations in the energy representation [164]. Therefore it will not capture any initial phase effect on the exciton population dynamics. Moreover, in a Lindblad ME (or a secular Redfield ME) for a two level system, the excitonic populations obey a Pauli ME [165], implying monotonicity in the evolution at all times, thence forbidding a population inversion as observed in Fig. 6.2. Both statements imply that to gain physical insight about the population inversion witnessed by TEDOPA we

need to consider a more general microscopic approach. Here, we work in the Born approximation through the Redfield equation [20, 140] to analyse bath-mediated couplings between populations and coherences. In the exciton basis, we obtain the following time-local ME (details of the derivation as well as explicit expressions for the coefficients are deferred to Section 6.4). Excluding (small) Lamb-shifts, we obtain

$$\begin{aligned}
\dot{\rho}_{11} =& -\Gamma_{rel}(t)\sin^2(\theta)\rho_{11} + \Gamma_{ex}(t)\sin^2(\theta)\rho_{22} \\
&- \frac{1}{2}\sin(2\theta)\left[\Gamma^x_{ns}(t)(\rho_{12}+\rho_{21}) - i\Gamma^y_{ns}(t)(\rho_{12}-\rho_{21})\right] \\
\dot{\rho}_{12} =& -i(E_1-E_2)\rho_{12} - 2\Gamma_d(t)\cos^2(\theta)\rho_{12} + 2\Gamma^+_{nr}(t)\sin^2(\theta)\rho_{21} \\
&- \frac{1}{2}\sin^2(\theta)\left(\Gamma_{rel}(t)\rho_{12} + \Gamma_{ex}(t)\rho_{12}\right) \\
&- \frac{1}{2}\sin(2\theta)\left[\Gamma^x_{ns}(t)(\rho_{11}-\rho_{22}) + i\Gamma^y_{ns}(t)(\rho_{11}-\rho_{22})\right],
\end{aligned} \tag{6.3}$$

with $\dot{\rho}_{22} = -\dot{\rho}_{11}$, $\dot{\rho}_{21} = \dot{\rho}^*_{12}$. This ME contains the standard terms of the secular approximation, namely the pure dephasing term ($\Gamma_{deph}$), spontaneous population relaxation ($\Gamma_{rel}$), and thermal excitation ($\Gamma_{ex}$), which are related by the detailed balance condition $\Gamma_{ex}(t) = e^{-\frac{\omega_0}{kT}}\Gamma_{rel}(t)$. We have retained the time-dependence of all rates (no coarse-graining), as we are interested in the early-time dynamics. In addition to these contributions, the full Redfield ME contains additional terms that couple coherences to populations, and coherences to their complex conjugates. We denote these as non-secular ($\Gamma^{x,y}_{ns}$) and counter-rotating [15] (or rapidly varying [140]) ($\Gamma^{\pm}_{nr}$), respectively. By counter-rotating we understand those $\Gamma$'s that have a time-dependence which oscillates at twice the frequency $\omega_0$ of the excitonic system (these terms would average to zero in a course-grained or rotating-wave approximation) [15]. Non-secular terms have a time-dependence that contains both rotating (slow) *and* counter-rotating (fast) components. The initial preparation $\psi$ imposes $\rho_{12}(0) + \rho_{21}(0) = 2\Re\{\rho_{12}(0)\} = 2\cos(\xi)$ and $\rho_{12}(0) - \rho_{21}(0) = i2\Im\{\rho_{12}(0)\} = i2\sin(\xi)$. Therefore Eqs. (6.3) with the initial condition $\psi$ return $2\dot{\rho}_{11}(0) = -\Gamma_{ns}(0)\sin(2\theta)(\cos(\xi)+\sin(\xi)) - \sin^2(\theta)\,\Gamma_{rel}(t)\left(1-e^{-\omega_0/kT}\right)$. Here we use a Taylor expansion of the decay rates around $t=0$; $\Gamma(t) = \Gamma'(0)\,t + O(0)\,t^2$, where the zeroth order vanishes. Hence the condition for population inversion to occur is

$$-\sin(2\theta)(\cos(\xi)+\sin(\xi)) > \sin^2(\theta)\,\frac{\Gamma_{rel}(0)\left(1-e^{-\frac{\omega_0}{k_BT}}\right)}{\Gamma_{ns}(0)}, \tag{6.4}$$

satisfied if $\dot{\rho}_{11}(0) > 0$.
Whereas if the non-secular terms were absent, $\dot{\rho}_{11}(0) < 0$ and population inversion would never take place. As the right hand side of Eq. (6.4) is always positive, this also holds for the left-hand side for the inversion to occur, imposing an initial phase in the $\xi \in (3\pi/4, 7\pi/4)$ complex half plane, in agreement with the obtained TEDOPA simulation results. Defining the rate of change of energy in the reduced systems as $\Delta E(t) = \omega_0\dot{\rho}_{11}(t)$, we observe that the population inversion requires an initial positive $\Delta E(0)$; consequently there is a net increase of the energy in the system that is being transferred from the non-equilibrium environment. Furthermore, the greater the inequality in Eq. (6.4), the higher the initial rate of change of energy will be, leading to enhanced population inversion. Due to the detailed balance condition on the right-hand side of Eq. (6.4), the exponential increase of the maximum population inversion with

temperature, depicted in Fig. 6.2 on the right, is neatly rationalised by the ME analysis. Finally, we see from Eq. (6.4) that the counter-rotating terms do not place a role in generating the population inversion, and we will not discuss these terms any further.
The reproduction of the main trends observed in the TEDOPA results suggests that a deeper microscopic understanding can be developed by looking at the non-secular terms in Eq. (6.3). In the excitonic basis, all dynamics arise due to environment interactions as given by $H_{\text{int}} = (\cos(\theta)\sigma_z - \sin(\theta)\sigma_x) \otimes (B_k + B_k^\dagger)$ with $B_k$ being some operators characterizing the coupling of the system to the environment. Such coupling $g$, labeled $\gamma_{\text{deph}}$ for each site of the dimer in Fig. 6.1, affects the environmental correlation functions via the relation $\Gamma(t) \propto \langle B_k(t)|B_k(0)\rangle$ [15, 16], and dictates the timescale of the environmental correlation functions understanding it as a rescaled time $\tau = g^2 t$. In the rotated (diagonal) basis that spans the eigenstates of the system (excitons), the coupling to the environment is redefined through $(0, g) \to (g\sin(\theta), g\cos(\theta))$. We now have a longitudinal (relaxation) component in addition to the transversal (dephasing), thence interference amongst them happens, and this is described exactly by these non-secular terms. Likewise, the timescale of such interference changes, meaning that it can become comparable to the time-scale of the system dynamics. In such regimes the non-secular terms can no longer be neglected, as the quantum interference will now be crucial to the understanding the system's dynamics during the correlation time of the environment.
Heuristically, the physical origin of the phase-dependence of transport can be understood by considering the transition amplitudes between the initial state $|\psi\rangle = \frac{1}{\sqrt{2}}\left(e^{i\xi}|1\rangle + |2\rangle\right)$ and the eigenstates $|1\rangle, |2\rangle$. $\langle 1|H_{\text{int}}|\psi\rangle = \frac{1}{\sqrt{2}}\left[\sin(\theta) - e^{i\xi}\cos(\theta)\right] X_{f_{b1}i}$ is yielded by direct calculation, as well as $\langle 2|H_{\text{int}}|\psi\rangle = \frac{1}{\sqrt{2}}\left(\sin(\theta) + e^{i\xi}\cos(\theta)\right) X_{f_{b2}i}$, where the environment matrix element is between initial and final bath configurations. These amplitudes can be understood as arising from two interfering pathways; the amplitude for a flip, say $|1\rangle \to |2\rangle \propto \sin(\theta)$ and the amplitude for no flip, $|2\rangle \to |2\rangle \propto \cos(\theta)e^{i\xi}$. The key observation is that $\xi$ controls whether the interference is constructive or destructive for a given transition (conservation of probability ensures that the other transition is suppressed or enhanced, accordingly). Moreover, the mixing angle $\theta = \pi/4$ maximises the population inversion, corresponding to a maximum interference between the longitudinal and transversal components of the environment, responsible for the non-secular terms via the coupling $\sin(2\theta)$. Completely delocalized ($\theta = \pi/2$) or completely localised ($\theta = 0$) eigenstates lead to no effect on the correlations in the population evolution. The interference flip-noflip pathway is described in the ME approach by the non-secular terms. Those terms do not conserve the energy in the system. The physical framework is thus that of an electronic transition in the system being compensated by the creation/annihilation of a virtual phonon in the environment in a process that drives the environment out of equilibrium, and consequently must vanish on longer timescales, thereby setting the transient nature of the population inversion and ensuring always the relaxation towards a thermal state.
Our toy-model ME analysis demonstrates that the phase-dependent transport uncovered by the TEDOPA results is not a peculiarity of a particular set of parameters but a rather general feature of open quantum systems, with the magnitude of the population inversion sensitive to the environment's spectral function and the mixing angle. Indeed, we can reproduce the qualitative features of the effect observed by TEDOPA employing the Redfield ME. These results, presented in the next section, also show that any violation

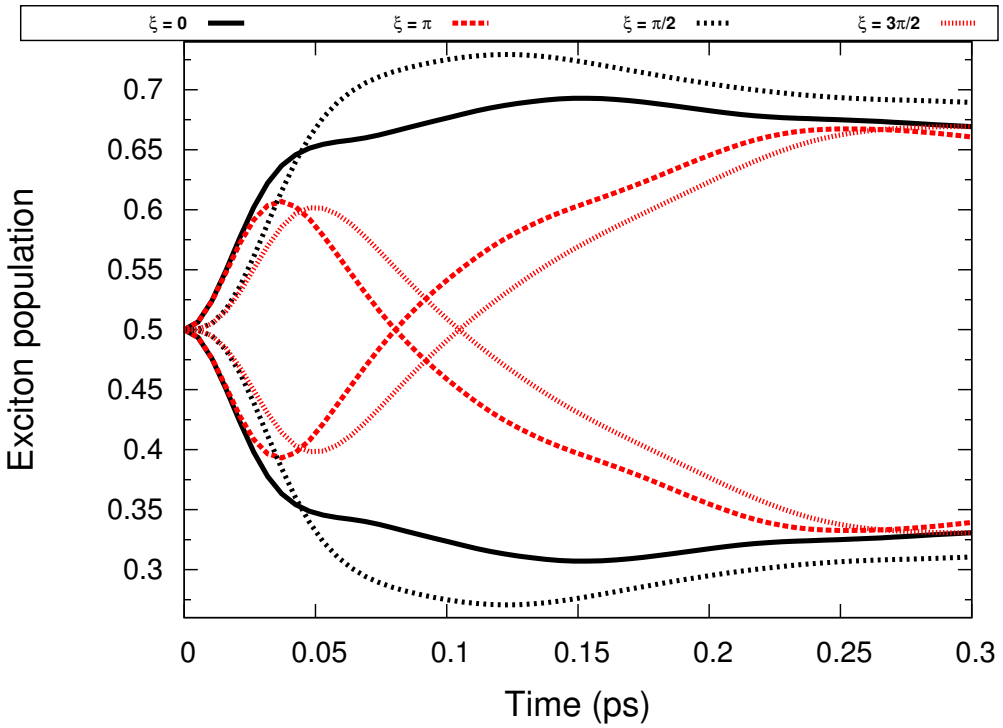


Figure 6.3: TEDOPA numerical results for the time evolution of exciton eigenstate populations on a dimer with $\omega_a = 335$ cm$^{-1}$, $\omega_b = 200$ cm$^{-1}$ and $J = 52$ cm$^{-1}$ in the super-Ohmic background characterized by the AR spectral density with two discrete vibrational modes of frequencies 180 cm$^{-1}$ and 37 cm$^{-1}$ at $T = 277$ K for representative $\xi = 0, \pi/2, \pi, 3\pi/2$ phases.

of positivity (a known problem of equations beyond the Born-Markov approximation [166, 15]) of the reduced density matrix is several orders of magnitude smaller than the population inversion, ensuring that we are not uncovering any unphysical effect. It is important to remember that TEDOPA generates a manifestly positive and numerically exact many-body density matrix, indicating that this effect is real and, potentially, observable.

Returning to the example of PPCs, most realistic spectral functions contain, in addition to the smooth background, a number of sharp features, usually associated with underdamped intramolecular vibrational modes [1, 158, 167, 168, 169, 170, 171]. We tackle this more complicated setting with TEDOPA, and examine the influence of two such modes (one of them near-resonant to the excitonic gap) in the phase-dependent population inversion. Figure 6.3 shows that the maximum inversion is significantly enhanced (up to 20% for $T = 277$ K and $\xi = \pi$ as compared to Fig. 6.2 left side) by the presence of discrete modes. The situation is easily understood via an *exact* quantum mechanical analysis of the system *and* the environment at $t \to 0$. With factorised initial conditions,

the second derivative of the high-energy exciton population at time zero is given by

$$\begin{aligned}\ddot{\rho}_{11}(0) = &-\sin(2\theta)\Re\left\{\rho_{e_1e_2}(0)\right\}\int_0^\infty J_0(\omega)(2n(\omega)+1)d\omega \\ &+\sum_i g_i^2(2n(\omega_i)+1),\end{aligned} \tag{6.5}$$

where $n(\omega)$ is the Planck distribution, $J_0(k)$ is the continuum part of the spectral function $J(\omega)$ and $i$ indexes an arbitrary finite number of intramolecular modes that couple to the system with amplitude $g_i$. As it can also be shown that $\dot{\rho}_{11}(0) = 0$ (see next section), Eq. (6.5) shows that discrete modes will always increase the initial rate of energy flow, explaining the enhancement of the population inversion seen in Fig. 6.3. Interestingly, the analysis shows that the initial enhancement due to discrete modes does not depend on the frequency of the modes, i.e. resonance is not required.

## 6.4 Master equations

### 6.4.1 Derivation

We start with the dimer Hamiltonian, describing a pair of two-level systems (sites **a** and **b**) coherently coupled

$$H_{\text{sys}} = \frac{\omega_a}{2}\sigma_z^a + \frac{\omega_b}{2}e\sigma_z^b + J\left(\sigma_+^a\sigma_-^b + \sigma_-^a\sigma_+^b\right). \tag{6.6}$$

Each of these two-level systems is described by the spin-boson model, thus coupled to an environment modeled by harmonic oscillators, whose Hamiltonian is

$$H_{\text{env}} = \sum_i \int_0^\infty dk g_i(k)\, a_{i,k}^\dagger a_{i,k}. \tag{6.7}$$

with interaction term

$$H_{\text{int}} = \sum_i \left(\sigma_z^i + \mathbb{1}\right)\int_0^\infty dk h_i(k)\left(a_{i,k} + a_{i,k}^\dagger\right). \tag{6.8}$$

We are interested in the time evolution of the diagonal states of $H_{\text{sys}}$, known as exciton states. Moreover, we will ignore excitonic states that correspond to either no excitation on each site ($|g_ag_b\rangle$), or to both sites excited ($|e_ae_b\rangle$), as such states are typically strongly suppressed in the systems of interest [163]. Hence, working on the one-excitation sector, spanned by the states $|e_ag_b\rangle$ and $|g_ae_b\rangle$, the excitons are defined as

$$\begin{pmatrix} |1\rangle \\ |2\rangle \end{pmatrix} = \begin{pmatrix} \cos\left(\frac{\theta}{2}\right) & \sin\left(\frac{\theta}{2}\right) \\ -\sin\left(\frac{\theta}{2}\right) & \cos\left(\frac{\theta}{2}\right) \end{pmatrix}\begin{pmatrix} |e_ag_b\rangle \\ |g_ae_b\rangle \end{pmatrix}, \tag{6.9}$$

with energies $E_{1,2} = \pm\frac{1}{2}\sqrt{4J^2+\Delta^2} = \pm\frac{\omega_0}{2}$, and the definitions $\Delta = \omega_a - \omega_b$ ($\omega_a > \omega_b$) and $\tan(\theta) = 2J/\Delta$. We also redefine the environmental bosonic operators as $a_{p,m} = \frac{1}{\sqrt{2}}(a_a \pm a_b)$, which when we impose the restriction of the one-excitation sector, will

remove the contribution from the $a_p$ operators, thus leaving just one set of harmonic oscillators. The complete Hamiltonian for the dynamics of the exciton states is then

$$H_{\text{sys}} = \frac{1}{2}\omega_0\sigma_z \tag{6.10}$$

$$H_{\text{env}} = \int_0^\infty dk h(k) a_k^\dagger a_k \tag{6.11}$$

$$H_{\text{int}} = (\cos(\theta)\,\sigma_z + \sin(\theta)\,\sigma_x)\int_0^\infty dk g(k)\left(a_k + a_k^\dagger\right), \tag{6.12}$$

where for simplicity we assume a constant of the system to the environment which is equal for both sites.
In order to obtain the master equation, we move to the interaction picture. Assuming a factorized initial state of the form $\rho(t) = \rho_{\text{sys}}(t) \otimes \rho_{\text{env}}$ and working in the Born approximation where the coupling between the system and the environment is presumed weak, the von Neumann equation for the evolution of the density matrix reads (cf. Chapter 2)

$$\dot{\rho}(t) = -\int_0^t dt_1 \text{tr}_{\text{env}}\left([H_{\text{int}}(t), [H_{\text{int}}(t_1), \rho_{\text{sys}}(t) \otimes \rho_{\text{env}}]]\right) \tag{6.13}$$

which is a time-local master equation, also known as the Redfield equation. The interaction Hamiltonian $H_{\text{int}}(t)$ is

$$H_{\text{int}} = [\cos(\theta)\,\sigma_z - \sin(\theta)\,(\cos(\omega_0 t)\,\sigma_x - \sin(\omega_0 t)\,\sigma_y)] \otimes \int_0^\infty dk \left(a_k e^{-i\omega t} + a_k^\dagger e^{i\omega t}\right) \tag{6.14}$$

The following identities are applied in the derivation below,

$$\begin{aligned}
&\sigma_j = \begin{pmatrix} \delta_{jz} & \delta_{jx} - i\delta_{jy} \\ \delta_{jx} + i\delta_{jy} & \delta_{jz} \end{pmatrix} \\
&[\sigma_i, \sigma_j] = 2i\epsilon_{i,j,k}\sigma_k \\
&\{\sigma_i, \sigma_j\} = 2\delta_{i,j}\mathbb{1} \\
&\sigma_x = \sigma_- + \sigma_+\,,\ \sigma_y = i(\sigma_- - \sigma_+)\,,
\end{aligned} \tag{6.15}$$

yielding the time-local master equation

$$\begin{aligned}
\frac{d}{dt}\rho(t) = &-\Gamma_{deph}(t)\cos^2(\theta)\,(\rho(t) - \sigma_z\rho(t)\,\sigma_z) \\
&+ \sin^2(\theta)\left(\Gamma_{nr}^+(t)\,\sigma_+\rho(t)\,\sigma_+ + \Gamma_{nr}^-(t)\,\sigma_-\rho(t)\,\sigma_-\right) \\
&+ \Gamma_{rel}(t)\sin^2(\theta)\left(\sigma_-\rho(t)\,\sigma_+ - \frac{1}{2}\{\sigma_+\sigma_-, \rho(t)\}\right) \\
&+ \Gamma_{ex}(t)\sin^2(\theta)\left(\sigma_+\rho(t)\,\sigma_- - \frac{1}{2}\{\sigma_-\sigma_+, \rho(t)\}\right) \\
&- \frac{1}{2}\sin(2\theta)\Big(\Gamma_{ns}^x(t)\,(\sigma_z\rho(t)\,\sigma_x + \sigma_x\rho(t)\,\sigma_z) \\
&- \Gamma_{ns}^y(t)\,(\sigma_z\rho(t)\,\sigma_y + \sigma_y\rho(t)\,\sigma_z)\Big).
\end{aligned} \tag{6.16}$$

The Lamb shift term is omitted as it is unimportant for the dynamics we are interested in. The expressions for the Γ rates is then

$$\begin{aligned}
\Gamma_{deph}(t) &= 2\int_0^t dt_1 Q(t-t_1),\\
\Gamma^{+}_{nr}(t) &= 2\int_0^t dt_1 e^{i(\omega_0(t+t_1))} Q(t-t_1),\\
\Gamma^{-}_{nr}(t) &= 2\int_0^t dt_1 e^{-i(\omega_0(t+t_1))} Q(t-t_1),\\
\Gamma_{rel}(t) &= 4\int_0^t dt_1 \cos(\omega_0(t-t_1))\, Q(t-t_1),\\
\Gamma_{ex}(t) &= 4\int_0^t dt_1 \cos(\omega_0(t-t_1))\, e^{-\omega_0\beta} Q(t-t_1),\\
\Gamma^{x}_{ns}(t) &= 2\int_0^t dt_1 \cos\left(\frac{\omega_0(t-t_1)}{2}\right)\cos\left(\frac{\omega_0(t+t_1)}{2}\right) Q(t-t_1),\\
\Gamma^{y}_{ns}(t) &= 2\int_0^t dt_1 \sin\left(\frac{\omega_0(t-t_1)}{2}\right)\sin\frac{\omega_0(t+t_1)}{2} Q(t-t_1),
\end{aligned} \tag{6.17}$$

where $Q(t-t_1)$ describes the effect of the environment as

$$Q(t-t_1) = \int_0^\infty d\omega\, J(\omega)\, coth\left(\frac{\beta\omega}{2}\right)\cos(\omega(t-t_1)), \tag{6.18}$$

where $J(\omega)$ describes the distribution of the environmental harmonic oscillators in frequency space, including the coupling $g(k)$ which for most purposes can be considered constant, as $g^2$.

In Figure 6.4 we present exemplary results for the excitonic populations and rate of change of energy, obtained for the master equation from above where we introduce heuristically a decay for the non-rotational and non-secular rates via the time dependent exponential $\exp(-\omega_0 t)$, while for simplicity leaving the rest of the rates equal and constant.

### 6.4.2 Discrete modes

Let us analyze the presence of intra-molecular vibrational modes by performing an exact quantum mechanical calculation, possible at $t = 0$ due to the factorising initial conditions assumption. Starting from the Hamiltonian in the excitonic basis

$$H = \sum_{i=1,2} E_n|n\rangle\langle n| + \sum_{i,k}\omega_k c^\dagger_{i,k}c_{i,k} + \sum_{n,m} Q_{nm}|n\rangle\langle m|, \tag{6.19}$$

we assume a finite number of independent bath modes coupled to each site of the dimer. In the delocalized excitonic basis the system-environment coupling is redefined as $Q_{nm} = \sum_{i,k} g_{i,k} C^i_n C^i_m (c_{i,k} + c^\dagger_{i,k})$, where the coefficients $C$ can be taken as real, so $Q_{nm} = Q_{mn}$. These coefficients can be re-expressed in terms of the mixing angle of the dimer system

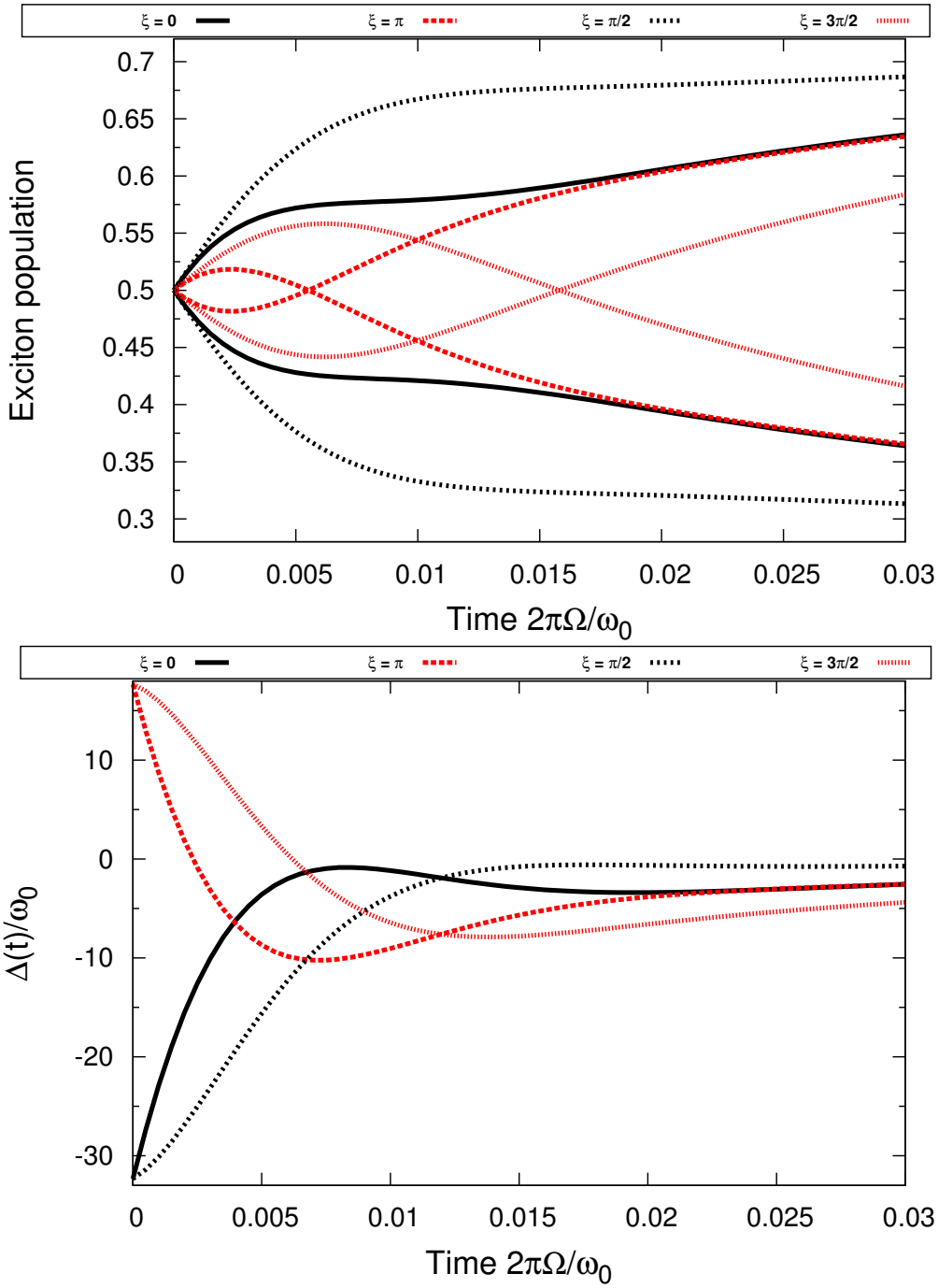


Figure 6.4: (a) Excitonic eigenstate population obtained by numerically solving the ME Eq. (6.16) for representative $\xi = 0, \pi/2, \pi, 3\pi/2$ at $T = 277$ K. Note that the crossing is qualitatively reproduced even in this simple situation. (b) Rate of change of energy $\Delta E(t) = \dot{\rho}_{11}(t)$ for representative $\xi = 0, \pi/2, \pi, 3\pi/2$ at $T = 277$ K, positive the differences when the crossing is present, and always asymptotically going to zero as required by returning to equilibrium.

to obtain explicit expressions for the couplings $Q$, yielding

$$\begin{aligned}
Q_{11} &= \sum_k g_k \cos^2\left(\frac{\theta}{2}\right)\left(c_{1,k} + c_{1,k}^\dagger\right) \\
&\quad + \sum_k g_k \sin^2\left(\frac{\theta}{2}\right)\left(c_{2,k} + c_{2,k}^\dagger\right) \\
Q_{22} &= \sum_k g_k \sin^2\left(\frac{\theta}{2}\right)\left(c_{1,k} + c_{1,k}^\dagger\right) \\
&\quad + \sum_k g_k \cos^2\left(\frac{\theta}{2}\right)\left(c_{2,k} + c_{2,k}^\dagger\right) \\
Q_{12} &= -\frac{1}{2}\sum_k g_k \sin(\theta)\left(c_{1,k} + c_{1,k}^\dagger\right) \\
&\quad + \frac{1}{2}\sum_k g_k \sin(\theta)\left(c_{2,k} + c_{2,k}^\dagger\right).
\end{aligned} \tag{6.20}$$

Introducing the definition $X_k = c_k + c_k^\dagger$ allows us to write

$$\begin{aligned}
Q_{11} - Q_{22} &= \cos(\theta)\sum_k g_k \left(X_{1,k} - X_{2,k}\right) \\
Q_{12} &= -\frac{\sin(\theta)}{2}\sum_k g_k \left(X_{1,k} - X_{2,k}\right).
\end{aligned} \tag{6.21}$$

Now the Heisenberg equations of motion $\dot{O}(t) = -i\left[H, O(t)\right]$ can be used to obtain the equations of motion for the excitonic population and coherence operators as

$$\begin{aligned}
\dot{\rho}_{11}(t) &= -iQ_{12}(t)\left(\rho_{12}(t) - \rho_{21}(t)\right) \\
\dot{\rho}_{12}(t) &= -i\left(E_{12} + Q_{11}(t) - Q_{22}(t)\right)\rho_{12}(t) \\
&\quad - iQ_{12}(t)\left(\rho_{22}(t) - \rho_{11}(t)\right),
\end{aligned} \tag{6.22}$$

Following the analysis from Section 6.3, the influence the initial state's phase on the direction of the energy flow can be extracted. The rate of change of energy is $\Delta(t) = \omega_0\dot{\rho}_{11}(t)$, so the sign of $\rho_{11}(t)$ at $t = 0$ tells in which direction the energy flows after an initial sudden excitation. Thus, taking the second derivative of the higher-energy exciton population evolution equation and inserting the expression from above for the rate of change of coherences, we obtain

$$\ddot{\rho}_{11}(t) = Q_{12}(0)\left(E_{12} + Q_{11}(0) - Q_{22}(0)\right)\Re\left\{\rho_{12}(0)\right\}. \tag{6.23}$$

Assuming separability into electronic and thermal environment density matrices, the expectation of the second derivative of the population with respect to the latter is

$$\ddot{\rho}_{11}(t) = 2\langle Q_{12}(0)\left(Q_{11}(0) - Q_{22}(0)\right)\rangle_\beta \Re\left\{\rho_{12}(0)\right\} \tag{6.24}$$

where the thermal expectation value of the environment operators is

$$\langle Q_{12}(0)\left(Q_{11}(0) - Q_{22}(0)\right)\rangle_\beta = -\frac{1}{2}\sin(2\theta)\sum_k g_k^2(2n(\omega_k) + 1), \tag{6.25}$$

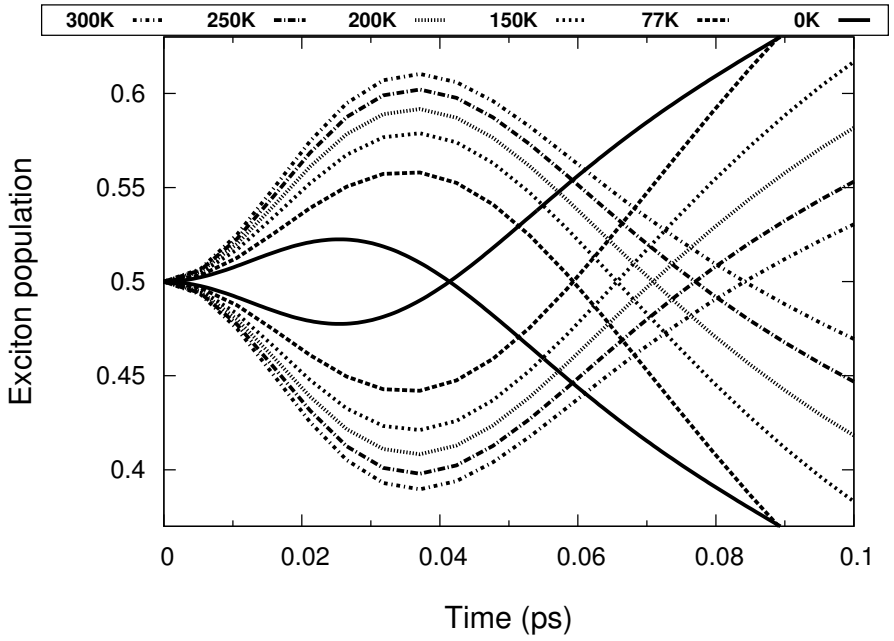


Figure 6.5: TEDOPA results for the time evolution of exciton populations of a dimer with $\omega_a = 335$ cm$^{-1}$, $\omega_b = 200$ cm$^{-1}$, and $J = 52$ cm$^{-1}$ in the presence of two vibrational modes of frequencies 180 cm$^{-1}$ and 37 cm$^{-1}$ for temperatures $0 - 300$ K following the initial state with $\xi = \pi$ in the AR background.

with $n(\omega)$ as the thermal Plank distribution. $\langle Q_{ij}(t)\rangle = 0$ for a thermal state, which is why the first derivative of the populations vanishes as $t \to 0$. We can now combine the previous two equations to obtain

$$\left.\frac{d^2\rho_{11}}{dt^2}\right|_{t=0} = -\sin(2\theta)\,\Re\{\rho_{12}(0)\}\sum_k g_k^2(2n(\omega_k)+1). \tag{6.26}$$

Introducing the definition for the spectral function of the environment as $J(\omega) = \sum_i g_i^2$ $\delta(\omega - \omega_i)$ allows us to write

$$\sum_i g_i^2(2n(\omega_k)+1) = \int_0^\infty J(\omega)\,(2n(\omega)+1)\,d\omega. \tag{6.27}$$

By now choosing the spectral density to contain discrete vibrational modes as $J(\omega) = J_0(\omega) + \sum_i g_i^2\delta(\omega - \omega_i)$, with $J_0(\omega)$ a smooth function representing the background fluctuations and $i$ discrete modes of frequency $\omega_i$ and coupling strength $g_i$, we obtain

$$\begin{aligned}&\sum_k g(k)^2(2n(\omega_k)+1) = \int_0^\infty J(\omega)(2n(\omega)+1)d\omega = \\ &\int_0^\infty J_0(\omega)(2n(\omega)+1)d\omega + \sum_i g_i^2(2n(\omega_i)+1).\end{aligned} \tag{6.28}$$

Putting together this result and the equation for the second derivative of the exciton population, Eq. (6.26), we observe that the presence of discrete modes will always enhance the initial rate of energy flow, whichever its direction.

We recover here the fact that the phase sensitivity is introduced via a correlation of transversal and longitudinal components of the environment ($\langle Q_{12}(0)(Q_{11}(0)-Q_{22}(0))\rangle$) in Eq. (6.26), in complete agreement with the ME approach presented above, where we also obtained the optimal mixing angle as $\theta = \pi/4$, maximizing the effect (overlap) of these cross correlations. In addition, the quantum mechanical analysis, although valid only at $t = 0$, shows that the populations grow quadratically at early times, as obtained by TEDOPA simulations. Such is the expected behaviour for any quantum system, although a Redfield ME due to the first order approximation delivers linear results.

## 6.5 Conclusions

By combining the new, powerful TEDOPA for numerical analysis with theoretical modeling, we have demonstrated that electronic coherence in a dimeric system can not only quantitatively influence the flow of energy transfer over the correlation time of the environment, it may even revert the *direction* of the flow and permit transient energy harvesting from its surroundings. By virtue of the Redfield equation analysis, we were able to predict the electronic and environmental properties that maximize this effect, and also showed that in principle such effects could be found in a wide range of natural dimeric systems. Experimentally, the ultrafast preparation of different excited state coherences could be achieved in a range of solid state systems, such as couple quantum dots, V-systems (via quantum control and optical techniques), and may also be possible in molecular systems prepared in thin films or crystals via polarization control in pump-probe or 2D Fourier transform spectroscopies. Finally, we remark that the fundamental processes we describe strongly motivate the design of thermal energy harvesting in quantum devices. As it is known from classical systems, these transient effects need to ratified in order to be used, which presents a rather interesting theoretical challenge in the context of multi-component, non-equilibrium quantum dynamics.

# CHAPTER 7

# The Transfer Tensor Method and TEDOPA

Until now we introduced the TEDOPA method and applied it in quantum-biological settings. However, TEDOPA is a general-purpose open quantum system method and thus not limited to biological settings but applicable in a wide variety of scenarios. However due to its power and flexibility, simulations tend to be costly – such that in the next two chapters we explore extensions and improvements that allow to save on the associated computational demands. In this chapter we therefore explore additional open quantum system approaches to exploit synergies. The content of this chapter was motivated by [5, 12] is in large parts based on the accounts first given in [3].

## 7.1 Motivation

Recapitulating from Section 3.4, TEDOPA exhibits three main characteristics distinguishing it from other open quantum system methods. First, it does not restrict the ratio $\lambda$ between inner-system couplings and system-environment couplings, unlike several other methods (which assume either $\lambda \gg 1$ or $\lambda \ll 1$). Second, it is able to deal with spectral densities (characterizing the system-environment interaction) that may assume any arbitrary shape. This includes a wide variety of sharp features that may be related to long-lived vibrational modes, as we investigated in Chapter 5. And third, while applicable to all temperatures, due to its scaling properties TEDOPA is inherently well-suited for simulations in the low-temperature domain.

For any exact simulation method it is generally the case that the size of the propagator or of the stochastic sample scales unfavorably with the time length of the simulation or the corresponding perturbative expansion order. Then the question arises whether there are regimes where this scaling can be mitigated in some form, i.e. if an effective propagator of a reduced size can be extracted with the intention of facilitating long-time simulations. In this chapter we address this question by combining TEDOPA with the transfer tensor method (TTM) [12], a tool that quantifies the environment's back-action on the system as in the Nakajima-Zwanzig formalism. The TTM has been shown to provide considerable acceleration in the context of non-Markovian open quantum system

simulations as well as in large classical systems. This is achieved by black-box learning from samples of exact trajectories for some short initial period and subsequent generation of a compact multiplicative propagator for the system degrees of freedom alone. For a learning period longer than the environment correlation time, the propagator accurately reproduces the long-time system dynamics with linear effort. TTM is a general and flexible approach that does not depend on the form of the environment or the interaction, while TEDOPA is not restricted to weak system-environment coupling, high temperatures or specific spectral densities. Therefore, they constitute ideal partners and a study of their combined performance represents a natural research question.

In the following we start by introducing TTM and specify the regime in which its combination with TEDOPA is expected to be most productive. Continuing we provide a benchmark between the proposed combination and the exact result and confirm perfect agreement while highlighting viability and combination synergies. Subsequently, relevant applications of the TEDOPA-TTM combination are proposed which include Ohmic and non-Ohmic spectral densities, low temperature simulations and absorption spectra computations.

## 7.2 Non-Markovian dynamical maps

The starting point for TTM are dynamical maps of a quantum system's evolution [172], containing all possible information of its evolution [25, 24]. As known from quantum process tomography, it is possible to obtain them by adopting a black-box engineering concept [17]. Usually this is done by initializing the system with a complete set of Hilbert space basis states which are also applied as measurements during the time evolution. Performed for the non-Markovian open quantum trajectories using some analytical or numerical method, for an initial condition where the state of the system and the state of the environment are separable, this yields the dynamical maps for discrete times $t_k = k\delta t$ (with step size $\delta t$)

$$\rho\left(t_k\right) = \mathcal{E}\left(t_k\right)\rho\left(0\right). \tag{7.1}$$

Of course this directly identifies the first dynamical map as the identity operator, $\mathcal{E}_0 = \mathbb{1}$. For a time independent Hamiltonian $H$, such as the spin-boson model from Eqs. (3.65) and (3.66) from Section 3.4, this is the solution of the (slightly transformed) time translational invariant Nakajima-Zwanzig equation (2.57)

$$\frac{d}{dt}\rho\left(t\right) = -i\mathcal{L}_s\rho\left(t\right) + \int_0^t dt' \mathcal{K}\left(t-t'\right)\rho\left(t'\right), \tag{7.2}$$

where $\mathcal{L}_s\rho = [H_{\text{sys}}, \rho]$ is the Liouvillian of the system alone, $\mathcal{K}(t-t')$ is the memory kernel arising from the system-environment interaction $H_{\text{int}}$ and $\hbar = 1$.

The key idea is to relate the initial stages of the time evolution to later times by efficiently determining the dynamical correlations built up between system and environment. If the time evolution is Markovian, then the propagation is directly given by the multiplicative application $\mathcal{E}_n = \mathcal{E}_1^n$. Non-Markovianity in the context of TTM is defined by violation of the semigroup property (although different definitions exist [24, 25]). In the

non-Markovian case every dynamical map needs to be found separately and contains correlations of the system at present and at previous times, which renders this an almost impossible task. This is alleviated by transforming dynamical maps for some initial evolution time, containing full information of time correlations, into so-called *transfer tensors* that allow for the propagation of the system in a multiplicative fashion. To create these transfer tensors, TTM used the dynamical maps $\mathcal{E}_k$ as input. The transfer tensors are then iteratively defined by

$$T_n = \mathcal{E}_n - \sum_{m=1}^{n-1} T_{n-m}\mathcal{E}_m. \tag{7.3}$$

According to this definition, the transfer tensor $T_k$ then quantifies the deviation between the dynamical map $\mathcal{E}_k$ and the non-Markovian effects built up during the previous $k-1$ time steps.

An inherent and clear justification for the use of transfer tensors is given by their actual relation to physical properties via

$$T_{k,n} = (\mathbb{1} - i\mathcal{L}_s\delta t)\,\delta_{k,n+1} + \mathcal{K}_{k,n}\delta t^2. \tag{7.4}$$

Thus the discretization of the memory kernel $\mathcal{K}$ is directly related to these tensors by the time step $\delta t$

$$T_k = \mathcal{K}_k\delta t^2, \tag{7.5}$$

where $\mathcal{K}_k = \mathcal{K}(t_k)$ is the discretized memory kernel at time $t_k$. Additionally the transfer tensors directly relate to the system's Liouville operator $\mathcal{L}_s$. On an operational level this very useful property allows checking of the tensor's correctness by extracting and comparing the Hamiltonian, since

$$T_1 = (\mathbb{1} - i\mathcal{L}_s\delta t) \tag{7.6}$$

$$\mathcal{L}_s = -i\,(\mathbb{1} - T_1)\,/\delta t. \tag{7.7}$$

These tensors can be used to propagate the system to arbitrary later times as long as they cover a relevant part of the memory kernel. Assuming a finite coherence time of the environment $t_{\mathrm{coh}}$, the transfer tensors will decay sufficiently fast that a cutoff $K$ can be defined such that $T_k = 0$ for $k > K$. Then, $\rho(t_n)$ for $n > K$ can be expressed simply as

$$\rho(t_n) = \sum_{k=1}^{K} T_k\rho(t_{n-k}). \tag{7.8}$$

TTM is applicable in a variety of interesting cases, scaling favourably in system size and length of the environment's correlation time. Due to its nature it also does not rely on assumptions on the system's parameters or environmental couplings. Thus it is usable as a powerful black-box tool which, given initial trajectories, subsequently delivers the evolution trajectories for later times. For details exceeding the present account refer to the detailed introduction given in [12].

## 7.3 Synergies

The combination of both TEDOPA and TTM facilitates the simulation of open quantum systems in regimes that were previously inaccessible. Exceptionally relevant is the ability to perform long-time simulations of low-temperature, highly-structured harmonic environments at merely a fraction of the computational cost which would be necessary if only TEDOPA were applied. Evidence for this is provided by simple examination of some of the features of each of the methods. On the one hand, TEDOPA is based on an MPO description of the complete system plus environment density matrix. Settings leading to low occupation numbers of environmental oscillators – such as low temperatures – are especially suitable as they reduce the MPO's number and size. In addition TEDOPA is not limited to a specific analytical form of the spectral density. On the other hand, recurrence effects originating at the chain's boundary limit the time for which accurate simulation is possible. Because TTM only requires sample system trajectories for as long as bath correlations are present, the required chain length is then not anymore determined by the target simulation time. The combination of TTM and TEDOPA is therefore most useful in highly non-Markovian regimes where bath correlation times are comparable to the maximum simulation time that TEDOPA can reach before recurrences appear.

## 7.4 Parameters and accuracy

Let us analyse relevant parametric cutoffs for the control of the accuracy of numerical simulations that combine TEDOPA and TTM. In the case of TEDOPA one can distinguish between parameters related to the chain mapping and to the MPO propagation. The semi-infinite chain of oscillators generated by the mapping necessarily requires the truncation of both the chain length $N$ and the Hilbert space dimension $d$ for each oscillator at a reasonable value. Those are native TEDOPA error sources and they have a direct effect on the recurrence time of the simulation and the maximum temperature that may be simulated, respectively – see also Section 3.4. The effect of other relevant parameters, namely the MPO's matrix size ($\chi \times \chi$) and the time step $\delta t$, are already well-known from TEBD and analysed thoroughly in Section 3.3.7. To reach the accuracy required by TTM, care needs to be taken in adjusting these parameters to bound the total error of TEDOPA sufficiently. Some indications on how to accomplish this are provided in the present section.

The maximum time $t_{\max}$ before unphysical back-actions of the environment due to reflections at the end of the chain appear is related to the chain length $N$. Usually all chain coefficients are of the same order of magnitude and hence the simulation time $t_{\max}$ scales roughly linearly with $N$. This reveals one of the benefits of the application of TTM on TEDOPA: The chain length can be truncated according to the length of the bath correlation time, allocating the simulation resources properly and shortening simulation times considerably in many cases of relevance (cf. Fig. 7.9). The exact relationship between $N$ and $t_{\max}$ may be derived analytically through the use of Lieb-Robinson bounds [71] or numerically by trial-and-error. By setting the chain in an initial state $|10\ldots0\rangle$ and following the evolution of the operator $O = n\mathbb{1}\ldots\mathbb{1}$ until a recurrence occurs.

The second native TEDOPA parameter is the local dimension $d$ of the single oscillators constituting the environment. For a given temperature the occupation of the single oscillators can be determined exactly, giving a rough scale of the necessary truncation level. Some error will be introduced nevertheless, but this can be upper-bounded analytically as explained in Ref. [71]. On the other hand, numerical benchmark calculations with increasing local dimensions will generally yield sufficiently accurate results.

A further subtlety of the chain mapping consists in the determination of the cutoff frequency $\omega_c$ of the spectral density. For instance, the asymptotic convergence to zero for large frequencies of the Drude-Lorentz environment imposes a careful convergence check of the resulting physical behaviour. For further discussions of these effects refer to [70].

While some error sources (like the cutoff in the chain length) introduce, if treated correctly, virtually no error at all, the matrix size $\chi$ necessarily does so due to the nature of the MPO. However, as already studied in the context of the TEBD algorithm in Section 3.3.7, this error can be monitored during the time evolution. This results in a quantity very similar to the *discarded weight* known from DMRG

$$w_{\text{discarded}} = 1 - \sum_i \sigma_i^2. \tag{7.9}$$

Using the discarded singular values $\sigma_i$, this quantifies the deviation from the targeted state. The error propagates in a non-trivial fashion and it is advisable to perform convergence checks in the dynamics under variation of the size of $\chi$. An additional source of error is derived from the Suzuki-Trotter decomposition used in the TEBD part of TEDOPA, quantified in Section 3.3.7.
It should be noted that the magnitude of the singular values kept during MPO-procedure should not fall below some threshold $w_{\text{thresh}}$. The transfer tensors determined by TTM do decay rapidly, falling to comparatively low magnitudes, and singular values corrupted by numerical noise deteriorate the interpretation of results as well as the propagation procedure.

Finally, in the scope of TTM, the important quantity to keep track of in simulations is the norm of the memory kernel. This corresponds to the norm of the transfer tensors divided by the squared time step $\delta t$. This magnitude should exhibit a sufficiently fast decay so that the remaining tail can be neglected. Additionally, the time step $\delta t$ must be such that it provides a good resolution of the features of the memory kernel.

## 7.5 Benchmark

Here we verify the combination of TEDOPA with TTM by comparing the obtained transfer tensors with those originating from another numerically exact simulation method for non-Markovian systems under the same conditions. The chosen benchmark regime is the Ohmic Drude-Lorentz environment and the additional simulation method is HEOM, which we already encountered in Section 2.6.
We consider the spin-boson model and define the system Hamiltonian

$$H_{\text{sys}} = \frac{1}{2}\varepsilon\sigma_z + \frac{1}{2}\Delta\sigma_x. \tag{7.10}$$

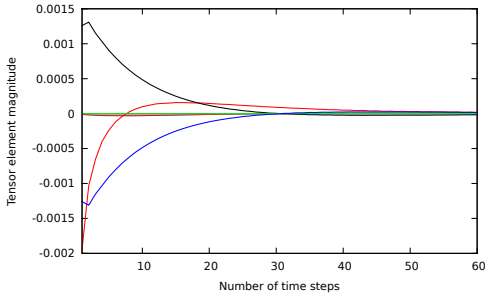


Figure 7.1: The decay of the memory kernel's elements (separated into real and imaginary part) for the initial part of the time evolution as obtained by TEDOPA. The system is subject to an environment with the Drude-Lorentz spectral density. System and environment parameters are as presented in the main text.

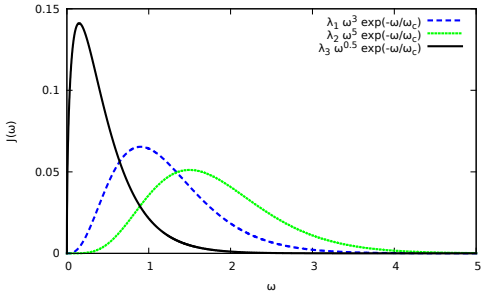


Figure 7.2: Plot of $J_{1,2,3}$. They differ only in their functional behaviour; their reorganization energy is kept constant at $\lambda_r = 0.29577$. To ensure this condition, their coupling constants have been chosen as $\lambda_{1,2,3} = 1.8, 1.0, 0.6$. They exhibit the same decay behaviour with soft and hard cutoff $\omega_c = 0.3$ and $\omega_{hc} = 10.0$, respectively.

Here we set $\hbar = 1$, a convention we will stick to from now on. We employ the standard spin-boson notation where $\varepsilon$ corresponds to the energy bias between ground and excited state, $\Delta$ is the tunneling matrix element, and $\sigma_i$ $(i = x, y, z)$ are the Pauli matrices corresponding to the $i$'th spatial direction. The system interaction operator $A$ is defined as the excited state projector $|e\rangle\langle e|$. We choose the parameters $\varepsilon = 1$ and $\Delta = 0.6$, and an Ohmic spectral density of the Drude-Lorentz form

$$J(\omega) = \lambda\, \gamma\, \frac{\omega}{(\omega^2 + \gamma^2)}, \tag{7.11}$$

with parameters $\lambda = 1$ and $\gamma = 10$ respectively identifying a scaling of the interaction strength and a soft cutoff frequency. Thus the bath's reorganization energy $\lambda_r = \int J(\omega)\, d\omega$ is $\lambda_r = 5.89$. A large hard cutoff $\omega_{\mathrm{hc}} = 320$ has been employed to meet the aforementioned convergence requirements of TEDOPA under Drude-Lorentz environments.

At an inverse temperature of $\beta = 0.5$, TEDOPA exhibits favorable cutoffs and HEOM simulations are accurate, which enables benchmarking. The resulting elements of the memory kernel obtained by TTM applied to TEDOPA's initial trajectories are compared with those retrieved from HEOM simulations of the same system. We have confirmed agreement in a broad range of additional regimes accessible to both TEDOPA and HEOM. The retrieved elements of the memory kernel, as obtained by TEDOPA, are shown in Fig. 7.1. Further the system's Hamiltonian has successfully been recovered from the first transfer tensor. This also corroborates the ability of TTM to extract the same dynamical tensors irrespective of the simulation method used for the generation of the trajectories. We will now turn to applications on hitherto inaccessible regimes to illustrate the strengths of the TEDOPA-TTM combination.

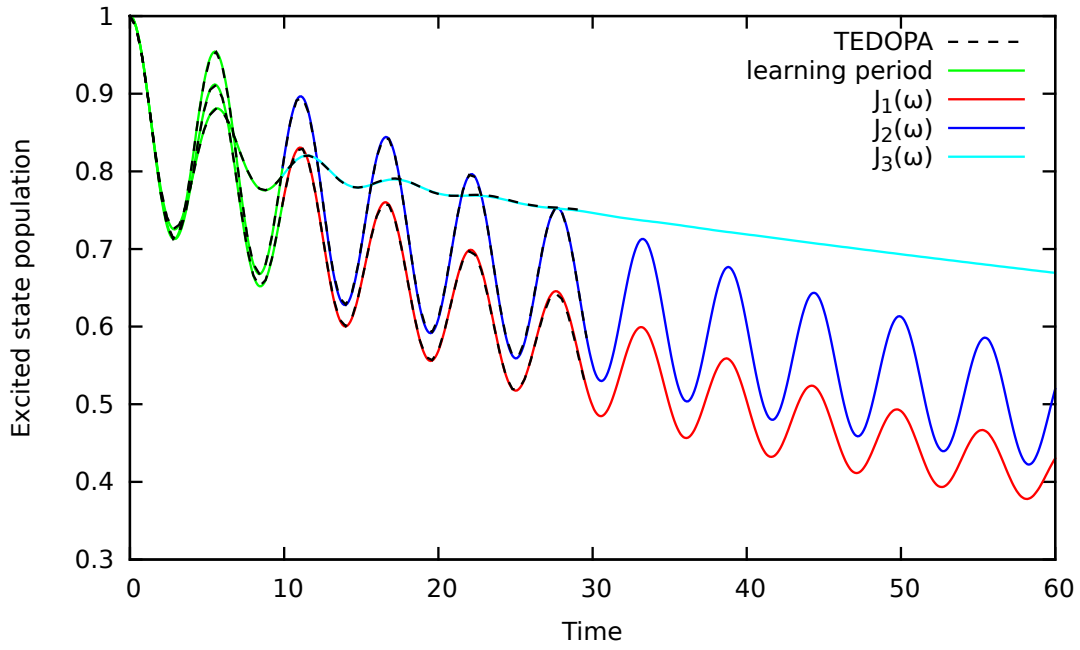


Figure 7.3: Effect on the dynamics of three different spectral densities $J_{1,2,3}$ at inverse temperature $\beta = 1.0$ and verification of the predictability of trajectories by TTM. Black dashed lines are TEDOPA simulation results, colored lines are TTM's predictions; TTM learning times are denoted by green lines (roughly until $t = 10$).

## 7.6 Applications

### 7.6.1 Non-Ohmic spectra

By construction, TEDOPA is inherently suited to treat spectral densities of any shape. When considering non-Ohmic spectral densities, Markovian approaches are well-known to anomalously omit pure dephasing terms [141]. In this section we present the analysis of the dynamical effects of three different non-Ohmic spectral densities

$$J_1(\omega) = \lambda_1 \, \omega^3 \, e^{-\omega/\omega_c}, \tag{7.12}$$

$$J_2(\omega) = \lambda_2 \, \omega^5 \, e^{-\omega/\omega_c}, \tag{7.13}$$

$$J_3(\omega) = \lambda_3 \, \sqrt{\omega} \, e^{-\omega/\omega_c}. \tag{7.14}$$

To facilitate comparison, all of them exhibit the same exponential decay with $\omega_c = 0.3$ and are subject to a hard cutoff at $\omega_{hc} = 10$. Also the parameters $\lambda_1 = 1.8$, $\lambda_2 = 1.0$ and $\lambda_3 = 0.6$ have been chosen in such a way that the reorganization energy $\lambda_r = 0.3$ is the same for each of these spectral densities. Thus the average interaction strength between system and environment is the same and the functional form of the spectral density is the factor responsible for disparate dynamics. The resulting dissimilar amplitudes and decay rates of the oscillations due to the different spectral densities are illustrated in Fig. 7.3. The system parameters are $\varepsilon = 1.0$ and $\Delta = 0.6$. One can observe that, for the fastest environment $J_2$, oscillations are sustained for a longer time, while this ability

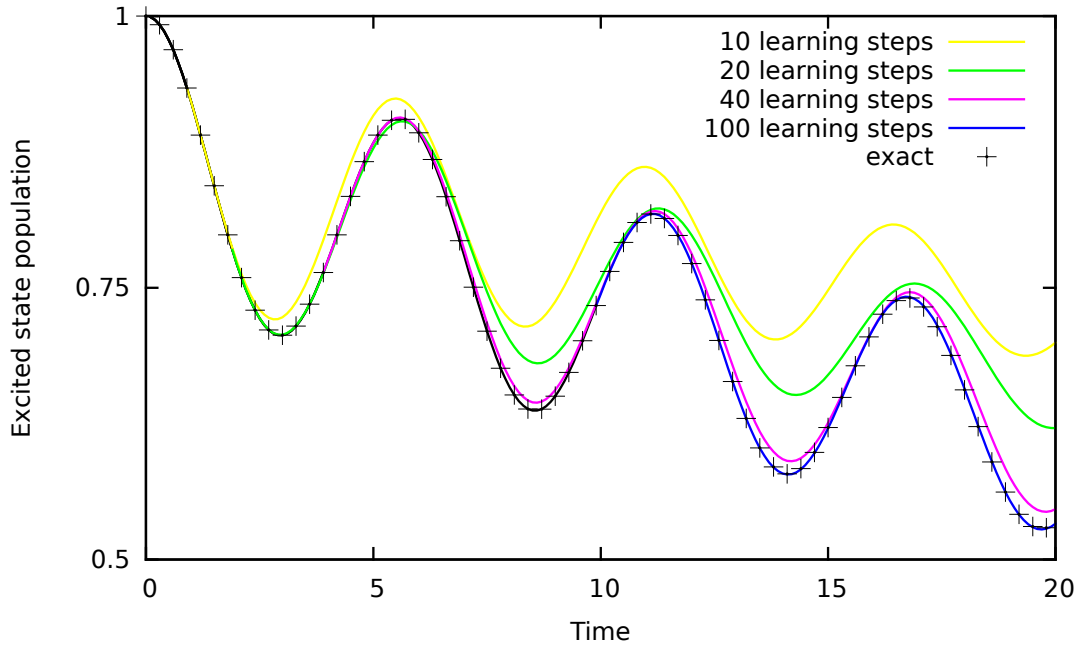


Figure 7.4: Time evolution of the excited state population, subject to an environment with spectral density $J_2(\omega)$ at $\beta = 1.0$. Black crosses denote the TEDOPA-only evolution, while the TTM predictions (colored lines) show a gradual convergence upon increased learning time (the initial part of each curve, marked in black in the plot). The full 100 learning steps correspond to time $t = 10$.

decreases for spectral densities centered in lower frequencies $J_1$ and almost disappears for the very slow environment represented by $J_3$. Some brief initial time is sufficient to learn TTM and predict the further evolution, whereupon high-accuracy TEDOPA simulations are used to verify these predictions. The suitability of the TEDOPA-TTM combination is supported by the fact that these simulations require on the order of just 100 tensors to converge to the exact results that have been obtained by high-accuracy TEDOPA simulations, as shown in Fig. 7.4. This translates into about an order of magnitude faster results for TTM-TEDOPA combination than for TEDOPA alone. Further improvements in simulation speed are possible and are discussed in section 7.7.

### 7.6.2 Low temperatures

To further illustrate the power of our approach, we present results for a broad range of low to very low temperatures. For the super-Ohmic spectral density $J_2(\omega)$ we show that it is possible to simulate the dynamics of a monomeric system at various inverse temperatures ranging from $\beta = 0.1$ to $\beta = 10$. This holds for the same system parameters as in the previous example. For the case of spectral density $J_1(\omega)$ we employ TTM to propagate the system until the steady state is reached (Fig. 7.6) and plot the steady-state occupation of the excited state for various inverse temperatures $\beta$ in Fig. 7.7. The insets in Figs. 7.5 and 7.6 show the memory kernel's decay over several orders of magnitude for the corresponding spectral densities. It is this decay which certifies the possibility to

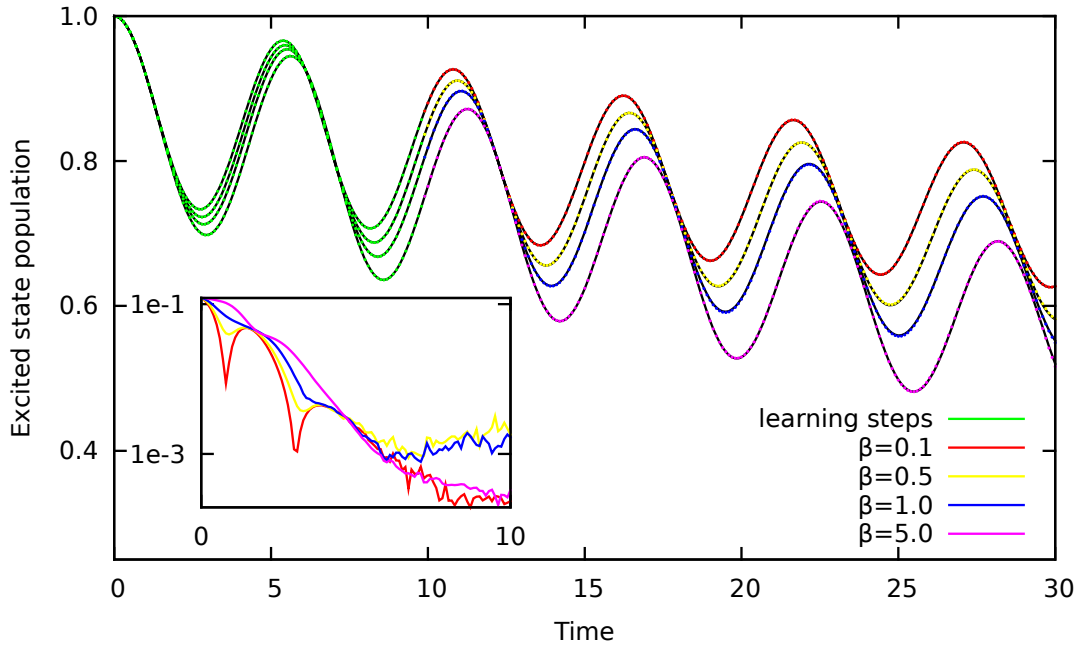


Figure 7.5: Decay of a monomeric system's population, subject to an environment with spectral density $J_2(\omega)$ at different inverse temperatures $\beta$. For better clarity only the first couple of oscillations are shown. Solid lines correspond to TEDOPA-only simulations with verified accuracy. The green initial part of each curve corresponds to the learning period. The decay of the tensor norm for the learning period is shown in the inset.

use the tensors for long-time propagation of the dynamics.

### 7.6.3 Absorption spectrum

The combination of TEDOPA and TTM is especially fruitful for applications where accurate simulation of long-time dynamics is crucial. The determination of absorption spectra belongs to this class of problems and we analyse here the more complex case of a dimeric system consisting of two coupled monomers.
The coupled dimeric system in the single excitation manifold consists of two excited states $|e_1\rangle$, $|e_2\rangle$ and a common ground state $|g\rangle$, and is described by the Hamiltonian

$$H_{sys} = \varepsilon_1 |e_1\rangle\langle e_1| + \varepsilon_2 |e_2\rangle\langle e_2| + J\left(|e_1\rangle\langle e_2| + |e_2\rangle\langle e_1|\right), \tag{7.15}$$

where parameters $\varepsilon_1 = 1.0$, $\varepsilon_2 = 2.0$, and exchange interaction strength $J = 0.6$ are chosen. Each of the two systems is coupled to an environment. Without loss of generality we assume both environments are described by the same spectral density $J_1(\omega)$ and at temperature $\beta = 1.0$.
The absorption spectrum is calculated as the Fourier transform of the two-point corre-

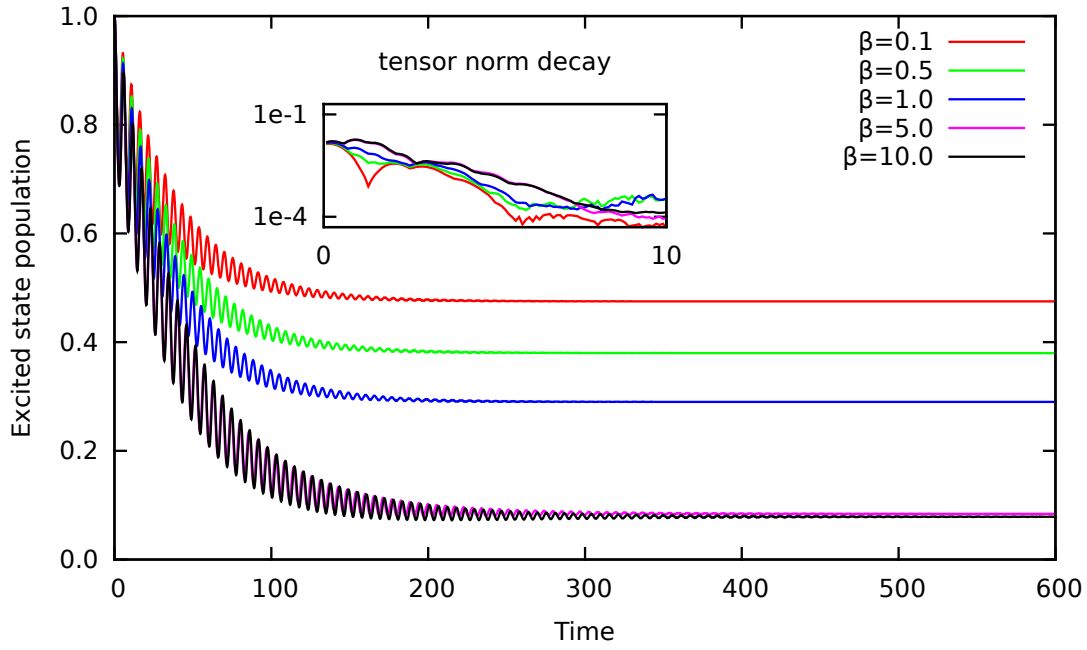


Figure 7.6: Thermalization of the system's population, subject to an environment with spectral density $J_1(\omega)$ at different temperatures. Solid lines correspond to TEDOPA-only simulations with verified accuracy. The green initial part of each curve corresponds to the learning period. The decay of the tensor norm for the learning period is shown in the inset.

lation function of the dipole operator $\hat{\mu} = \mu_1|e_1\rangle\langle g| + \mu_2|e_2\rangle\langle g| + h.c.$

$$C_{\mu-\mu}(t,0) = \mathrm{tr}\left[\hat{\mu}(t)\,\hat{\mu}(0)\right] \tag{7.16}$$

$$= \mathrm{tr}\left[e^{-iHt}\hat{\mu}e^{iHt}\hat{\mu}\rho(0)\right], \tag{7.17}$$

between times $t = 0$ and $t = \tau$ such that the steady state has been reached at $\tau$.

In the limit of weak interaction with the environment, the absorption spectrum emerging from Hamiltonian Eq.(7.15) exhibits two peaks in the one-exciton subspace. One of them is shown in the $\lambda_1 = 0.018$ line (green) of Figure 7.8, corresponding to the second excited state in the excitonic manifold at a wavelength of around 0.363. For higher coupling strengths to the environment, the emergence of the vibrational fine structure splits the peak in two, which is shown in the $\lambda_1 = 0.18$ line (blue) and the $\lambda_1 = 1.8$ line (black).

## 7.7 Simulation time

The ability of the TEDOPA-TTM combination to explore new simulation regimes is a consequence of the extraordinary savings in computational resources. We will explore these in terms of the "wall time" $t_w$, the physical time required for the simulation to be executed as measured by an external clock.
Three factors have a direct influence on simulation time:

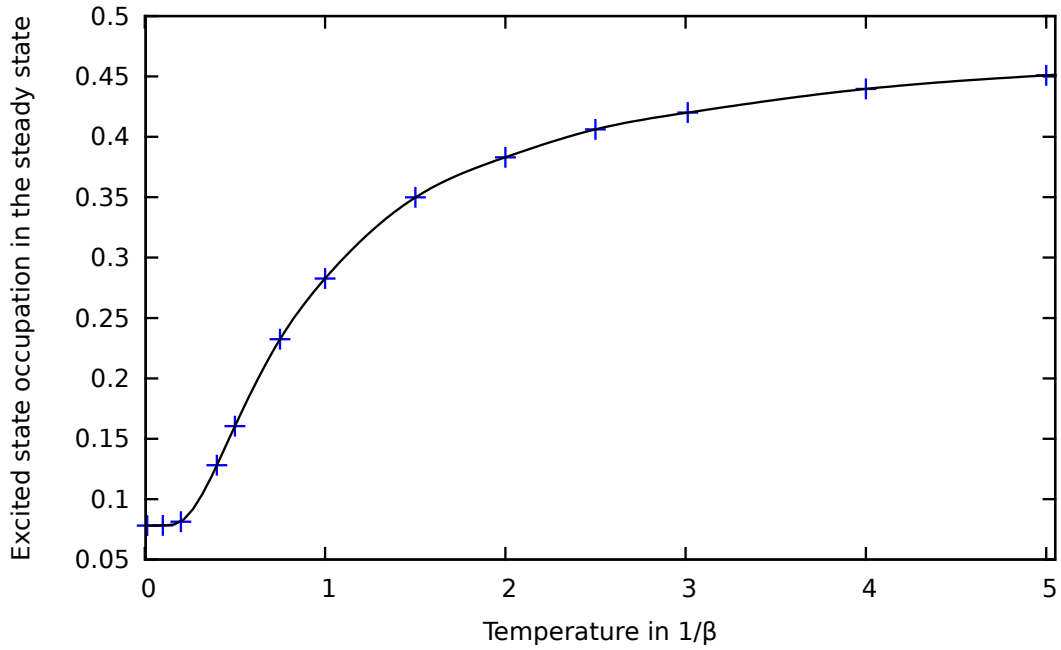


Figure 7.7: Excited state population in the steady state for a monomeric system, subject to spectral density $J_1(\omega)$, plotted over the inverse temperature $\beta$. The steady state is determined by TTM evolution of the initial TEDOPA trajectories.

- environment coherence time $t_{\mathrm{coh}}$,
- chain length $N$, and
- system dimension $d_{\mathrm{sys}}$.

TTM requires the simulation of $d_{\mathrm{sys}}^2$ trajectories until $t_{\mathrm{coh}}$, one for each independent initial density matrix. Although this overhead may become inconvenient for systems of large dimension, the computation easily parallelizes avoiding a scaling of $t_w$ with $d_{\mathrm{sys}}$. Even without parallelization, numerical studies often require exploration of a large number of independent initial conditions anyway.
Due to the efficiency of multiplicative propagation with TTM (Eq.7.8), nearly the totality of the wall time $t_w$ required for a simulation until $t_{\mathrm{sim}}$ is employed in the initial generation of the tensors until $t_{\mathrm{coh}}$ with TEDOPA. Therefore, one may consider $t_w$ to be essentially independent of $t_{\mathrm{sim}}$. This makes the TTM-TEDOPA combination suitable for long-time simulations, i.e. cases where $t_{\mathrm{sim}} \gg t_{\mathrm{coh}}$. There is an additional benefit in shortening simulations with TEDOPA to $t_{\mathrm{coh}}$, since this reduces the necessary chain length $N$.
The scaling of the wall time $t_w$ necessary to perform a TEDOPA simulation of time step $\delta t$ until $t_{\mathrm{coh}}$ can be expressed as

$$t_w \propto N \frac{t_{\mathrm{coh}}}{\delta t} \bar{t}, \tag{7.18}$$

where dependence on three factors has been made explicit: The number of sites $N$, the number of time steps $\frac{t_{\mathrm{coh}}}{\delta t}$ and a factor $\bar{t}$ denoting the average wall time necessary to simulate one chain site during one time step $\delta t$.

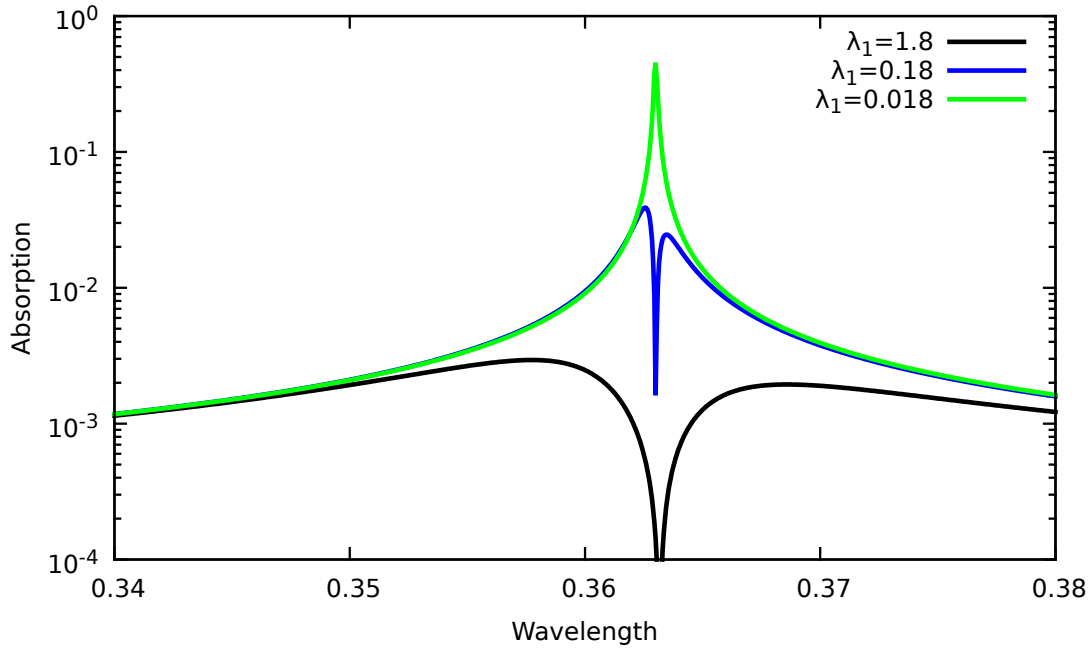


Figure 7.8: Peak structure of the absorption spectrum of a dimer at increasing system-environment coupling strength. The emergence of the vibrational fine structure is shown for increasing strength of the coupling to the environment.

However, in order to avoid end-of-chain recurrences, for a simulation time $t_{\mathrm{coh}}$ one requires $N$,

$$N \propto t_{\mathrm{coh}} \cdot \bar{v}, \tag{7.19}$$

sites in the environment, given an average propagation speed $\bar{v}$ in the chain. Thus a total wall time of

$$t_w \propto \frac{\bar{v}\bar{t}}{\delta t} t_{\mathrm{coh}}^2 \equiv c \cdot t_{\mathrm{coh}}^2, \tag{7.20}$$

is needed where $c$ is a scenario-dependent constant.

The global speedup provided by the TTM-TEDOPA combination is illustrated in Fig. 7.9 for three instances with different spectral densities. The near independence of $t_w$ on $t_{\mathrm{sim}}$ is shown for large $t_{\mathrm{sim}}$. As shown in the inset, in reality $t_w$ increases linearly with $t_{\mathrm{sim}}$, although with a negligible slope. For simulations with TEDOPA alone, the quadratic dependence expressed in Eq.(7.20) extends beyond $t_{\mathrm{coh}}$ until $t_{\mathrm{sim}}$.

## 7.8 Conclusions

In the analysis above we demonstrated the enhancement of the TEDOPA method by applying the tool set of TTM, resulting in a method well-suited, but not restricted to, low-temperature regimes and highly structured spectral densities and for very long simulation times.

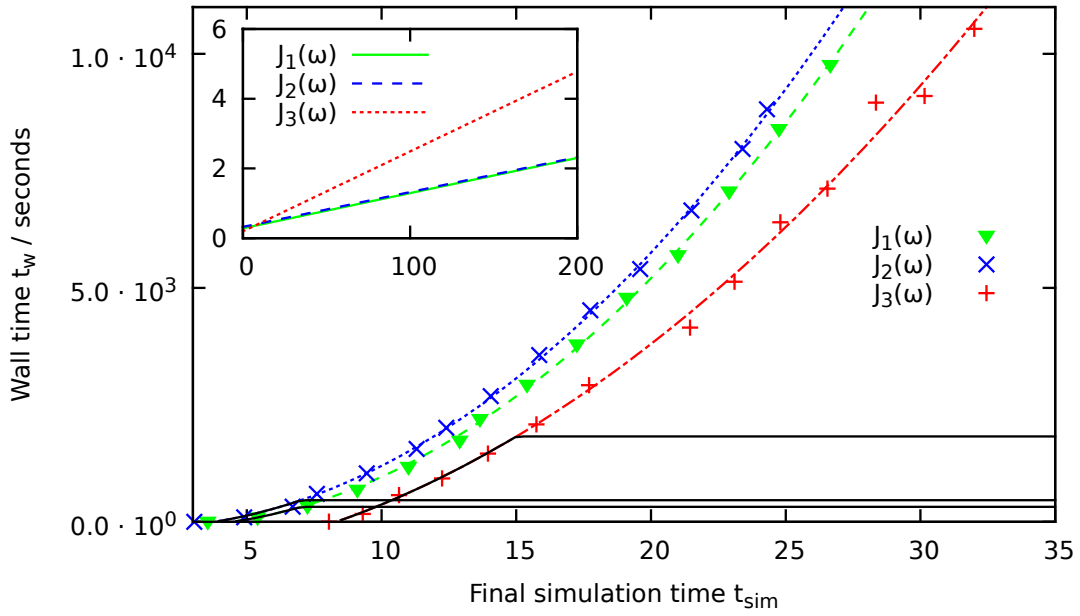


Figure 7.9: The data points show single-core TEDOPA wall times $t_w$ for a specific simulation time $t_{\text{sim}}$; the respective line of the same color is the corresponding quadratic fit. Black lines show the simulation time for the same physical setting upon employing the combination of TEDOPA and TTM. The TTM-part grows linearly as can be seen in the inset (on the main panel the slope of these lines is so small that they appear horizontal).

We verified the feasibility of this combination by a benchmark and presented applications for various spectral densities to highlight the flexibility of our method. In spite of the useful examples presented, even larger benefits can be expected upon application to simulations which are post-processed by some averaging-type method. These are often noise-tolerant or noise-stable, so small deviations do not change the characteristic features of the final result. Such methods include, but are not limited to, compressed sensing [173, 174] or Fourier and wavelet transformations [175]. A physical connection to the last example would be the calculation of emission or fluorescence spectra from the two point correlation functions and the analysis of time dependent 2D spectra.

# CHAPTER 8

## Reduced-Rank Randomized Singular Value Decomposition

In the previous chapter we drew on open quantum system methods to extend TEDOPA to regimes that previously were only reachable by employing huge computational resources. Now we again optimize TEDOPA, this time focusing on the numerical part – the TEBD algorithm – to be subject of improvement. Specifically, we optimize its most costly part, the two-site update step, by resorting to a different algorithm to perform the SVD. In Chapter 3 we already covered the basic properties of the generic SVD as it is implemented in most numerical libraries. Further we covered its integration into the TEBD algorithm and why it is applied. These considerations also extend beyond the TEBD to various MPS-based representations and algorithms. In this chapter we introduce an algorithm that uses random numbers, thus is of probabilistic nature, and combined with a highly efficient low-level implementation helps to considerably reduce the necessary numerical resources and improve the scaling of TEBD. We further highlight for which parameter regimes this improvement results in the largest savings on computational time. Large parts of this chapter are based on material first presented in [4].

## 8.1 Motivation

When the amount of entanglement in a quantum system is limited, the relevant dynamics of the system is restricted to a very small part of the state space. When restricted to this subspace, the description of the system becomes efficient in the system size, resulting in a polynomial scaling of the resources with the system size. One specific setting of considerable practical importance that allows for efficient approximate description of quantum many-body systems concerns systems whose entanglement content is limited. The dynamics of such one-dimensional quantum many-body systems are then accessible via various methods. The time-dependent DMRG (t-DMRG) [176], the time-dependent Matrix Product States (t-MPS) [177], and the TEBD from Section 3.3 are all algorithms based on the idea of evolving an MPS [52] in time. In settings in which only a restricted amount of entanglement is present in the system, these methods are very efficient and the cost of simulation scales merely polynomially in the system size. A very clear presen-

tation of these three algorithms as well as a discussion of the main differences between them can be found in [47].
All these algorithms rely on the selection of the relevant subspace through a decimation technique based on the SVD. As already seen in the case of the TEBD in Section 3.3.3, due to its computational complexity the SVD often is the bottleneck of an algorithm's implementation. In this chapter we show how to address this issue within the TEBD framework by replacing the SVD which is used to restrict the Hilbert space of quantum states relevant to the system dynamics, with the Reduced-Rank Randomized SVD (RRSVD) proposed in [178]. We show that when the Schmidt coefficients decay exponentially, the polynomial complexity of the TEBD decimation step can be reduced from $\mathcal{O}(n^3)$ to $\mathcal{O}(n^2)$ with $n$ indicating the linear dimension of the square matrix to decompose. This results in a considerable speed-up for the TEBD algorithm for real world problems, enabling the access of larger parameter spaces, faster simulation times, and thus opening up new regimes that were previously inaccessible.
In the following analysis we start by identifying and highlighting the crucial step in which the RRSVD routine can be applied for considerable benefit. In Section 8.3 we then proceed with a description of the salient features of the RRSVD algorithm and a discussion of the speed-up that it provides over the standard SVD. Benchmarking in the TEBD context with applications to TEDOPA, along with stability analysis, is presented in Section 8.4.

## 8.2 An advanced application of the TEBD algorithm

The TEBD algorithm is remarkably useful also in scenarios which at first seem to be quite different from quantum many-body systems. One such example is its usage in the TEDOPA framework where it aids in the treating of open quantum systems. TEDOPA itself was already introduced thoroughly in Section 3.4; here we restrict ourselves to briefly lay out our benchmark system used to show in which regimes RRSVD proves to be most useful an how to speed up previous simulations.
this benchmark system will be a dimeric complex of two two-level open quantum systems. Each of these open quantum systems is described by the spin-boson model where the central spin interacts linearly with an environment modeled by harmonic oscillators. For each of the open systems TEDOPA then employs a unitary transformation reshaping the spin-boson model into a one-dimensional configuration. Thereafter the configuration is adjusted appropriately to suit numerical needs (see also Section 3.4). For each environment we keep $N$ sites of oscillators with $d_{k,\max}$ levels each.

The two open quantum systems exhibit an energy splitting of $\varepsilon_1$ are subject to Hamiltonian

$$H_{\text{sys}} = \varepsilon_1|10\rangle\langle 10| + \varepsilon_2|01\rangle\langle 01| + J\left(|10\rangle\langle 01| + |01\rangle\langle 10|\right) \tag{8.1}$$

with parameters $\varepsilon_1 = 335\text{cm}^{-1}$, $\varepsilon_2 = 200\text{cm}^{-1}$, and $J = 52\text{cm}^{-1}$. The state $|10\rangle$ ($|01\rangle$) denotes excitation of the left (right) site. The environment's spectral density $J(\omega)$ is the same as employed in Chapter 5 from Reference [97].

The system's initial state is $\rho_{\text{sys}} = |\psi\rangle\langle\psi|$ with $|\psi\rangle = \frac{|e_1\rangle+|e_2\rangle}{\sqrt{2}}$ with excitonic eigenstates $|e_1\rangle$ and $|e_2\rangle$ (where the energy $E\left(|e_1\rangle\right)$ of $|e_1\rangle$ is smaller than $E\left(|e_2\rangle\right)$). At the beginning

of the time evolution each environment is in a thermal state at temperature $T = 277$ K. The total state is a product state of system and environment. This setting corresponds to one of the comprehensively investigated applications from Chapter 5, thus perfectly illustrating the corresponding speed-up in a real-world setting.

## 8.3 Reduced-rank randomized SVD

The efficiency of TEBD and MPS-based algorithms comes from the possibility of approximating states in an exponentially large Hilbert space by states that are described by a number of parameters that grows only polynomially with the system size. In order to better understand the role of the SVD in these settings, we introduce the following task: Given a complex $m \times n$ matrix $A$, provide the best rank-$k$ ($k \leq n$) approximation of $A$. Without loss of generality we suppose $m \geq n$ and $rank(A) = n$. The solution to this is well known [179]: First compute the SVD of $A = U\Sigma V^\dagger$, where $U = \left(U^{(1)}, U^{(2)}, \ldots, U^{(n)}\right)$, $V = \left(V^{(1)}, V^{(2)}, \ldots, V^{(n)}\right)$ are the left and right singular vectors of $A$ respectively and $\Sigma = \text{diag}\left(\sigma_1, \sigma_2, \ldots, \sigma_n\right)$ with $\sigma_1 \geq \sigma_2 \geq \ldots \geq \sigma_n$. Then retain the $k$ largest singular values $(\sigma_1, \sigma_2, \ldots, \sigma_k)$ and build the matrices $U_k = \left[U^{(1)}, U^{(2)}, \ldots, U^{(k)}\right]$ and $V_k = \left[V^{(1)}, V^{(2)}, \ldots, V^{(k)}\right]$. The matrix $\widetilde{A}_k = U_k \Sigma_k V_k^\dagger$ satisfies

$$||A - \widetilde{A}_k||_F = \sqrt{\sum_{i=k+1}^{n} \sigma_i^2} = \min\left(_,rank(A') = k\right) ||A - A'||_F, \tag{8.2}$$

where $||\cdot||_F$ indicates the Frobenius norm

$$||A||_F = \sqrt{\sum_{i=1}^{n} \sigma_i^2}. \tag{8.3}$$

In other words, $\widetilde{A}_k$ provides the best rank-$k$ approximation of $A$.

The computational complexity of the SVD of $A$ is $\mathcal{O}(m \cdot n^2)$. For large matrices, the SVD can therefore require a significant amount of time. This is a crucial point since every single TEBD simulation step of an $N$-sites spin chain requires $\mathcal{O}(N)$ SVDs which often consumes about 90% of the total simulation time.
As thoroughly highlighted in the discussion of the TEBD algorithm ( Section 3.3), dimension-reduction of an MPS (or MPO) with bond-dimension $n$ to an MPS with bond-dimension $\chi$ requires discarding of $n - \chi$ singular values (and corresponding left-/right- singular vectors). The prototypical case of course is the TEBD two-site update step where we keep only $\chi$ singular values out of $n = d \cdot \chi$ (pure states) or $n = d^2 \cdot \chi$ (mixed states). Most of the singular values and left-/right-singular vectors are therefore discarded. This means that we are investing time and computational resources to compute information that is then wasted.

It is possible to avoid the *full* SVD of $A$ and compute only the first $k$ singular values and corresponding singular vectors by using *truncated SVD* methods; such methods are standard tools in data-classification algorithms [180], signal-processing [181] and other

research fields. The Implicitly Restarted Arnoldi Method [182, 183] and the Lanczos-Iteration [184] algorithms, both belonging to the Krylov-subspace iterative methods [185, 186], are two examples.
The Reduced-Rank Singular Value Decomposition (RRSVD), originally presented in by N. Halko *et al.* [178], is a *randomized* truncated SVD. It is particularly well suited to decompose structured matrices, such as those appearing in the TEBD simulation of non-critical quantum systems. Most interestingly, the algorithm is insensitive to the quality of the random number generator used, delivers highly accurate results and is, despite its random nature, very stable: The probability of failure can be made arbitrarily small with only minimal impact on the necessary computational resources.
In what follows we will describe the RRSVD algorithm and report the main results on stability and accuracy. For a full account on RRSVD we refer the reader to [178].

The RRSVD algorithm is a two-step procedure. The first step constructs an orthogonal matrix $Q$ whose columns constitute a basis for the approximated range of the input matrix $A$. In the second step, the approximated SVD of $A$ is computed by performing an SVD of $Q^\dagger A$.
The approximation of the range can be done either for fixed *error tolerance* $\epsilon$, namely by finding a $Q_\epsilon$ such that

$$||A - Q_\epsilon Q_\epsilon^\dagger A|| \leq \epsilon, \tag{8.4}$$

or for a fixed rank $k$ of the approximation, that is by finding $Q_k$ such that

$$\min{}_{(,rank(X)\leq k)} ||A - X|| \approx ||A - Q_k Q_k^\dagger A||. \tag{8.5}$$

The first is known as the *fixed-precision approximation problem*, whereas the second is known as the *fixed-rank approximation problem*. Here and in what follows, we indicate by $||A||$ the operator norm, corresponding to the largest singular value of $A$.
If $\sigma_j$ is the $j$-th largest singular value of $A$ then

$$\begin{aligned}&\min{}_{(,rank(X)\leq k(\epsilon))} ||A - X||_F = \\ &= ||A - Q_{k(\epsilon)} Q_{k(\epsilon)}^\dagger A||_F = \sqrt{\sum_{j=k(\epsilon)+1}^{n} \sigma_j^2}.\end{aligned} \tag{8.6}$$

where $\sigma_{k(\epsilon)}$ is the first singular value $\geq \epsilon$ and the columns of the rank-$k(\epsilon)$ matrix $Q$ are the first $k(\epsilon)$ left singular vectors of $A$. This however would require the knowledge of the first $k(\epsilon)$ singular values and vectors of $A$.
For the sake of simplicity, let us focus initially on the fixed-rank approximation problem. In order to determine $Q_k$ we resort to randomness. More precisely, we use a sample of $k+p$ random vectors $\omega^{(i)}$, whose components are independently drawn form a standard Gaussian distribution $\mathcal{N}_{(\mu=0,\sigma=1)}$. The set $\left\{\omega^{(i)}\right\}_{i=1}^{k+p}$ will be with *very high probability* a set of independent vectors. The parameter $p$ determines the amount of *oversampling* necessary to make the rank-$k$ approximation of $A$ more precise. The $m \times (k+p)$ matrix

$$Y = A\Omega, \tag{8.7}$$

where $\Omega = (\omega^{(1)}, \omega^{(2)}, \ldots, \omega^{(k+p)})$, will therefore have full rank $(k+p)$. By re-orthogonalizing the columns of the matrix $Y$ we obtain a basis for the rank-$(k+p)$ approximation of the range of $A$. The re-orthogonalization can be done by using the QR-decomposition $Y = QR$. If $(k+p) < n$, the computational cost of the first step of this algorithm is dominated by the matrix multiplication $A\Omega$: This operation has an asymptotic complexity $\mathcal{O}(mn(k+p))$, whereas the QR-decomposition of the $m \times (k+p)$ matrix $Y$ has asymptotic complexity $\mathcal{O}(m(k+p)^2)$.
When the input matrix $A$ is very large, the singular vectors associated with small singular values may interfere with the calculation. In order to reduce their weight relative to the dominant singular values it is expedient to take powers of the original matrix $A$. So, instead of computing $Y = A\Omega$ we compute

$$Z = B\Omega = (AA^\dagger)^q A\Omega. \tag{8.8}$$

The singular vectors of $B = (AA^\dagger)^q A$ are the same as the singular vectors of $A$; for the singular values of $B$, on the other hand, the relation holds:

$$\sigma_j(B) = (\sigma_j(A))^{2q+1}\,, \tag{8.9}$$

This leads to the desired reduction of the influence on the computation of the singular vectors associated to small singular values. This "stabilizing" step, also referred to as *Power Iteration* step (PI), increases the computational cost of the first step of the RRSVD algorithm by a constant factor $(2q+1)$.
A side effect of the PI is the extinction of all information pertaining to singular vectors associated to small singular values due to the finite size of floating point number representation. In order to avoid such losses, we use intermediate re-orthogonalizations (see Algorithm 8.1). We point out that in the typical context where TEBD is successfully applied the singular values of the according matrices decay very fast, so that the PI scheme has to be applied.
Since the RRSVD is a randomized algorithm, the quality of the approximation comes in the form of expectation values, standard deviations and failure probabilities. We report pertinent results that can be found (including proofs) in [178], as well as some particular results tuned to cases of specific relevance to applications for TEBD.

**Theorem 1.** *(Corollary* 10.10 *in [178])*
*Given a target rank $k \geq 2$ and an oversampling parameter $p \geq 2$, let $Q_Z$ be the orthogonal $m \times (k+p)$ matrix consisting of the fist $k+p$ left singular vectors of the matrix $Z$ defined in Eq.* (8.8)*. We define $P_Z = Q_Z^\dagger Q_Z$. Then*

$$\begin{aligned}\mathbb{E}\left(||\left(\mathbb{I} - P_Z\right)A)||\right) &\leq \left[\left(1+\sqrt{\frac{k}{p-1}}\right)\sigma_{k+1}^{2q+1} + \frac{e\sqrt{k+p}}{p}\left(\sum_{j>k}\sigma_j^{2(2q+1)}\right)^{\frac{1}{2}}\right]^{\frac{1}{2q+1}} \\ &\leq \left[1+\sqrt{\frac{k}{p-1}} + \frac{e\sqrt{k+p}}{p}\sqrt{n-k}\right]^{1/(2q+1)} \sigma_{k+1}. \end{aligned} \tag{8.10}$$

The application of the PI scheme reduces the average error exponentially in $q$. In order to quantify the deviation from the expected estimation error, we use the facts

$$||\left(\mathcal{I} - P_Z\right)A||^{2q+1} \leq ||\left(\mathcal{I} - P_Z\right)B|| \tag{8.11}$$

(Theorem 9.2 [178]) and

$$|| \left(\mathcal{I} - P_Y\right) A|| \leq 1 + 6\sqrt{(k+p) \cdot p \log(p)}\sigma_{k+1} + 3\sqrt{k+p} \left(\sum_{j>k} \sigma_j^2\right)^{\frac{1}{2}}, \tag{8.12}$$

the last one holding with probability greater or equal to $1 - \frac{3}{p^p}$ (Corollary 10.9 [178]). We can now state

**Corollary 1.**
*Under the hypotheses from Theorem 1 it holds the inequality*

$$P\left(|| \left(\mathcal{I} - P_Z\right) A|| \leq \alpha^{\frac{1}{2q+1}}\sigma_{k+1} + \beta^{\frac{1}{2q+1}} \sum_{j>k} \sigma_j\right) \geq 1 - \frac{3}{p^p}, \tag{8.13}$$

*with* $\alpha = (1 + 6\sqrt{(k+p) \cdot p \log(p)})$ *and* $\beta = 3\sqrt{k+p}$.

*Proof.* By applying Eq. (8.12) to $B = (AA^\dagger)^q A$ and using Eq. (8.9), we obtain

$$P\left(|| \left(\mathcal{I} - P_Z\right) B|| \leq \alpha\sigma_{k+1}^{2q+1} + \beta \left(\sum_{j>k} (\sigma_j^{2q+1})^2\right)^{\frac{1}{2}}\right) \geq 1 - \frac{6}{p^p}. \tag{8.14}$$

By relation Eq. (8.11) we have

$$|| \left(\mathcal{I} - P_Z\right) A|| \leq \left(\alpha\sigma_{k+1}^{2q+1} + \beta \left(\sum_{j>k} (\sigma_j^{2q+1})^2\right)^{\frac{1}{2}}\right)^{1/(2q+1)} \tag{8.15}$$

and since the function $f(q) = a^{1/x}, a > 0, x > 0$ is convex, it holds

$$\begin{aligned}
&\left(\alpha\ \sigma_{k+1}^{2q+1} + \beta \left(\sum_{j>k} (\sigma_j^{2q+1})^2\right)^{\frac{1}{2}}\right)^{1/(2q+1)} \\
\leq &\left(\alpha\ \sigma_{k+1}^{2q+1}\right)^{\frac{1}{(2q+1)}} + \left(\beta \sqrt{\sum_{j>k} (\sigma_j^{2q+1})^2}\right)^{\frac{1}{2q+1}} \\
\leq &\alpha^{\frac{1}{2q+1}}\sigma_{k+1} + \beta^{\frac{1}{2q+1}} \sqrt{\sum_{j>k} \sigma_j^2} \\
= &\alpha^{\frac{1}{2q+1}} ||A - \widetilde{A}_k|| + \beta^{\frac{1}{2q+1}} ||A - \widetilde{A}_k||_F.
\end{aligned} \tag{8.16}$$

□

The results the algorithm delivers are usually closer to the average value than those estimated by the bound Eq. (8.10). The bound therefore appears to be not tight. However, the important message of the previous results is, that by applying the PI we obtain a much better approximation of $A$ than that provided by the original scheme – while at

Algorithm 8.1: **Randomized SVD with Power Iterations**

**Require:** $m \times n$ matrix $A$; integers $l = k+p$ (rank of the approximation) and $q$ (number of iterations)

1: Draw an $n \times l$ Gaussian matrix $\Omega$
2: Form $Y_0 = A\Omega$
3: Compute the QR factorization $Y_0 = Q_0 R_0$
4: **for** $j = 1, 2, \ldots, q$ **do**
5: Form $\widetilde{Y}_j = A^\dagger Q_{j-1}$
6: Compute the QR factorization $\widetilde{Y}_j = \widetilde{Q}_j \widetilde{R}_j$
7: Form $Y_j = A\widetilde{Q}_j$
8: Compute the QR factorization $Y_j = Q_j R_j$
9: **return** $Q = Q_q$

the same time error expectations and deviations are under full control.

It would be most convenient to have some means to check how close $QQ^\dagger A$ is to the original input matrix $A$. With such a tool, we could check the quality of the approximation; moreover, we would be able to solve the fixed-error approximation problem Eq. (8.4). In the TEBD setting, this would allow us to determine the bond dimension $\chi$ for an assigned value $\epsilon$ of the truncation error. The solution to this is given by

**Theorem 2.** *(Eq. 4.3 supported by Lemma 4.1 [178])*
*For $M = (I - QQ^\dagger)A$ we have*

$$P\left(||M|| \leq 10\sqrt{\frac{2}{\pi}} \max_{i=1,2,\ldots,r} ||M\omega^{(i)}||\right) \geq 1 - 10^{-r}, \tag{8.17}$$

*where $\omega^{(i)}, i = 1, \ldots, r$ are standard normal random vectors.*

Suppose the first three steps of Algorithm 8.1 have been completed. Now set $Q = Q_0$, with $rank(Q) = l = k + p$, and choose the size $r$ of the sample. The *Accuracy Check* Algorithm 8.2 takes as input the values of $A, Q, r$, and $\epsilon$ and returns a new matrix $Q'$ that satisfies the accuracy bound with probability $1 - 10^{-r}$. The computational cost of the Accuracy Check depends on different parameters. The cost of each iteration step is $\mathcal{O}(m \cdot l^2)$. Further we need to consider the number of iterations – if we take $r$ too small (e.g. $r = 1$), then for a starting rank-$l$ approximation that is not sufficient we might need many iteration to converge to the desired accuracy. As a rule of thumb, we suggest to double the rank of the approximation at each time. This will likely lead to oversampling, but still delivers a good performance.

Since the reference metric in the TEBD is the Frobenius norm, Eq. (8.3), some estimate of the Frobenius norm via the operator norm is required. To this end we remark again that TEBD can successfully be applied if the correlations in the simulated system are sufficiently short-ranged, i.e. the singular values decay "fast enough". If the entanglement between distant parts of the system is non-vanishing, the decimation step will lead to an important loss of relevant information. As an example let us consider a spin chain of size $N$ and a bipartition $A = \{1, 2, \ldots l\},\ B = \{l+1, \ldots, N\}$ of the chain. Let $|k\rangle_A$ and

Algorithm 8.2: **Accuracy Check**

**Require:** $m \times n$ matrix $A$; rank-$(k+p)$ projector $P_Q = QQ^\dagger$; integer $r$; tolerance $\epsilon$

**do**
  Set $l = k + p$
  Draw an $n \times r$ Gaussian matrix $\Omega_r$
  Compute $B = A\Omega_r$
  Compute $D = (I - P_Q)A\Omega_r = \left(d^{(1)}, d^{(2)}, \ldots, d^{(r)}\right)$
  Set MAX= $\max\left\{d^{(i)}\right\}_{i=1}^{r}$
  **if** (MAX $> \epsilon$) **then**
    Build $\widetilde{Q} = Q|B$
    Set $l = l + r$
    Compute the QR-decomposition $\widetilde{Q} = \widetilde{Q}'\widetilde{R}'$
    Set $Q = \widetilde{Q}'$
**while** (MAX $> \epsilon$ and $l \leq n - r$ )
**return** $Q$

$|j\rangle_B$ be orthonormal bases for subsystems $A$ and $B$ respectively. Then the state $|\psi\rangle$ of the spin chain can be Schmidt-decomposed as

$$|\psi\rangle = \sum_{k,j} c_{k,j}|k\rangle_A|j\rangle_B = \sum_i \sigma_i|i\rangle_A|i\rangle_B, \tag{8.18}$$

where in the last equality we used the SVD of the matrix $C = (c_{j,k}) = U\Sigma V^\dagger$ to perform the Schmidt decomposition of $|\psi\rangle$. The Schmidt coefficients $\sigma_i$ are the singular values of $C$, i.e. the diagonal elements of $\Sigma$ [17]. The number of non-zero singular values is the Schmidt number. The amount of entanglement between the subsystems $A$ and $B$ can be quantified by the von Neumann, or entanglement, entropy [187] of the reduced density matrices $\rho_A$ and $\rho_B$

$$S(\rho_A) = -\sum_i \sigma_i^2 \log(\sigma_i^2) = S(\rho_B). \tag{8.19}$$

The decay rate of the singular values is therefore directly related to the amount of entanglement shared between two parts of a system. If the system is highly entangled, the singular values will decay "slowly"; in the limiting case where the system is maximally entangled, the reduced density matrices will describe completely mixed states and the singular values will be all equal to each other. When the system is only slightly entangled, the singular values will decay very fast; in particular, if the state $|\psi\rangle$ is separable, the Schmidt number is equal to 1 (and $\sigma_1 = 1$). The behavior of the entanglement entropy in systems at, or close to, the critical regime has been thoroughly studied (see [57] and references therein) together with its dependence on the decay rate of the eigenvalues of the reduced density matrices $\rho_{A,B}$ [188, 189, 58, 59]. By oversimplifying the problem, we observe that if the singular values decay as $\sigma_j = 1/\sqrt{j}$ the entanglement entropy shows, when the system size $N \to \infty$, a divergence $\log^2(N)$, whereas if they decay as $\sigma_j = 1/j$ the entanglement entropy does converge, since an area law holds [57]. When the singular values decay as $1/j$, however, the truncation error $||A - \widetilde{A_k}||_F$ decreases slowly in $k$ and the TEBD scheme becomes inefficient since any decimation will lead to considerable

approximation errors (see Eq. (3.59)). For these reasons we consider the case of linearly decreasing singular values as an extremal case for the range of applicability of the TEBD algorithm.
This observation provides a useful tool to estimate the Frobenius norm (which plays a central role in TEBD) through the operator norm. For any matrix $A$ it is:

$$||A|| \leq ||A||_F \leq \sqrt{rank(A)}||A||.$$

This result holds in general. The inequalities are saturated, in particular, when $rank(A) = 1$. The upper bound on the Frobenius norm is the tighter the closer the singular values of $A$ are to each other. If the singular values decay at least as $1/j$, on the other hand, we obtain the following result:

**Fact 1.**
*Given a rank-n matrix $A$ with singular values $\sigma_1 \geq \sigma_2 \geq \ldots \geq \sigma_n$ with $\sigma_j \leq \sigma_1/j, j = 1, \ldots, n$, the Frobenius norm can be upper bounded,*

$$||A||_F \leq \frac{\pi}{\sqrt{6}}||A|| = \sigma_1 \frac{\pi}{\sqrt{6}}, \tag{8.20}$$

*where $||A||$ denotes the operator norm.*

*Proof.*

$$||A||_F = \sqrt{\mathrm{tr}\left[A^\dagger A\right]} = \sqrt{\sum_{i=1}^{n} \sigma_i^2} \leq \sigma_1 \sqrt{\sum_{i=1}^{n} \frac{1}{i^2}}, \tag{8.21}$$

where the last term can further be upper bounded with

$$\lim_{n\to\infty} \sqrt{\sum_{i=1}^{n} \frac{1}{i^2}} = \frac{\pi}{\sqrt{6}}. \tag{8.22}$$

□

This result finds application in the Accuracy Check routine. If we set $P_Q = QQ^\dagger$ we find

$$\begin{aligned} ||(I - P_Q)A||_F &= \sqrt{\mathrm{tr}\left[(A - P_Q A)^\dagger (A - P_Q A)\right]} \\ &= \sqrt{\mathrm{tr}\left[A^\dagger A\right] - \mathrm{tr}\left[A^\dagger P_Q A\right]} \\ &= \sqrt{||A||_F^2 - ||A^\dagger Q||_F^2} \\ &\leq ||A||_F. \end{aligned} \tag{8.23}$$

Therefore we have

$$\begin{aligned} ||(I - P_Q)A||_F &\leq \frac{\pi}{\sqrt{6}}||A||_F \\ &\leq \frac{10}{3}\pi \max_{i=1,2,\ldots,r} ||(I - QQ^\dagger)A\omega^{(i)}|| \end{aligned} \tag{8.24}$$

with probability $1 - 10^{-r}$.

We point out that it is not really necessary to *estimate* the Frobenius norm of the error: Given $Q$ we can compute $||(I - QQ^\dagger)A||_F$ directly. However, one should note that this computation of $QQ^\dagger A$ requires $2(m \cdot n \cdot k)$ floating point operations instead of the $2(m \cdot k \cdot r) + m \cdot n \cdot r$ operations required to obtain the error estimate. We observe that the error probability $1 - 10^{-r}$, becomes negligible ($10^{-50}$ or even less) for real-life situations (remember that this algorithm is designed to work on large matrices, i.e. $> 500 \times 500$). Now that we have the orthogonal matrix $Q$ whose columns constitute a basis for the approximated range of the input matrix $A$, we can directly compute the approximate SVD of $A$ by:

(i) Form the matrix $B = Q^\dagger A$

(ii) Compute the SVD of $B$: $B = \widetilde{U}\Sigma V^\dagger$

(iii) Form the orthonormal matrix $U = Q\widetilde{U}$.

The product $Q^\dagger A$ requires $\mathcal{O}((k+p) \cdot n \cdot m)$ floating point operations. The SVD of $B$, under the reasonable assumption that $k + p \leq n$, requires $\mathcal{O}(n \cdot (k+p)^2)$ operations. The product $Q\widetilde{U}$ requires $\mathcal{O}(m \cdot (k+p)^2)$ operations.
We conclude this section by presenting some results for the computational cost of the whole procedure, as well as on some more technical aspects related to the implementation of the algorithm. The asymptotic computational cost of partial steps has been given at various places in this section. In summary, the real bottleneck of the complete RRSVD algorithm is the first matrix multiplication $Y = A\Omega$ which has complexity $\mathcal{O}(m \cdot n \cdot (k+p))$. The value of $p$ can be set in advance or determined by the Accuracy Check method described above. All remaining operations, such as QR-decompositions and error estimation, have smaller computational complexity. If the TEBD scheme is applied in a non-adaptive way, i.e. the bond dimension is fixed at a given value $\chi$, we use the RRSVD to solve the fixed-rank problem. In this case the RRSVD has complexity $\mathcal{O}(m \cdot n \cdot \chi)$. If the bond dimension $\chi$ is set independently of the input matrix size, the replacement of the standard SVD by RRSVD will therefore result in a speed-up linear in $n$. On the other hand, if we use an adaptive TEBD simulation where the bond dimension is set such that some bound on the approximation error is satisfied, the cost of RRSVD will (strongly) depend on the structural properties of the input matrices. If the singular values decay exponentially (corresponding to short-ranged correlations), then the expected speed-up is roughly the same as for the non-adaptive scheme. If the simulated system presents long-ranged correlations, then the speed-up provided by RRSVD will be less than linear in $n$, possibly even vanishing. However, TEBD itself is not the ideal tool to deal with systems exhibiting long-range correlations, so this is only a minor limitation.
Another crucial observation related to the implementation is, that all the operations required by RRSVD are standard functions of either the Basic Linear Algebra Subprograms (BLAS) [190] or the Linear Algebra PACKage (LAPack [191]) library. Both libraries are heavily optimized and available for single-core, multi-core (e.g. Intel Math Kernel Library (MKL) [192]) and Kilo-processor architectures (e.g. CuBLAS [193] and CULA [194]). Since TEBD simulations are usually run on many cores (on current cluster architectures often 8 or 16), RRSVD can take full advantage of these optimized libraries.

## 8.4 RRSVD case-study and profiling of real TEBD simulations

We start by showing that, despite its random nature, RRSVD produces very accurate results with surprisingly small fluctuations. To this end we test the described algorithm on a sample of relatively small, structured matrices extracted from pure-state TEBD simulations of our benchmark system from Section 8.2, subsequently continuing to larger matrices from mixed-state TEBD simulations of the same system. We analyze the accuracy of RRSVD and its time performance, concluding by presenting how RRSVD impacts full TEBD simulations.

### 8.4.1 Stability analysis

In order to benchmark the stability of the RRSVD algorithm, we consider a set of 7 diagonal $750 \times 750$ matrices $\Sigma_m$, $m = 1, 2, \ldots, 7$. The matrices $\Sigma_m$ are extracted from an actual pure-state TEBD simulation of our benchmark system from Section 8.2. For every $\Sigma_m$ we generate a set of $n_A = 20$ random matrices $\{A_{m,i}\}_{i=1}^{n_A}$ by generating $1500 \times 750$ random orthonormal matrices $U_{m,i}$ and $750 \times 750$ random orthonormal matrices $V_{m,k}$; each matrix $A_{m,i}$ has dimensions $1500 \times 750$. This way we can compare the performance of both the standard LaPack SVD and the RRSVD on different matrices that exhibit the same structural properties. In order to take the random nature of RRSVD into account, for *each* $A_{m,i}$ we perform $n_R = 20$ executions of RRSVD. In this first benchmark we provide a rank-50 approximation of the rank-750 original matrices $A_{m,i}$ and show how the accuracy is related to the number of subspace iterations $q$. Motivated by the theorems in the previous section, we set $p = 50$. We compare the accuracy and timing results for different values $q = 2, 4, 6$ of the iteration parameter $q$. The Accuracy Check of the algorithm is not included yet: We do not estimate the difference between the original matrix $A$ and its projection on the reduced space.
By running the RRSVD on a set $\{A_{k,i}\}_{i=1}^{n_A}$ random realizations of matrices that exhibit the same structure, i.e. the same singular values $\Sigma_k$, we verify that the accuracy of RRSVD depends – for fixed number of iterations $q$, approximation-rank $k$, and oversampling parameter $p$ – only on the structural properties of the matrices. Therefore, in what follows we present an analysis that refers to the instance corresponding to the random realization $A_{2,1}$. This is, in every respect, a good representative of the matrices we deal with in a TEBD simulation of a pure quantum system far from the critical regime. In Fig. 8.1(a) we plot the singular values of $A_{2,1}$. It is important to notice that some of the largest singular values are very close to each other. This is a typical situation in which truncated-SVD methods that belong to the family of Krylov-subspace iterative methods are likely to require more iterations in order to accurately resolve these singular values. RRSVD, on the other hand, is completely insensitive to this peculiarity of the spectrum and provides very good results for the whole range of retained singular values ($k = 50$) starting from $q = 4$: The approximation error is comparable to that of the state-of-the-art LAPack SVD routine. Most noticeably, none of the $n_R$ executions of RRSVD on the instance $A_{2,1}$ presents *outliers*, that is to say singular values that are computed with anomalous inaccuracy (Fig. 8.1(b)) The behavior of the approximation error as a function of $q$ is compatible with the theoretical results stated in the previous section. In Table 8.1 we show the speed-up $t_{SVD}/t_{RRSVD}$ for both, MKL-SVD and MKL-based RRSVD, executed on an Intel Xeon X5570@2.93GHz with 8 concurrent threads (see Section 8.4.2 for more information about the implementation). The speed-up over the

| k/q | 0 | 2 | 4 | 6 | 8 | 10 |
|---|---|---|---|---|---|---|
| 50 | 11.6 | 5.4 | 3.5 | 2.6 | 2.04 | 1.7 |
| 100 | 4.7 | 2.3 | 1.5 | 1.1 | 0.89 | 0.69 |

Table 8.1: $A_{2,1}$: Speed-up ratio $t_{SVD}/t_{RRSVD}$ obtained by the RRSVD. The corresponding LAPack SVD time is 3.84 s

MKL-SVD is obviously decreasing as $q$ and $k$ increase: For $k = p = 100$ and $q = 6$ almost no advantage remains in applying RRSVD instead of the standard SVD.
It is worth stressing here that RRSVD is meant to deliver a substantial advantage only for very large matrices and a comparatively small number of retained singular values, as we will show later.

We now turn our attention to the TEBD extremal case discussed previously. We consider an $m = 1500, n = 750$ random matrix $A_c$ generated, as described at the beginning of this section, starting from singular values $\Sigma_c = diag(\sigma_1^c, \sigma_2^c, \ldots, \sigma_n^c)$ with $\sigma_i^c = 1/i$. As shown in Fig. 8.2(a), in order to provide the same accuracy as delivered by LAPack on the first $k$ singular values, we need to increase the number of iterations. For $k = 50$ and $q = 10$, RRSVD is still able to provide some speed-up over the LAPack SVD. But the real problem is the truncation error: For $k = 50$ we have a truncation error of $\epsilon \approx 10^{-1}$. But in order to achieve $\epsilon < 10^{-2}$, about 650 singular values need to be retained. This results in a major loss of efficiency of the TEBD simulation scheme. Therefore we can claim that RRSVD is indeed a fast and reliable method, able to successfully replace the standard SVD in the TEBD algorithm *in all situations* where TEBD can successfully be applied.

### 8.4.2 Performance on larger matrices and TEBD profiling

Now that the basic properties of the algorithm are established, we test it on larger matrices sampled from mixed-state TEBD simulations of our benchmark system from Section 8.2. Given the bond dimension $\chi$ and the local dimension $d$ of the sites involved in the two-site-update, the size of the matrix given as input to the SVD is $d^2\chi \times d^2\chi$. In the following example we set $k = \chi = 100$ and the dimension of the local oscillators to $3, 4, 5, 6$, and 7 respectively. We therefore present results for matrices of dimensions $d_3 = 900\times900, d_4 = 1600\times1600, d_5 = 2500\times2500, d_6 = 3600\times3600$ and $d_7 = 4900\times4900$. The structural properties of the test matrices considered are similar to the non-critical instances considered in the previous section. We first analyzed the results provided by the RRSVD routine on a large sample of matrices (200 instances for each dimension). We determined that the RRSVD reaches the LAPack accuracy for a number $q = 2$ of PI steps.

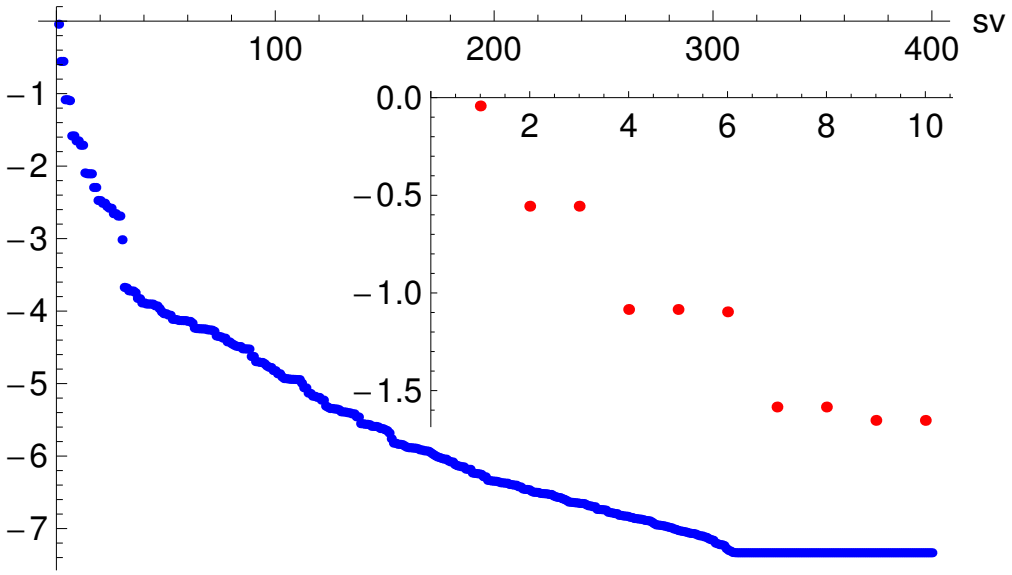


(a)

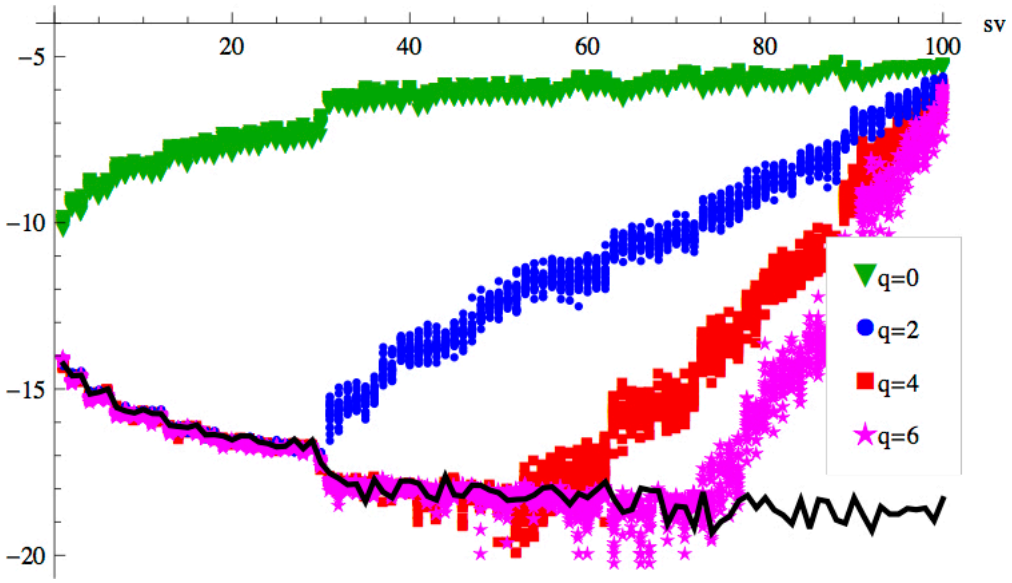


(b)

Figure 8.1: Instance $A_{2,1}$ with $m = 1500, n = 750$, and $k = p = 50$. The discarded weight is $w = 4 \cdot 10^{-4}$. (a) The y-axis gives the base-10 logarithmic value for the singular values (SVs) $\Sigma_2$: The decay shows to be roughly exponential. The inset shows the first 10 singular values: Some of them are very close to each other (with a difference of about $10^{-5}$). (b) The y-axis shows the magnitude of the errors $\log_{10}(|\sigma_i - \sigma_i^{RRSVD}|)$ of the RRSVD for each singular value and for all $n_R = 20$ executions of RRSVD on the same instance matrix $A_{2,1}$ for different values of the iteration number $q$. The standard MKL-SVD routine errors are shown by the thick black line.

| | 1-BL SVD | 1-BL RRSVD | 1-MKL-SVD | 1-MKL-RRSVD |
|---|---|---|---|---|
| $d_3$ | 13.27 | 6.62 | 1.47 | 0.71 |
| $d_4$ | 262.47 | 21.38 | 9.31 | 1.69 |
| $d_5$ | 449.97 | 37.19 | 31.87 | 3.62 |
| $d_6$ | 1464.67 | 74.48 | 97.37 | 6.97 |
| $d_7$ | 1973.23 | 99.9 | 241.01 | 11.49 |

| | 16-MKL-SVD | 16-MKL-RRSVD | GPU-SVD | GPU-RRSVD |
|---|---|---|---|---|
| $d_3$ | 0.46 | 0.14 | 1.08 | 0.25 |
| $d_4$ | 1.92 | 0.36 | 3.92 | 0.41 |
| $d_5$ | 6.07 | 0.54 | 9.95 | 0.61 |
| $d_6$ | 22.93 | 0.84 | 21.97 | 0.88 |
| $d_7$ | 61.51 | 1.43 | 49.00 | 1.48 |

Table 8.2: Execution time, in seconds, for the SVD of matrices of different sizes with LAPack SVD and RRSVD. The parameters for RRSVD are $q = 2$, $k = p = 100$. 1-BL: Single-thread CBLAS-LAPACKE-based implementation, executed on an Intel i7@2.66GHz processor. MKL: MKL-based implementation; 1-MKL: With one MKL thread, 16-MKL: With 16 MKL-threads, executed on one and two 8-core Xeon X5570@2.93GHz respectively. GPU: CUBLAS-CULA implementation executed on an NVIDIA K20s; the timing in this case includes host-to-device and device-to-host memory transfers.

The testing involved three different implementations we developed of the RRSVD algorithm: BL-, MKL- and GPU-RRSVD, each one using a different implementation of the BLAS and LAPack libraries. BL-RRSVD is based on a standard single-thread implementation (CBLAS [195], LAPACKE [196]); MKL-RRSVD uses the Intel® implementation Math Kernel Library (MKL [192]); GPU-RRSVD exploits CUBLAS[193] and CULA [194], i.e. the BLAS and LAPack libraries for Nvidia® Graphics Processing Units (GPUs). RRSVD is available for single/double precision real/complex matrices in each version. We refer the reader to [197] for detailed information about our RRSVD implementations. During the completion of this work, another implementation of RRSVD from one of the authors of [178] has been reported in [198]. The authors present three variants of RRSVD (essentially RRSVD with and without the PI and the Accuracy check) and discuss their performance on large (up to $6000 \times 12000$) real matrices with slowly decaying singular values. The implementation described in [198] is available for single-, multi- and Kilo-processor architectures, but is limited to double precision real matrices.

In Table 8.2 we show the times required to perform the SVD/RRSVD of $d_3, d_4, d_5, d_6$, and $d_7$ double-precision complex matrices for the three implementations.
RRSVD provides a speed-up (Fig. 8.3) which is consistent with the predictions except

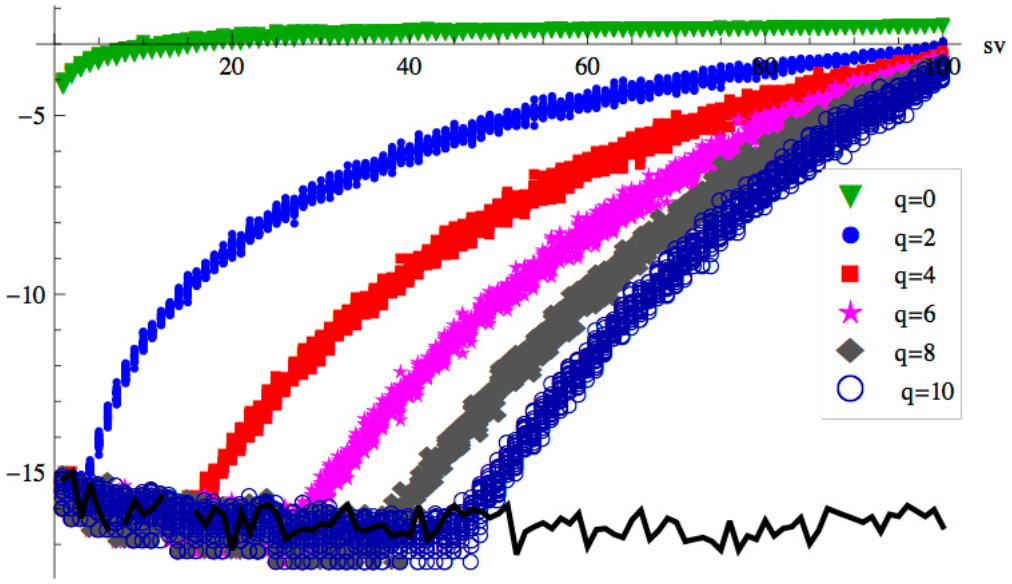


(a)

Figure 8.2: Instance $A_c$ with $m = 1500, n = 750$, and $k = p = 50$. Shown on the y-axis is the magnitude of the errors $\log_{10}(|\sigma_i - \sigma_i^{RRSVD}|)$ of the RRSVD as in Fig. 8.1(b), but referring to the singular values of the matrix $A_c$ and for $q \in \{0, 2, 4, 6, 8, 10\}$. The discarded weight $w$ for the chosen value of $k$ is $w = 1 \cdot 10^{-1}$.

in the 16-MKL case. For this case it grows stronger than linearly for matrix sizes in the range $d_3 - d_6$. This peculiar behavior is due to the low impact of the initial matrix multiplication $Y = A\Omega$ (and subsequent ones) on matrices of such sizes: This operation is heavily optimized for multi-threaded execution. Thus the operations that determine the computational cost are the QR- and the final singular value decompositions which have complexity $\mathcal{O}\left(m \cdot (k+p)^2\right)$. Since $k + p$ is kept constant, we obtain a quadratic speed-up. This justification is also supported by the speed-up scaling of the 1-MKL case. However, as the matrix size increases, the speed-up will tend to be linear (see the $d_7$ case). The performance on RRSVD provided by GPUs are comparable to those delivered by the 16-MKL. Indeed, the standard SVD is faster on the GPU starting from size $d_6$. This behavior was expected, since our test matrices are still too small to take full advantage of the Kilo-processor architecture.
At last we perform full TEBD simulations: For each dimension $d_i$, $i = 3, 4, 5, 6, 7$ we executed one full TEBD simulation with the standard SVD routine and another that employs the RRSVD. We ran all the jobs on the same cluster node, equipped with two Xeon X5570@2.93GHz with 8 cores each, as to assure a fair comparison.
In Fig. 8.4 we show the average time required by the TEBD two-site update, for the standard SVD and for the RRSVD. The overall speed-up of the two-site update (inset of Fig. 8.4) agrees with Amdahl's law [199]. The average is taken over all maximum-sized two-site updates performed in the TEBD simulation (more than 1500 for every dimension $d_i$). When the standard SVD is applied, it requires more than 90% of the overall computation time; however if RRSVD is used, the total time taken by the SVD

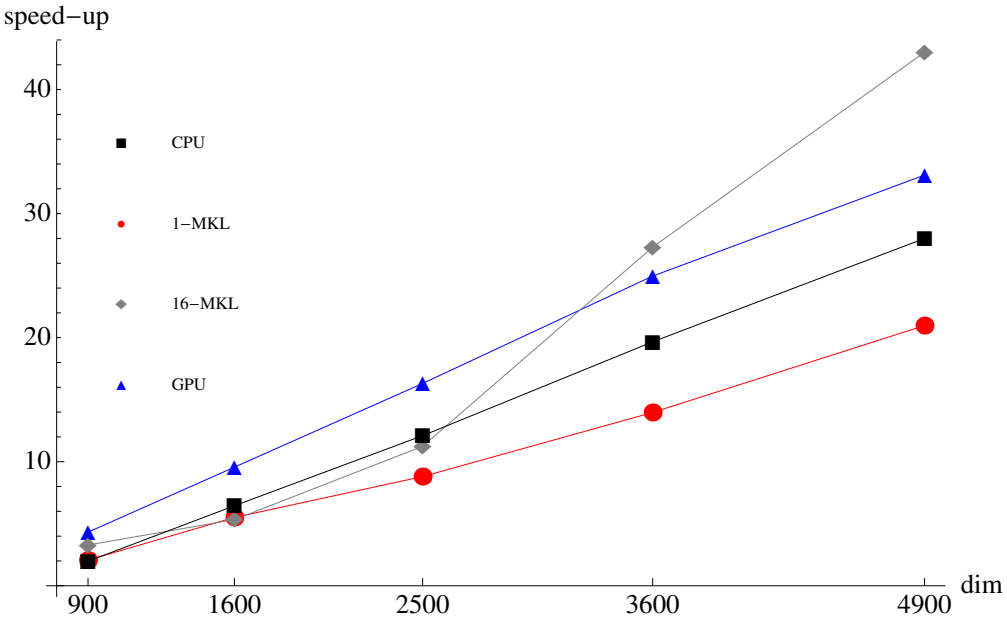


Figure 8.3: Scaling of the SVD/RRSVD speed-up for different platforms as a function of the matrix size, as obtained from the data reported in Table 8.2. Parameters are $k = p = 100$; $q = 2$.

reduces drastically. Its computational cost is of the same order as that of the building of the $\widetilde{\Theta}$ matrix (cf. Fig. 8.4). The fluctuations around the average RRSVD time are due to the action of the Accuracy-Check: From time to time the bond dimension $\chi$ must be increased in order to keep the approximation error below the threshold value $\epsilon = 10^{-3}$ required by the simulation. According to Corollary 1, for the choice $p = 100$ and $q = 2$, such an increase is motivated only by the decay rate of the singular values: The failure probability is smaller than $1/10^{100}$. This is confirmed by an *a posteriori* analysis of the matrices produced during the test TEBD simulations that required an extension of the bond dimension. The rank of the approximation proposed by RRSVD, for assigned tolerance $\epsilon$, can therefore be used to detect either an entanglement build-up in the system or an (unlikely) anomalous behavior of the RRSVD itself.

## 8.5 Conclusions and Outlook

The TEBD-algorithm, an important tool for the numerical description of one-dimensional quantum many-body systems, depends essentially on the SVD which, in current implementations, is the bottleneck. We have demonstrated that this bottleneck can be addressed by the successful application of the RRSVD algorithm to TEBD simulations. The block decimation step of the TEBD update procedure is now approximately one order of magnitude faster than with the standard SVD without incurring additional accuracy losses. We note that in our test cases we have always chosen the RRSVD parameters such that we obtain singular values (and vectors) that were as precise as those provided by the standard (LAPack) SVD routine. By relaxing this requirement, the speed-up can be increased further. Moreover, by augmenting RRSVD with the Accuracy Check feature we are able not only to detect any (very unlikely) deviations from the average

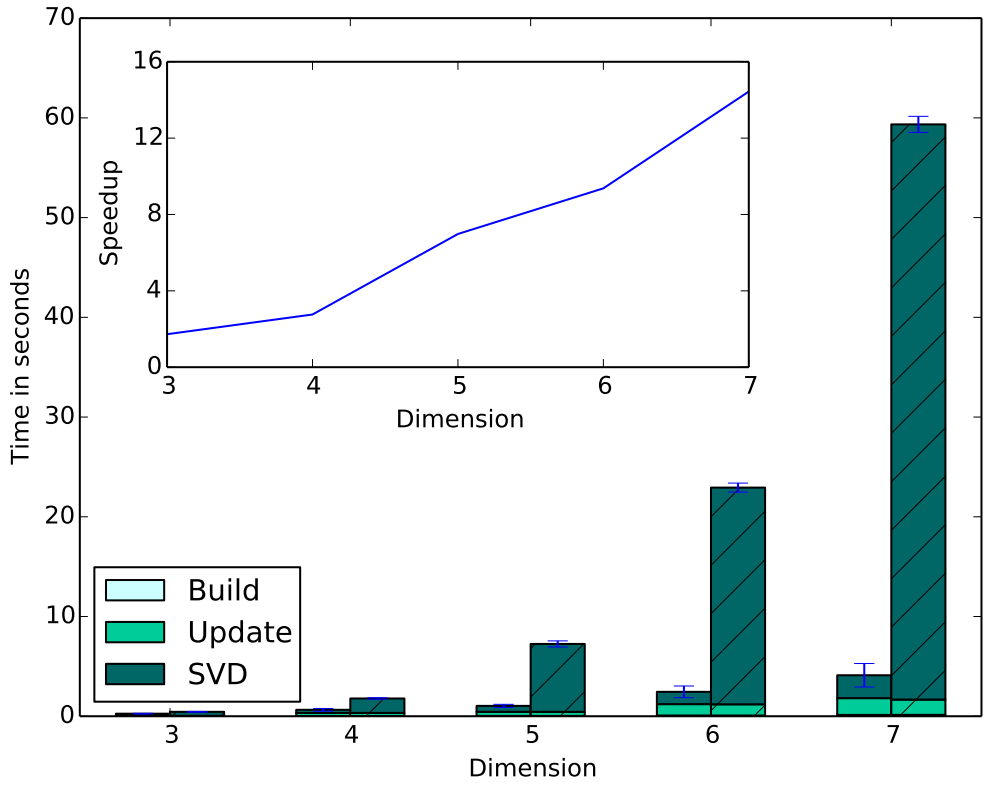


Figure 8.4: Profiling of the average time required by the SVD during a TEBD update step. The left bars show the time taken by the RRSVD, the right bars that of the standard SVD. The data refers to the MKL implementation executed with 16 MKL-threads. The (unbiased) standard deviation of the execution time for the SVD part of the update step is shown as an error bar on top of each bar. The inset presents the overall speed-up for one complete TEBD two-site update achieved by the RRSVD.

behavior, but also to understand whether the system is experiencing an entanglement build-up which would require an increasing of the retained Hilbert space.
In this chapter we focused on the TEBD algorithm and its application to the one-dimensional system obtained through a TEDOPA mapping of an open quantum system (Section 3.4). In this context, RRSVD makes it possible to increase the dimension of the local oscillators with a much reduced impact on the computational time, thus allowing for the efficient simulation of the system at higher temperatures. However, all MPS algorithms relying on the SVD to select the relevant Hilbert space can greatly benefit from the use of the RRSVD routine, as long as the ratio between the number of retained and total singular values is sufficiently small.
The real scope and impact of this new computational tool is still to be understood fully. To this end, we prepared the *RRSVD-Package*, a library that provides the RRSVD routine for single-/double-precision and real-/complex-matrices. The package includes all the different implementations (BL, MKL, GPU) of RRSVD and has been designed to be plugged into existing codes through very minor code modifications. In principle, it suffices to replace each call to the SVD by a corresponding call to the RRSVD. This should allow for a very quick test of the RRSVD in different simulation codes and

scenarios. The library is written in C++; a Fortran wrapper that allows to call the RRSVD routine from Fortran code is included as well. Some of the matrices used for the analysis of RRSVD in this paper are also available, together with some stand-alone code that exemplifies the use of RRSVD and how to reproduce some of the results reported in this paper. The RRSVD-Package is freely available at [197].
The results obtained for the GPU implementation are rather promising: For the largest matrices considered ($d_5, d_6, d_7$) the GPU performs as well as a full cluster node. Preliminary results on even larger matrices show that a GPU can become a valid alternative means to perform TEBD simulations of systems with high local dimensions, or when the number of retained dimensions needs to be increased because of larger correlation lengths. Moreover, if operated in the right way, a GPU can act as a large cluster of machines [200] without the difficulties stemming from the need of distributing the workload among different computational nodes (Message Passing Interface (MPI)). A full GPU version of TEBD can make the access to super-computing facilities superfluous: A typical laboratory workstation equipped with one or two GPUs would be sufficient. We are currently re-analyzing the TEBD algorithm to expose further options for parallelization, as for example in the construction of the $\widetilde{\Theta}$ matrix. It could be computed by an ad-hoc designed CUDA-kernel and is a valid target for improvement now that its computational complexity is similar to that of the SVD.

# CHAPTER 9

## Summary and outlook

The central theme of this work was the TEDOPA method, a novel tool to investigate open quantum systems numerically. We now briefly recapitulate the main results this work presented and how to proceed from there.
The main body, referring to Chapters 5 to 8, exhibits a two-fold character. At first, in Chapters 5 and 6, we applied TEDOPA to biological settings. The difficulty in describing these systems lies in their interaction with a complex protein environment that often features a heavily structured spectral function. Besides, the fact that their intra-system couplings are of the same order of magnitude than their couplings to the environment limits the applicability of perturbative approaches. These properties therefore make TEDOPA the method of choice for their investigation.

In Chapter 5 we managed to identify a mechanism that is able to explain excitonic coherence observed in pigment-protein complexes [7, 9, 11]. The complex interplay with sharp environmental modes of frequencies near-resonant to transition energies in the system leads to emergent long-lasting coherences. These sharp, underdamped modes couple to the excitonic coherence elements and, upon initial displacement, drive the excitonic coherence at later times. This process is identified as a regeneration of coherence and inherently different from protection of coherence. We were able to identify this underlying mechanism on a microscopic level and show its emergence within TEDOPA simulations, traces of it even visible in the environmental dynamics accessible by TEDOPA. This mechanism not only serves as an explanation of experimental results, but even offers design principles for the engineering of biomimetic devices.

In Chapter 6 we employ TEDOPA once more, uncovering and analyzing an ultrafast environmental process that causes energy transfer in the system to depend explicitly on the phase of an initial preparation of eigenstates. Remarkably, for particular phases and system parameters, the net energy flow is uphill, transiently violating the principle of detailed balance, and implying that energy is spontaneously taken up from the environment. Subsequent theoretical analysis traces this effect back to correlations within the background environment.

These investigations exploited TEDOPA's capabilities of treating arbitrary spectral densities and unrestricted coupling strengths. While biological settings are indeed a highly promising field, the generality of TEDOPA allows for many more applications, as has been shown i.e. by its application to photonic crystals [73]. A valuable target for TEDOPA, especially with the numerical improvements summarized below, is the FMO complex. Albeit its resulting tensor-network structure complicates its treatment, the large body of experimental and theoretical evidence present for it makes it a desirable target. Future extensions of TEDOPA, especially those that deal with highly connected tensor networks combined with improved local update schemes, could provide valuable insight and comparison to existing results. The next stage to reach this goal could be similar light harvesting structures, such as the B800 and B850 rings, in which EET and quantum coherence also has been studied [121, 201]. They offer a much easier configuration in the form of a less connected tensor network and thus are in principle already accessible by the extended TEDOPA. While similar structures already have been investigated numerically [202], TEDOPA's capabilities could shed new light onto exciton dynamics and the environment's role in these complexes.

The second part of this work dealt with various improvements for the TEDOPA framework. At first we drew on open quantum system techniques to drastically shorten TEDOPA simulations for certain parameter regimes. Next we improved its underlying numerical workhorse, the TEBD, by applying a randomized algorithm for the singular value decomposition, speeding it up by more than an order of magnitude.

In Chapter 7 we introduced the TTM and joined it with TEDOPA [3]. The main difficulty hereby lay in the fine-tuning of parameters and cutoffs to guarantee compatibility with both tools. This resulted in a method well-suited, but not restricted to, low-temperature regimes and very long simulation times. Thereby we produced a simulation framework that yields accurate results in the long-time evolution; especially for post-processed and averaging-type methods [173, 174] or Fourier and wavelet transformations [175] this becomes of interest. We illustrated this fact by producing highly accurate absorption spectra for a coupled dimeric system. The spectroscopic application presented is only a beginning. While the extension towards fluorescence spectra is a suitable first candidate, the field of non-linear spectroscopy might also be successfully tackled. The complex interplay of intra-system interactions and system-environment interactions and how it shapes the resulting spectra is still not fully understood. Should exact numerical studies of such systems become available, this could further promote the understanding and interpretation of experimentally obtained spectra of biological complexes.

In Chapter 8 we then moved on to improve the core part of the TEBD algorithm: The singular value decomposition [4]. Since the TEBD, and especially its two-site update that employs an SVD, is the numerically costliest part of TEDOPA, an improvement here is most beneficial. By employing the reduced-rank randomized singular value decomposition we avoid superfluous efforts in obtaining singular values only to discard them immediately. This offers a huge speed-up in the stand-alone version, embedded in the TEBD it still yields exceptional results and leads to a speed-up of more than an order of magnitude – especially in the case of high environmental dimensions as we encountered in biological settings [1, 2].

These numerical improvements still offer some potential. The rise of "single instruction multiple data"-technologies over the last years slowly leads to a paradigm change in the way programming is done. Especially costly operations from linear algebra, such as the indispensable SVD or matrix-matrix multiplications, can benefit heavily from these new trends. Thus the two-site update step in the TEBD scheme can possibly be made even cheaper yet. Similar benefits are expected from GPUs. Tentative analysis for the SVD show similar results for one GPU as for one cluster node. Exploiting relevant memory-design techniques, this offers the possibility to use a standalone machine for full-scale TEDOPA simulations, turning it into a standard tool which is not required to be backed up by a full-grown cluster.

While these twofold results aim at different directions, nevertheless they all center around the TEDOPA method. On joining the improving efforts of the last two chapters and focusing this combined power on the previously presented applications, we can expect great advances. Not only are new configurations and thus more complex real-life challenges accessible, but the additional, accompanying steady advance of computational resources enhances the range of accessible regimes yet again – firmly establishing TEDOPA as a general-purpose numerical method for open quantum systems.

# Acknowledgements

Die Danksagung wurde aus Datenschutzgründen aus der elektronischen Version entfernt.

# Curriculum Vitae

Der Lebenslauf wurde aus Datenschutzgründen aus der elektronischen Version entfernt.

## Kooperationen und Erklärung wissenschaftlicher Redlichkeit

Diese Arbeit wurde wurde in der *Controlled Quantum Dynamics Group* am Institut für Theoretische Physik der Universität Ulm verfasst, in Zusammenarbeit mit Prof. Martin B. Plenio, Prof. Dr. Susana F. Huelga, Dr. Felipe Caycedo-Soler, Dr. Alex W. Chin und Santiago Oviedo-Casado.

Weiterhin beruhen verschiedene Teile der Arbeit auf Kooperationen mit Dr. Javier Prior (Universidad Politécnica de Cartagena), Prof. Dr. Jianshu Cao und Dr. Javier Cerrillo (Massachusetts Institute of Technology) sowie Dr. Dario Tamascelli (Università degli Studi di Milano).

Hiermit erkläre ich, dass die vorliegende Arbeit selbstständig von mir und unter Zuhilfenahme keiner anderer als den angegebenen Hilfsmitteln und Quellen angefertigt wurde. Alle wörtlich oder inhaltlich übernommene Stellen sind als solche gekennzeichnet und die Satzung der Universität Ulm zur Sicherung guter wissenschaftlicher Praxis in der aktuellen Fassung vom 16.10.2009 wurde beachtet.

*Robert Rosenbach* *Ulm, Mai 2015*

# References


[1] A. W. Chin, J. Prior, R. Rosenbach, F. Caycedo-Soler, S. F. Huelga, and M. B. Plenio, Nature Physics pp. 113–118 (2013).

[2] S. Oviedo-Casado, J. Prior, A. W. Chin, R. Rosenbach, S. F. Huelga, and M. B. Plenio, Physical Review A **93**, 020102 (2016).

[3] R. Rosenbach, J. Cerrillo, S. F. Huelga, J. Cao, and M. B. Plenio, New Journal of Physics **18**, 023035 (2016).

[4] D. Tamascelli, R. Rosenbach, and M. B. Plenio, Physical Review E **91**, 063306 (2015).

[5] J. Prior, A. W. Chin, S. F. Huelga, and M. B. Plenio, Physical Review Letters **105**, 050404 (2010).

[6] A. W. Chin, Á. Rivas, S. F. Huelga, and M. B. Plenio, Journal of Mathematical Physics **51**, 092109 (2010).

[7] G. S. Engel, T. R. Calhoun, E. L. Read, T. K. Ahn, T. Mancal, Y. C. Cheng, R. E. Blankenship, and G. R. Fleming, Nature **446**, 782 (2007).

[8] G. Panitchayangkoon, D. Hayes, K. A. Fransted, J. R. Caram, E. Harel, J. Wen, R. E. Blankenship, and G. S. Engel, Proceedings of the National Academy of Sciences **107**, 12766 (2010).

[9] T. R. Calhoun, N. S. Ginsberg, G. S. Schlau-Cohen, Y.-C. Cheng, M. Ballottari, R. Bassi, and G. R. Fleming, The Journal of Physical Chemistry B **113**, 16291 (2009).

[10] D. Hayes, G. Panitchayangkoon, K. A. Fransted, J. R. Caram, J. Wen, K. F. Freed, and G. S. Engel, New Journal of Physics **12**, 065042 (2010).

[11] E. Collini, C. Y. Wong, K. E. Wilk, P. M. G. Curmi, P. Brumer, and G. D. Scholes, Nature **463**, 644 (2010).

[12] J. Cerrillo and J. Cao, Physical Review Letters **112**, 110401 (2014).

[13] H. Carmichael, *Statistical Methods in Quantum Optics 1: Master Equations and Fokker-Planck Equations*, Physics and Astronomy Online Library (Springer, 1998).

[14] U. Weiss, *Quantum Dissipative Systems* (World Scientific (Singapore), 2008).

[15] H. P. Breuer and F. Petruccione, *The Theory of Open Quantum Systems* (OUP Oxford, 2007).

[16] Á. Rivas and S. F. Huelga, *Open Quantum Systems: An Introduction*, SpringerBriefs in Physics (Springer, 2011).

[17] M. A. Nielsen and I. L. Chuang, *Quantum Computation and Quantum Information* (Cambridge University Press, 2004), 1st ed.

[18] G. Lindblad, Communications in Mathematical Physics **40**, 147 (1975).

[19] J. Jeske and J. H. Cole, Physical Review A **87**, 052138 (2013).

[20] A. G. Redfield, IBM Journal of Research and Development **1**, 19 (1957).

[21] H.-P. Breuer, Journal of Physics B: Atomic, Molecular and Optical Physics **45**, 154001 (2012).

[22] B. Vacchini, A. Smirne, E.-M. Laine, J. Piilo, and H.-P. Breuer, New Journal of Physics **13**, 093004 (2011).

[23] M. M. Wolf, J. Eisert, T. S. Cubitt, and J. I. Cirac, Physical Review Letters **101**, 150402 (2008).

[24] H.-P. Breuer, E.-M. Laine, and J. Piilo, Physical Review Letters **103**, 210401 (2009).

[25] Á. Rivas, S. F. Huelga, and M. B. Plenio, Physical Review Letters **05**, 050403 (2010).

[26] S. Nakajima, Progress of Theoretical Physics **20**, 948 (1958).

[27] R. Zwanzig, Journal of Chemical Physics **33**, 1338–1341 (1960).

[28] H. Grabert, Zeitschrift für Physik B Condensed Matter **49**, 161 (1982).

[29] R. Kühne and P. Reineker, Zeitschrift für Physik B Condensed Matter **31**, 105 (1978).

[30] M. A. Schlosshauer, *Decoherence and the quantum-to-classical transition*, The Frontiers Collection (Springer, 2007).

[31] A. J. Leggett, S. Chakravarty, A. T. Dorsey, M. P. A. Fisher, A. Garg, and W. Zwerger, Reviews of Modern Physics **59**, 1 (1987).

[32] M. Vojta, N.-H. Tong, and R. Bulla, Physical Review Letters **94**, 070604 (2005).

[33] R. Bulla, H.-J. Lee, N.-H. Tong, and M. Vojta, Physical Review B **71**, 045122 (2005).

[34] J. A. Barker, Journal of Chemical Physics **70**, 2914 (1979).

[35] D. E. Makarov and N. Makri, Journal of Chemical Physics **221**, 482 (1994).

[36] N. Makri and D. E. Makarov, Journal of Chemical Physics **102**, 4600 (1995).

[37] N. Makri and D. E. Makarov, Journal of Chemical Physics **102**, 4611 (1995).

[38] Y. Tanimura and R. Kubo, Journal of the Physical Society of Japan **58**, 1199 (1989).

[39] Y. Tanimura, Physical Review A **41**, 6676 (1990).

[40] Y. Tanimura, Journal of the Physical Society of Japan **75**, 082001 (2006).

[41] L. N. Trefethen and D. Bau, *Numerical Linear Algebra* (SIAM, 1997).

[42] W. H. Press, S. A. Teukolsky, W. T. Vetterling, and B. P. Flannery, *Numerical recipes in C (2nd ed.): The art of scientific computing* (Cambridge University Press, New York, NY, USA, 1992).

[43] J. Demmel, M. Gu, S. Eisenstat, I. Slapnicar, K. Veselic, and Z. Drmac, Tech. Rep., Linear Algebra Appl (1997).

[44] W. Gautschi, ACM Transactions on Mathematical Software **20**, 21 (1994).

[45] G. Vidal, Physical Review Letters **91**, 147902 (2003).

[46] G. Vidal, Physical Review Letters **93**, 040502 (2004).

[47] U. Schollwöck, Annals of Physics **326**, 96 (2011).

[48] G. Vidal, Physical Review Letters **98**, 070201 (2007).

[49] F. Verstraete, V. Murg, and J. I. Cirac, Advances in Physics **57**, 143 (2008).

[50] G. Vidal, Physical Review Letters **101**, 110501 (2008).

[51] M. Zwolak and G. Vidal, Physical Review Letters **93**, 207205 (2004).

[52] D. Perez-Garcia, F. Verstraete, M. M. Wolf, and J. I. Cirac, Quantum Information and Computation **7**, 401 (2007).

[53] S. Rommer and S. Östlund, Physical Review B **55**, 2164 (1997).

[54] S. R. White, Physical Review Letters **69**, 2863 (1992).

[55] K. Audenaert, J. Eisert, M. B. Plenio, and R. F. Werner, Physical Review A **66**, 042327 (2002).

[56] M. B. Plenio, J. Eisert, J. Dreißig, and M. Cramer, Physical Review Letters **94**, 060503 (2005).

[57] J. Eisert, M. Cramer, and M. B. Plenio, Reviews of Modern Physics **82**, 277 (2010).

[58] F. G. S. L. Brandão and M. Horodecki, Nature Physics **9**, 721 (2013).

[59] F. G. S. L. Brandão and M. Horodecki, Communications in Mathematical Physics **333**, 761 (2015).

[60] J. Eisert, M. Cramer, and M. B. Plenio, Reviews of Modern Physics **82**, 277 (2010).

[61] M. B. Hastings, Journal of Statistical Mechanics: Theory and Experiment **2007**, P08024 (2007).

[62] M. Suzuki, Communications in Mathematical Physics **57**, 193 (1977).

[63] M. Suzuki, Physics Letters A **146**, 319 (1990).

[64] A. E. Feiguin and S. R. White, Physical Review B **72**, 020404 (2005).

[65] M. Hochbruck and C. Lubich, SIAM Journal on Numerical Analysis **34**, 1911 (1997).

[66] J. J. García-Ripoll, New Journal of Physics **8**, 305 (2006).

[67] D. Gobert, C. Kollath, U. Schollwöck, and G. Schütz, Physical Review E **71**, 036102 (2005).

[68] A. T. Sornborger and E. D. Stewart, Physical Review A **60**, 1956 (1999).

[69] A. W. Chin, S. F. Huelga, and M. B. Plenio, in *Semiconductors and Semimetals*, edited by U. Würfel, M. Thorwart, E. R. Weber, and C. Jagadish (Academic Press, Burlington, 2011), vol. 85, pp. 115–144.

[70] M. P. Woods, R. Groux, A. W. Chin, S. F. Huelga, and M. B. Plenio, Journal of Mathematical Physics **55**, 032101 (2014).

[71] M. P. Woods, M. Cramer, and M. B. Plenio, Preprint arXiv:1504.01531 (2015).

[72] A. J. Daley, C. Kollath, U. Schollwöck, and G. Vidal, Journal of Statistical Mechanics: Theory and Experiment **2004**, P04005 (2004).

[73] J. Prior, I. de Vega, A. W. Chin, S. F. Huelga, and M. B. Plenio, Physical Review A **87**, 013428 (2013).

[74] R. Bulla, T. A. Costi, and T. Pruschke, Reviews of Modern Physics **80**, 395 (2008).

[75] P. Jordan, *Die Physik und das Geheimnis des organischen Lebens* (Friedrich Vieweg & Sohn, Braunschweig, 1943).

[76] E. Schrödinger, *What is life?: The physical aspect of the living cell* (Cambridge University Press, 1944).

[77] M. Arndt, O. Nairz, J. Vos-Andreae, C. Keller, G. Van der Zouw, and A. Zeilinger, Nature **401**, 680 (1999).

[78] M. Mohseni, Y. Omar, G. S. Engel, and M. B. Plenio, *Quantum Effects in Biology* (Cambridge University Press, 2014).

[79] S. F. Huelga and M. B. Plenio, Contemporary Physics **54**, 181 (2013).

[80] S. Johnsen and K. J. Lohmann, Nature Reviews Neuroscience **6**, 703 (2005).

[81] R. Wiltschko and W. Wiltschko, Biosensors **4**, 221 (2014).

[82] W. Wiltschko, R. Wiltschko, and T. Ritz, Procedia Chemistry **3**, 276 (2011), 22nd Solvay Conference on Chemistry.

[83] J. Cai and M. B. Plenio, Physical Review Letters **111**, 230503 (2013).

[84] J. C. Brookes, Philosophical Transactions of the Royal Society of London A. (Mathematical, Physical and Engineering Sciences) **368** (2010).

[85] J. E. Amoore, Letters to Nature **199**, 912 (1963).

[86] E. Tareilus, J. Noé, and H. Breer, Biochimica et Biophysica Acta (BBA) - Molecular Cell Research **1269**, 129 (1995).

[87] G. Malcolm Dyson, Journal of the Society of Chemical Industry **57**, 647 (1938).

[88] R. H. Wright, Journal of Theoretical Biology **64**, 473 (1977).

[89] M. I. Franco, L. Turin, A. Mershin, and E. M. C. Skoulakis, Proceedings of the National Academy of Sciences **108**, 3797 (2011).

[90] L. Turin, Chemical Senses **21**, 773 (1996).

[91] J. C. Brookes, F. Hartoutsiou, A. P. Horsfield, and A. M. Stoneham, Physical Review Letters **98**, 038101 (2007).

[92] R. E. Blankenship, *Molecular Mechanisms of Photosynthesis* (Blackwell Science Ltd, 2002).

[93] J. T. Beatty, J. Overmann, M. T. Lince, A. K. Manske, A. S. Lang, R. E. Blankenship, C. L. van Dover, T. A. Martinson, and F. G. Plumley, Proceedings of the National Academy of Sciences of the United States of America **102**, 9306 (2005).

[94] T. M. Wahlund, C. R. Woese, R. W. Castenholz, and M. T. Madigan, Archives of Microbiology **156**, 81 (1991).

[95] J. Wen, H. Zhang, M. L. Gross, and R. E. Blankenship, Proceedings of the National Academy of Sciences **106**, 6134 (2009).

[96] R. E. Fenna and B. W. Matthews, Nature **258**, 573 (1975).

[97] J. Adolphs and T. Renger, Biophysical Journal **91**, 2778 (2006).

[98] D. E. Tronrud, J. Wen, L. Gay, and R. E. Blankenship, Photosynthesis Research **100**, 79 (2009).

[99] M. Schmidt am Busch, F. Müh, M. El-Amine Madjet, and T. Renger, Journal of Physical Chemistry Letters **2**, 93 (2011).

[100] J. Moix, J. Wu, P. Huo, D. Coker, and J. Cao, The Journal of Physical Chemistry Letters **2**, 3045 (2011).

[101] R. K. Chain and D. I. Arnon, Proceedings of the National Academy of Sciences **74**, 3377 (1977).

[102] S. Mukamel, *Principles of Nonlinear Optical Spectroscopy* (Oxford University Press, New York, 1995).

[103] V. May and O. Kühn, *Charge and Energy Transfer Dynamics in Molecular Systems* (Wiley-VCH, Weinheim, Germany, 2011).

[104] E. L. Read, H. Lee, and G. R. Fleming, Photosynthesis Research **101**, 233 (2009).

[105] H. van Amerongen, L. Valkunas, and R. van Grondelle, *Photosynthetic Excitons* (World Scientific, Singapore, 2000).

[106] M. Cho, *Two-Dimensional Optical Spectroscopy* (CRC Press, Boca Raton, 2009).

[107] I. P. Mercer, Y. C. El-Taha, N. Kajumba, J. P. Marangos, J. W. G. Tisch, M. Gabrielsen, R. J. Cogdell, E. Springate, and E. Turcu, Physical Review Letters **102**, 057402 (2009).

[108] J. Strümpfer and K. Schulten, Journal of Chemical Physics **134** (2011).

[109] C. Olbrich, J. Strümpfer, K. Schulten, and U. Kleinekathöfer, Journal of Physical Chemistry **115**, 758 (2011).

[110] M. Mohseni, P. Rebentrost, S. Lloyd, and A. Aspuru-Guzik, The Journal of Chemical Physics **129**, 174106 (2008).

[111] M. B. Plenio and S. F. Huelga, New Journal of Physics **10**, 113019 (2008).

[112] T. Förster, Annalen der Physik **437**, 55 (1948).

[113] A. W. Chin, S. F. Huelga, and M. B. Plenio, Philosophical Transactions of the Royal Society **370**, 3638 (2012).

[114] M. del Rey, A. W. Chin, S. F. Huelga, and M. B. Plenio, Journal of Physical Chemistry Letters **4**, 903 (2013).

[115] L. A. Pachon and P. Brumer, Physical Chemistry - Chemical Physics **14**, 10094 (2012).

[116] J. Strümpfer and K. Schulten, Journal of Chemical Theory and Computation **8**, 2808 (2012).

[117] P. Nalbach, J. Eckel, and M. Thorwart, New Journal of Physics **12**, 065043 (2010).

[118] G. D. Scholes, G. R. Fleming, A. Olaya-Castro, and R. van Grondelle, Nature Chemistry **3**, 763 (2011).

[119] F. Caruso, A. W. Chin, A. Datta, S. F. Huelga, and M. B. Plenio, Journal of Chemical Physics **131**, 105106 (2009).

[120] A. Ishizaki, T. R. Calhoun, G. S. Schlau-Cohen, and G. R. Fleming, Physical Chemistry - Chemical Physics **12**, 7319 (2010).

[121] A. Olaya-Castro, C. F. Lee, F. F. Olsen, and N. F. Johnson, Physical Review B **78**, 085115 (2008).

[122] S. Matsuzaki, V. Zazubovich, M. Rätsep, J. M. Hayes, and G. J. Small, The Journal of Physical Chemistry B **104**, 9564 (2000).

[123] M. Wendling, T. Pullerits, M. A. Przyjalgowski, S. I. E. Vulto, T. J. Aartsma, R. van Grondelle, and H. van Amerongen, The Journal of Physical Chemistry B **104**, 5825 (2000).

[124] M. Rätsep, R. E. Blankenship, and G. J. Small, The Journal of Physical Chemistry B **103**, 5736 (1999).

[125] M. Rätsep and A. Freiberg, Journal of Luminescence **127**, 251 (2007).

[126] L. A. Pachón and P. Brumer, The Journal of Physical Chemistry Letters **2**, 2728 (2011).

[127] C. Kreisbeck and T. Kramer, The Journal of Physical Chemistry Letters **3**, 2828 (2012).

[128] M. O. Scully, K. R. Chapin, K. E. Dorfman, M. B. Kim, and A. Svidzinsky, Proceedings of the National Academy of Sciences **108**, 15097 (2011).

[129] M. Rätsep, H.-M. Wu, J. M. Hayes, R. E. Blankenship, R. J. Cogdell, and G. J. Small, The Journal of Physical Chemistry B **102**, 4035 (1998).

[130] M. B. Plenio and S. F. Huelga, Physical Review Letters **88**, 197901 (2002).

[131] J. Eisert, M. B. Plenio, S. Bose, and J. Hartley, Physical Review Letters **93**, 190402 (2004).

[132] S. F. Huelga and M. B. Plenio, Physical Review Letters **98**, 170601 (2007).

[133] L. Hartmann, W. Dür, and H. J. Briegel, New Journal of Physics **9**, 230 (2007).

[134] J.-M. Cai, S. Popescu, and H. J. Briegel, Physical Review E **82**, 021921 (2010).

[135] F. L. Semião, K. Furuya, and G. J. Milburn, New Journal of Physics **12**, 083033 (2010).

[136] M. Sarovar, Y.-C. Cheng, and K. B. Whaley, Physical Review E **83**, 011906 (2011).

[137] F. Caycedo-Soler, A. W. Chin, J. Almeida, S. F. Huelga, and M. B. Plenio, Journal of Chemical Physics **136**, 155102 (2012).

[138] N. Christensson, H. F. Kauffmann, T. Pullerits, and T. Mančal, The Journal of Physical Chemistry B **116**, 7449 (2012).

[139] V. I. Novoderezhkin, A. G. Yakovlev, R. van Grondelle, and V. A. Shuvalov, Journal of Physical Chemistry B **108**, 7445 (2004).

[140] K. Blum, *Density Matrix Theory and Applications* (Plenum Press, New York, London, 1981).

[141] A. W. Chin, S. F. Huelga, and M. B. Plenio, Physical Review Letters **109**, 233601 (2012).

[142] R. J. W. Louwe and T. J. Aartsma, The Journal of Physical Chemistry B **101**, 7221 (1997).

[143] R. Hildner, D. Brinks, and N. F. van Hulst, Nature Physics **7**, 172 (2011).

[144] C. Theiss, I. Trostmann, S. Andree, F. J. Schmitt, T. Renger, H. J. Eichler, H. Paulsen, and G. Renger, The Journal of Physical Chemistry B **111**, 13325 (2007).

[145] G. Panitchayangkoon, D. V. Voronine, D. Abramavicius, J. R. Caram, N. H. C. Lewis, S. Mukamel, and G. S. Engel, Proceedings of the National Academy of Sciences, USA **108**, 20908 (2011).

[146] E. Collini and G. D. Scholes, Science **323**, 369 (2009).

[147] E. Collini and G. D. Scholes, The Journal of Physical Chemistry A **113**, 4223 (2009).

[148] A. F. Fidler, E. Harel, and G. S. Engel, Journal of Physical Chemistry Letters **1**, 2876 (2010).

[149] C. Creatore, M. A. Parker, S. Emmott, and A. W. Chin, Physical Review Letters **111**, 253601 (2013).

[150] K. E. Dorfman, D. V. Voronine, S. Mukamel, and M. O. Scully, Proceedings of the National Academy of Sciences **110**, 2746 (2013).

[151] E. Romero, I. H. M. van Stokkum, V. I. Novoderezhkin, J. P. Dekker, and R. van Grondelle, Biochemistry **49**, 4300 (2010).

[152] N. Killoran, S. F. Huelga, and M. B. Plenio, E-print arXiv:1412.4136 (2014).

[153] F. Caruso, A. W. Chin, A. Datta, S. F. Huelga, and M. B. Plenio, Physical Review A **81**, 062346 (2010).

[154] P. Rebentrost, M. Mohseni, I. Kassal, S. Lloyd, and A. Aspuru-Guzik, New Journal of Physics **11**, 033003 (2009).

[155] A. Ishizaki and G. R. Fleming, Proceedings of the National Academy of Sciences **106**, 17255 (2009).

[156] A. W. Chin, A. Datta, F. Caruso, S. F. Huelga, and M. B. Plenio, New Journal of Physics **12**, 065002 (2010).

[157] V. Tiwari, W. K. Peters, and D. M. Jonas, Proceedings of the National Academy of Sciences **110**, 1203 (2013).

[158] A. Kolli, E. J. O'Reilly, G. D. Scholes, and A. Olaya-Castro, The Journal of Chemical Physics **137**, 174109 (2012).

[159] E. Romero, R. Augulis, V. I. Novoderezhkin, M. Ferretti, J. Thieme, D. Zigmantas, and R. van Grondelle, Nature Physics **10**, 676 (2014).

[160] S. Gélinas, A. Rao, A. Kumar, S. L. Smith, A. W. Chin, J. Clark, T. S. van der Poll, G. C. Bazan, and R. H. Friend, Science **343**, 512 (2014).

[161] G. Ritschel, J. Roden, W. T. Strunz, and A. Eisfeld, New Journal of Physics **13**, 113034 (2011).

[162] A. W. Chin, J. Prior, S. F. Huelga, and M. B. Plenio, Physical Review Letters **107**, 160601 (2011).

[163] T. Renger, V. May, and O. Kühn, Physics Reports **343**, 137 (2001).

[164] R. Alicki and K. Lendi, *Quantum Dynamical Semigroups and Applications* (Springer, Berlin, Heidelberg, 2007).

[165] R. Gebauer and R. Car, Physical Review Letters **93**, 160404 (2004).

[166] E. B. Davies, Communications in Mathematical Physics **39**, 91 (1974).

[167] A. Chenu, N. Christensson, H. F. Kauffmann, and T. Manfçal, Scientific Reports **3**, 2029 (2013).

[168] V. Tiwari, W. K. Peters, and D. M. Jonas, Nature Chemistry **6**, 173 (2014).

[169] J. Lim, D. Paleček, F. Caycedo-Soler, C. N. Lincoln, J. Prior, H. von Berlepsch, S. F. Huelga, M. B. Plenio, D. Zigmantas, and J. Hauer, E-print arXiv:1502.01717 (2015).

[170] M. B. Plenio, J. Almeida, and S. F. Huelga, Journal of Chemical Physics **139**, 235102 (2014).

[171] J. M. Womick and A. M. Moran, The Journal of Physical Chemistry B **115**, 1347 (2011).

[172] M.-D. Choi, Linear Algebra and its Applications **10**, 285 (1975).

[173] J. Almeida, J. Prior, and M. B. Plenio, The Journal of Physical Chemistry Letters **3**, 2692 (2012).

[174] J. N. Sanders, X. Andrade, and A. Aspuru-Guzik, ACS Central Science **1**, 24 (2015).

[175] J. Prior, E. Castro, A. W. Chin, J. Almeida, S. F. Huelga, and M. B. Plenio, Journal of Chemical Physics **139**, 224103 (2013).

[176] S. R. White and A. E. Feiguin, Physical Review Letters **93**, 076401 (2004).

[177] J. J. Garcìa-Ripoll, New Journal of Physics **8**, 305 (2006).

[178] N. Halko, P. Martinsson, and J. Tropp, SIAM Review **53**, 217 (2011).

[179] G. H. Golub and C. F. Van Loan, *Matrix computations* (Johns Hopkins University Press, 1996), 3rd ed.

[180] T. Hastie, R. Tibshirani, and J. Friedman, *The Elements of Statistical Learning* (Springer-Verlag, 2009), 2nd ed.

[181] E. J. Candes and B. Recht, Foundations of Computational Mathematics **9**, 717 (2009).

[182] D. Sorensen, Tech. Rep., CAAM at Rice University (1998).

[183] D. Sorensen, Acta Numerica pp. 519–584 (2002).

[184] R. M. Larsen, Tech. Rep. DAIMI PB-357, Department of Computer Science, Aarhus University (1998).

[185] Y. Saad, SIAM Journal on Numerical Analysis **29**, 209 (1992).

[186] M. Hochbruck and C. Lubich, SIAM Journal on Numerical Analysis **34**, 1911 (1997).

[187] M. B. Plenio and S. Virmani, Quantum Information and Computation **7**, 1 (2007).

[188] P. Calabrese and A. Lefevre, Physical Review A **78**, 032329 (2008).

[189] N. Schuch, M. M. Wolf, F. Verstraete, and J. I. Cirac, Physical Review Letters p. 030504 (2008).

[190] *http://www.netlib.org/blas/*.

[191] *http://www.netlib.org/lapack/*.

[192] *https://software.intel.com/en-us/intel-mkl*.

[193] *https://developer.nvidia.com/cublas*.

[194] *http://www.culatools.com*.

[195] *http://www.netlib.org/blas/cblas*.

[196] *http://www.netlib.org/lapack/lapacke.html*.

[197] *https://github.com/kindaguy/rrsvd.git*.

[198] S. Voronin and P. Martinsson, arXiv:1502.05366 (2015).

[199] G. M. Amdahl, AFIPS Conference Proceedings **30**, 483 (1967).

[200] D. Tamascelli, F. S. Dambrosio, R. Conte, and M. Ceotto, Journal of Chemical Physics **140**, 174109 (2014).

[201] Y. C. Cheng and R. J. Silbey, Physical Review Letters **96**, 028103 (2006).

[202] J. Strümpfer and K. Schulten, The Journal of Chemical Physics **131**, 225101 (2009).